Of Road Blocks and Loading Bays

–

Control Mechanisms of Dendritic Cargo Trafficking

Dissertation

Zur Erlangung des Doktorgrades der Naturwissenschaften am Fachbereich Chemie der Fakultät für Mathematik, Informatik und Naturwissenschaften der Universität Hamburg

vorgelegt von

Anja Konietzny

Fachbereich Chemie, Universität Hamburg

und

Zentrum für Molekulare Neurobiologie Hamburg, Universitätsklinikum Eppendorf

Januar 2020

Thesis evaluators

Prof. Dr. Henning Tidow
Institute of Biochemistry and Molecular Biology, University of Hamburg

Dr. Marina Mikhaylova
Center for Molecular Neurobiology Hamburg (ZMNH), University Clinic Hamburg-Eppendorf (UKE)

Disputation

13.03.2020

Examiners

Prof. Dr. Wolfram Brune

Heinrich Pette Institute (HPI), Leibniz Institute for Experimental Virology, Hamburg

Prof. Dr. Wolfgang Maison

Institute of Pharmacy, University of Hamburg

Dr. Marina Mikhaylova

Center for Molecular Neurobiology Hamburg (ZMNH), University Clinic Hamburg-Eppendorf (UKE)

The work presented in this dissertation was done between January 2016 and December 2019 in the group of Dr. Marina Mikhaylova at the Center for Molecular Neurobiology Hamburg (ZMNH).

List of Publications

First Authorships:

Konietzny A*****, Gonzalez-Gallego J*****, Baer J, Perez-Alvarez A, Drakew A, Demmers JAA, Deckers DHW, Hammer 3rd JA, Frotscher M, Oertner T, Wagner W, Kneussel M, Mikhaylova M. (2019) Myosin V regulates synaptopodin clustering and localization in dendrites of hippocampal neurons. Journal of Cell Science 2019 132: jcs230177. doi: 10.1242/jcs.230177. ***** first authors

van Bommel B***, Konietzny** A*****, Kobler O, Bär J, Mikhaylova M. (2019). F-actin patches associated with glutamatergic synapses control positioning of dendritic lysosomes. EMBO J. 27:e101183. doi: 10.15252/embj.2018101183. ***** first authors

Review article:

Konietzny A, Bär J, Mikhaylova M. (2017) Dendritic Actin Cytoskeleton: Structure, Functions, and Regulations. Front Cell Neurosci. 18;11:147. doi: 10.3389/fncel.2017.00147.

Co-Authorships:

Mikhaylova M, Bär J, van Bommel B, Schätzle P, YuanXiang P, Raman R, Hradsky J**, Konietzny** A, Loktionov EY, Reddy PP, Lopez-Rojas J, Spilker C, Kobler O, Raza SA, Stork O, Hoogenraad CC, Kreutz MR. (2018). Caldendrin Directly Couples Postsynaptic Calcium Signals to Actin Remodeling in Dendritic Spines. Neuron 7;97(5):1110-1125.e14. doi: 10.1016/j.neuron.2018.01.046.

Heinz LS, Muhs S, Schiewek J, Grüb S, Nalaskowski M, Lin YN, Wikman H, Oliveira-Ferrer L, Lange T, Wellbrock J, **Konietzny** A, Mikhaylova M, Windhorst S. (2017) Strong fascin expression promotes metastasis independent of its F-actin bundling activity. Oncotarget 1;8(66):110077-110091. doi: 10.18632/oncotarget.22249.

Co-Authorships (submitted ; publication pending):

Hu C, Kanellopoulos A, **Konietzny** A, Richter M, Tenedini F, Petersen M, Hoyer N, Cheng L, Poon C, Harvey K, Windhorst S, Parish J, Mikhaylova M, Bagni C, Calderon de Anda F, Soba P. (2019) Conserved Tao kinase activity regulates dendritic arborization, dynamics and sensory function in Drosophila. In revision at the Journal of Neuroscience. JN-RM-1846-19R1

Pelucchi S, Vandermeulen L, Pizzamiglio L, Aksan B, Yan J, **Konietzny** A, Bonomi E, Borroni B, Rust M, Di Marino D, Mikhaylova M, Mauceri D, Antonucci F, Gardoni F, Di Luca M, Marcello E. (2019) CAP2 dimer controls structural synaptic plasticity by regulating cofilin localization in spines. Under review in Brain. BRAIN-2019-02049

II. Table of contents

List of Abbreviations

ABP	actin-binding protein
AIS	axon initial segment
AMPAR	N-methyl-D-aspartate receptor
ANOVA	analysis of variance
ATP	adenosine triphosphate
CaM	calmodulin
CaMKII	Ca^{2+}/calmodulin-dependent protein kinase II
cAMP	cyclic adenosine monophosphate
CDD	caldendrin
CNS	central nervous system
DIV	days in vitro
DMSO	dimethylsulfoxide
DN	dominant negative
EGTA	ethylene glycol-bis(β-aminoethyl ether)-N,N,N',N'-tetraacetic acid
EM	electron microscopy
ER	endoplasmic reticulum
ERGIC	ER to Golgi intermediate compartment
F-actin	filamentous actin
fl	full length
FRAP	fluorescence recovery after photobleaching
GABA	gamma-aminobutyric acid
GFP / RFP	green / red fluorescent protein
GTD	globular tail domain (myosin V cargo binding domain)
GTP	guanosine triphosphate
HEK293T	human embryonic kidney cell line expressing the SV40 T-antigen
k.o.	knock-out
LAMP1	lysosome associated membrane protein 1
LTP	long-term potentiation
MPS	membrane-associated periodic skeleton
MT	microtubule
NMDAR	α-amino-3-hydroxy-5-methyl-4-isoxazolepropionic acid receptor
N-WASP	neuronal Wiskott–Aldrich Syndrome protein
PEG	polyethyleneglycol
PKA	protein kinase A
PLL	poly-L-lysine
PSD	post-synaptic density
RNA / mRNA	ribonucleic acid / messenger ribonucleic acid
RNPs	ribonucleoprotein particles
SA	spine apparatus
SEM	standard error of the mean
TIRF	total internal reflection
wt	wild type

Abstract

Neurons are among the largest and most intricate cells of the body. Their elaborate morphology is the basis for their function in complex nervous systems, but it comes with a few challenges. Proteins, organelles and membrane components need to be transported over large distances to be available exactly where they are needed at each point in time. Therefore, cargo is constantly on the move to allow neurons to react dynamically to various external and internal stimuli. Directed cargo transport inside cells relies on the cytoskeleton and associated motor proteins, which use the cytoskeleton as walkways to move their specific cargo throughout the cell. Two distinct cytoskeletal systems, the microtubule and the actin cytoskeleton, fulfill complementary roles in this context. The microtubule cytoskeleton is used for fast, long-distance transport, whereas the actin cytoskeleton provides structural stability, as well as anchor points for stationary cargo and short-distance transport. For a long time, the most prominent roles that were attributed to actin in neurons were the movement of growth cones, polarized cargo sorting at the axon initial segment, and the dynamic plasticity of dendritic spines, since those compartments contain large accumulations of actin filaments (F-actin) that can be easily visualized using electron- and fluorescence microscopy. With the recent development of super-resolution microscopy, previously unknown structures of the actin cytoskeleton have been uncovered: a membrane-associated periodic skeleton (MPS) consisting of a periodic actin-spectrin lattice, stretches of longitudinal actin filaments inside neurites, as well as spatially confined patches of F-actin inside the dendritic shaft. During the course of my doctoral studies, I focused on factors and molecular players that interact with and rely on the actin cytoskeleton, especially through the actin-associated motor protein myosin V.

We characterized the dendritic actin cytoskeleton in detail, with a focus on dendritic actin patches, and found that they are frequently located at the base of dendritic spines, or form around excitatory shaft synapses. Using lysosomes as an example for mobile organelles, we demonstrated that the presence of actin patches has a strong impact on dendritic organelle transport. We provided mechanistic insights on this pausing behavior, demonstrating that actin patches form a physical barrier for microtubule-based, kinesin-driven cargo. In addition, we identified the F-actin based motor myosin Va as one of the active brakes which mediate long-term cargo stalling. As precisely regulated organelle positioning within neurites is required for proper neuronal function, we propose that active cargo stalling at actin patches is a generalized principle by which neurons control organelle trafficking.

We further investigated the role of myosin V in the targeted localization of an endoplasmatic-reticulum-derived organelle called the spine apparatus, which is present in a subset of dendritic spines. While it was known before that the protein synaptopodin is essential for the formation of the spine apparatus, it was still unclear which factors contribute to its localization at selected synapses. We characterized development, localization and mobility of synaptopodin clusters in hippocampal neurons, as well as the molecular dynamics within these clusters. We identified the motor proteins myosin V and VI as novel interaction partners of synaptopodin and demonstrated that myosin V is involved in the formation and/or maintenance of the spine apparatus.

Finally, we asked which factors govern myosin V activity, and which could provide precise spatial and temporal regulation of this motor protein. We focused on the role of calcium signaling, and found that several myosin motors, including myosin V and VI, directly interact with the calcium-sensing protein caldendrin. The investigations on the effect of caldendrin binding to myosin are still ongoing. However, given the fact that caldendrin becomes selectively activated in dendritic spines following synaptic activation, we propose that it represents a way of coupling synaptic activity to the regulation of myosin motors.

Zusammenfassung

Neurone gehören zu den größten und kompliziertesten Zellen des Körpers. Ihre weitverzweigte Morphologie ist grundlegend für ihre Funktion in komplexen Nervensystemen, bringt jedoch einige Herausforderungen mit sich. Zellbausteine wie Proteine, Organellen und Membrankomponenten müssen über große Entfernungen transportiert werden, um jederzeit genau dort verfügbar zu sein, wo sie benötigt werden. Diese Bausteine sind ständig in Bewegung, damit Neurone dynamisch auf verschiedene äußere und innere Reize reagieren können. Ihr gezielter Transport innerhalb von Zellen benötigt das Zytoskelett und dazugehörige Motorproteine, die das Zytoskelett als Trassen verwenden, um ihre spezifische Fracht durch die Zelle zu befördern. Zwei unterschiedliche Zytoskelettsysteme, das Mikrotubuli- und das Aktin-Zytoskelett, erfüllen in diesem Zusammenhang komplementäre Rollen. Das Mikrotubuli-Zytoskelett wird für schnellen Transport über lange Strecken verwendet, während das Aktin-Zytoskelett strukturelle Stabilität bietet, sowie als Ankerpunkt und für lokalen Kurzstreckentransport verwendet wird. Lange Zeit waren die wichtigsten Funktionen, die Aktin in Neuronen zugeschrieben wurden, das Steuern von Wachstumskegeln, das Sortieren von Zellbausteinen im „axon initial segment“, und die dynamische Plastizität von dendritischen Spines. Die genannten Kompartimente enthalten sehr große Mengen an Aktinfilamenten (F-Aktin), weshalb diese historisch mittels Elektronen- und Fluoreszenzmikroskopie gut sichtbar gemacht werden konnten. Nun konnten dank jüngster Fortschritte in der hochauflösenden Mikroskopie einige bisher unbekannte Strukturen des Aktin-Zytoskeletts aufgedeckt werden: ein membranassoziiertes periodisches Skelett (MPS), das aus einem periodischen Aktin-Spektrin-Gitter besteht, Bündel von longitudinalen Aktinfilamenten innerhalb von Neuriten, und räumlich abgegrenzte Ansammlungen („Patches“) von F-Aktin innerhalb des dendritischen Schafts. Während meiner Promotion habe ich mich auf Faktoren konzentriert, die mit dem Aktin-Zytoskelett interagieren und auf dieses angewiesen sind, insbesondere im Zusammenhang mit dem Aktin-assoziierte Motorprotein Myosin V.

Wir haben das dendritische Aktin-Zytoskelett und die neu entdeckten Aktin-Patches detailliert charakterisiert und festgestellt, dass diese sich häufig an der Basis dendritischer Spines, oder an exzitatorischen Schaftsynapsen befinden. Anhand von Lysosomen als Beispiel für mobile Organellen konnten wir zeigen, dass das Vorhandensein von Aktin-Patches einen starken Einfluss auf den Transport dendritischer Organellen hat. Wir beschrieben mechanistische Hintergründe in deren Bewegungsmustern und zeigten, dass Aktin-Patches eine physikalische Barriere für Mikrotubuli-basierte, von dem Motorprotein Kinesin getriebene Transportvorgänge darstellen. Darüber hinaus identifizierten wir den F-Aktin-basierten Motor Myosin Va als einen aktiven Brems-Faktor, der längere Transport-Pausen vermittelt. Um die normale Funktion von Neuronen zu gewährleisten, ist eine präsize regulierte Lokalisation von Zellbausteinen und Organellen, wie zum Beispiel Lysosomen, essentiell wichtig. Daher schlagen wir vor, dass das aktive Abbremsen von mobilen Zellbausteinen an Aktin-Patches einen allgemeinen Mechanismus darstellt, den intrazellulären Transport in Neuronen zu kontrollieren. Desweiteren untersuchten wir die Rolle von Myosin V in der Entstehung und Regulation des Spine-Apparates (SA), einer mit dem endoplasmatischen Retikulum verwandten Organelle. Diesen findet man vor allem in besonders großen und stabilen dendritischen Spines. Während vorab bekannt war, dass das Protein Synaptopodin für die Bildung des SA essentiell ist, war bisher noch unklar, welche Faktoren seine Lokalisierung an ausgewählten Spines vermitteln. Wir charakterisierten die Entstehung, Lokalisation und Mobilität von Synaptopodin-Clustern in hippocampalen Neuronen, sowie die Moleküldynamik innerhalb dieser Cluster. Wir identifizierten die Motorproteine Myosin V und VI als neue Interaktionspartner von Synaptopodin und konnten zeigen, dass Myosin V an der Bildung und / oder Aufrechterhaltung des SA beteiligt ist. Schließlich fragten wir, welche Faktoren die Aktivität von Myosin-V selbst steuern, und die räumliche und zeitliche Regulation dieses Motorproteins ermöglichen. Wir konzentrierten uns auf die Rolle von Kalzium-Ionen und stellten fest, dass mehrere Myosinmotoren, einschließlich Myosin V und VI, direkt mit dem Kalziumsensorprotein Caldendrin interagieren. Die Untersuchungen, welchen Effekt die Bindung von Caldendrin an Myosin hat, dauern noch an. Angesichts der Tatsache, dass Caldendrin infolge von synaptischer Aktivität in dendritischen Spines selektiv aktiviert wird, schlagen wir jedoch vor, dass über Caldendrin die Regulation von Myosin-Motoren an synaptische Aktivität gekoppelt werden kann.

Introduction

Neurons in the central nervous system

Neurons, or nerve cells, are the main components of the peripheral and central nervous systems (CNS). Together with glial cells, which provide structural and metabolic support, they make up the main part of nervous tissue. Neurons are electrically excitable cells that communicate with each other, and with other cell types, via tight connections called **synapses**. The unique ability of neurons to form networks that compute and convey information is the fundamental basis of any functioning nervous system. In the brain, billions of neurons, interconnected into a (so far) immeasurable number of neural circuits, give rise to thought, emotion, and behavior. Based on the current state of research, it seems that a vital aspect underlying the functioning of those neural networks is their plasticity. In order to learn, store or retrieve memories, neuronal circuits change and adapt constantly. This is possible through the loss, strengthening or *de novo* establishment of synaptic contacts between individual neurons.

Although there are many different types of specialized neurons within the brain, they all share a common morphology, which comprises several functionally distinct compartments: dendrites, the axon and the cell body. **Dendrites** are long, highly branched extensions from the cell body that can reach hundreds of microns in length, forming a widespread and complex arbor. They receive information from typically thousands of synaptic inputs, which is then further transmitted via the cell body to the neuron's single axon (Figure 1A) (Gulledge *et al*, 2005; Magee, 2000). This information is received in the form of chemical and electrical signals. Like most cell types, neurons maintain a voltage gradient, or membrane potential, across their outer membrane by actively building up a concentration gradient of ions (Na^+, K^+, Cl^-) between inside and outside of the cell. This is achieved by membrane-integrated ion transporters or ion pumps, which use energy in the form of ATP to move ions across the membrane until the inside potential reaches about - 70 mV relative to the outside. One hallmark of the neuronal cell type is their electrical excitability, i.e. their ability to rapidly de- and re-polarize the membrane potential in response to certain stimuli. This mostly relies on voltage-sensitive sodium channels. Those channels open upon a slight depolarization of the membrane potential, thus amplifying the initial depolarizing impulse and causing a spike in membrane potential to approx. + 40 mV. These spikes travel along neurites in a wave-liker manner as electrochemical pulses, or **action potentials**. Membrane compartments that have been depolarized are rapidly repolarized by re-establishing the ion gradient in a matter of milliseconds.

Dendrites receive input from upstream axons in the form of neurotransmitters released at synaptic sites (Figure 1B). **Synapse** types are subdivided into inhibitory and excitatory synapses. As the name suggest, inhibitory synapses induce pathways that inhibit the post-synaptic neuron from firing, whereas excitatory synapses can induce the activation of the post-synaptic neuron. When an action potential travels along an axon, it causes the release of pre-synaptic vesicles containing **neurotransmitters**. In the CNS, the major excitatory and inhibitory neurotransmitters are glutamate and GABA (gamma-aminobutyric acid), respectively. The post-synaptic membrane contains neurotransmitter receptors, which elicit a response depending on the type of transmitter-receptor pair. Metabotropic receptors initiate a second messenger pathway, whereas ionotropic receptors initiate an electrical response. Examples of excitatory ionotropic transmitter-receptor pairs are glutamate and two of its most prevalent receptors, called NMDA receptor (NMDAR) and AMPA receptor (AMPAR; NMDA = α-amino-3-hydroxy-5-methyl-4-isoxazolepropionic acid, AMPA = N-methyl-D-aspartate). AMPARs and NMDARs are found along the dendritic plasma membrane but are

particularly enriched at excitatory synapses. Both are ion-channels which open upon ligand binding, causing an efflux of K^+ and influx of Na^+ and Ca^{2+}. This leads to a local de-polarization of the post-synaptic membrane which propagates towards the cell body (Figure 1B). Once enough de-polarizing spikes from the dendrites simultaneously reach the cell body, they can trigger the formation of an action potential at the axon initial segment (AIS), which in turn travels along the axon towards further downstream cells. Apart from the membrane depolarization, inflowing **calcium-ions** act as powerful second messengers that lie upstream of a multitude of signaling pathways. In the resting state, intracellular calcium concentrations are kept at the nanomolar range (50–100 nM), while they can rise up to 100-fold to the single-digit micromolar range upon synaptic stimulation (Maravall *et al*, 2000).

Although neurons are often entitled as the "fundamental units" of the brain, they do perform internal computations: synaptic input is integrated within the dendrites, which can be morphologically, electrochemically and functionally sub-compartmentalized. These dendritic sub-compartments can be hard to define; although pyramidal neurons as a particular example possess apical and basal dendrites with a distinct molecular makeup (Figure 1A) (Shah *et al*, 2010; Yuan *et al*, 2015).

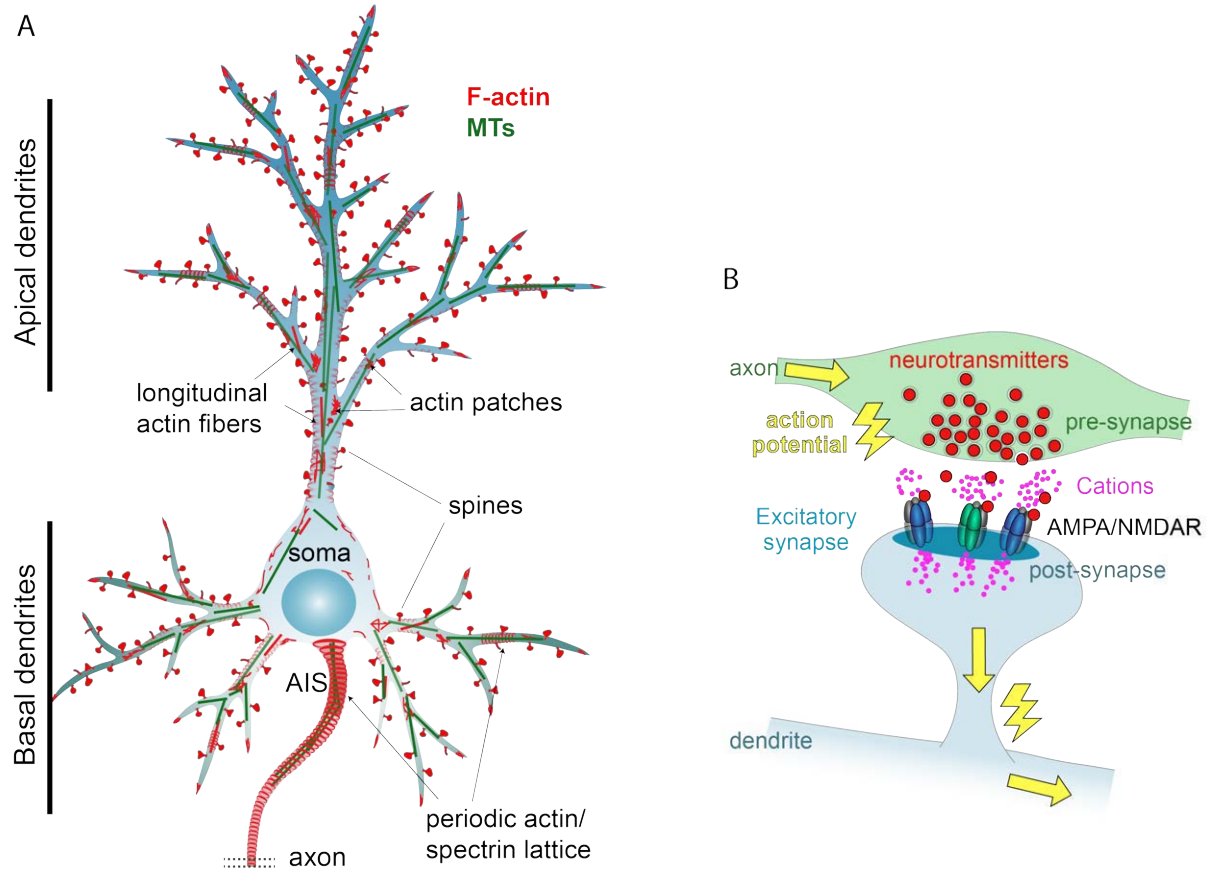

Figure 1. Neuronal and synaptic morphology. (A) Actin and MT distribution in pyramidal neurons. The actin cytoskeleton forms many different structures that shape neuronal morphology. Shown in red are longitudinal actin fibers and actin patches inside dendritic shafts, dendritic spines and the periodic actin-spectrin lattice that is spread throughout dendrites and axon. Shown in green are MTs, long cytoskeletal elements that are present all over the cell. AIS = axon initial segment. **(B) Signal transmission at an excitatory synapse**. An action potential traveling along an axon triggers neurotransmitter-release at the pre-synapse. Post-synaptic neurotransmitter receptors (AMPA / NMDA receptors) open upon ligand binding and allow cations to cross the membrane, which leads to a depolarization that propagates towards the cell body.

The highly polarized and compartmentalized morphology of neurons, together with the continuous remodeling of synaptic contacts, makes them especially reliant on a constant supply chain of compartment-specific proteins and other building blocks. As a consequence, neurons have developed a highly sophisticated trafficking system that mediates active, long-distance transport and local control of membrane and protein turnover (Hanus & Ehlers, 2016).

Neuronal protein transport

In neurons, most types of cellular organelles, which are usually found in the soma, are also spread throughout the dendrites, including the endoplasmic reticulum (ER), mitochondria, lysosomes and Golgi-like organelles (Figure 2) (Hanus *et al*, 2014; Mikhaylova *et al*, 2016).

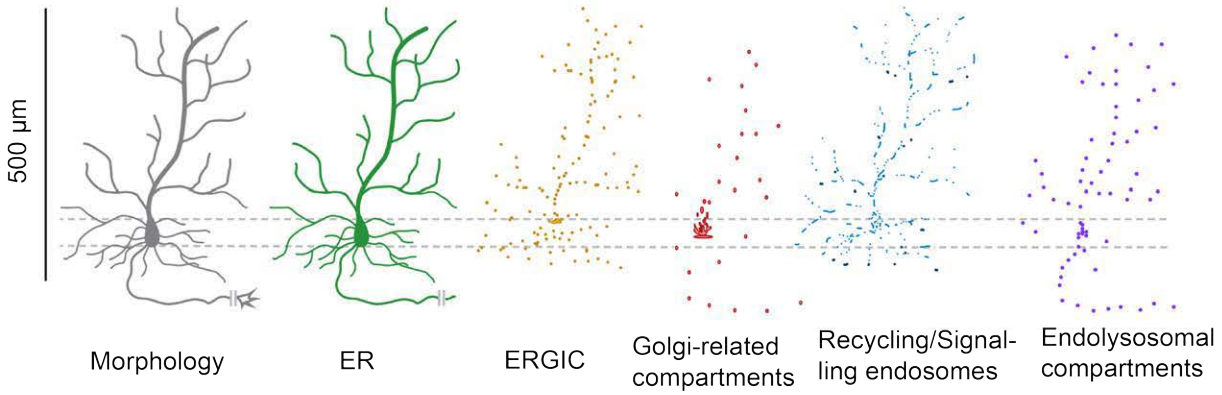

Figure 2. Distribution of secretory organelles in neurons. Most organelle compartments can be found spread throughout the neurites. The ER extends throughout the whole cell. ERGIC (ER to Golgi intermediate compartments) and recycling / signaling endosomes are mostly found in dendrites. Golgi-related and endolysosomal vesicles are present all over the cell. *Modified from Kennedy & Hanus (2019) Annu. Rev. Cell Dev. Biol. doi: 10.1146/annurev-cellbio-100818-125418*

Organelles and vesicles are constantly on the move to cover local demands of proteins, membrane components, and energy equivalents (ATP/GTP etc). All forms of active, directional transport require the presence of cytoskeletal elements, with **actin filaments** (F-actin) and **microtubules** (MTs) being the main mediators of neuronal protein transport. Microtubules, hollow tubes consisting of tubulin dimers, form thick and long bundles that stretch through the entire length of the dendrite, while actin forms much thinner and shorter filaments (Figure 1). As such, the cytoskeleton provides a network of tracks and walkways for so-called motor proteins, aptly named for their ability to actively transport intracellular cargo from one location to the other. Long-range intra-dendritic cargo transport is typically carried out via MTs and associated **kinesin** and **dynein** motors, whereas actin-based **myosin** motors regulate short-range transport and anchoring of cargo (Figure 3). Even though the different types of motor proteins have evolved independently, they broadly share a common structure, comprising a motor-domain with ATPase activity, a neck linker that translates conformational change upon ATP hydrolysis into forward movement, a flexible dimerization domain, and a cargo-binding domain (Figure 3A). Most of those motor proteins form dimers in order to processively walk along cytoskeletal tracks. They couple to their designated cargo via specific adapter proteins, or by direct interaction with the membrane lipids, whereby the same cargo vesicle may be bound by various kinds of motors (Figure 3B). Within the actin-rich environment of dendritic spines, the actin-based myosin motors are known to play an important role in the transport of vesicular cargo (Figure 4; Wang *et al*, 2008; Osterweil *et al*, 2005).

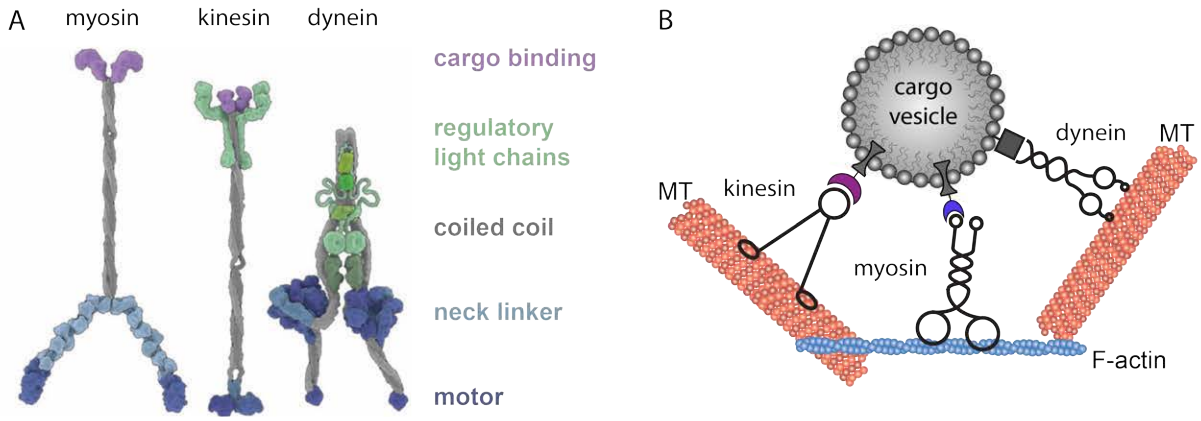

Figure 3. Motor proteins. (A) There are three major classes of processive motor proteins: The MT-based kinesins and dynein, and F-actin based myosins. They share a similar domain organization, including a motor domain (dark blue), neck linker (light blue), dimerization or coiled coil domains (grey), cargo binding domain (purple) and regulatory light chains (light green). *This figure was adapted from (Carter (2013) J Cell Sci; doi: 10.1242/jcs.120725)*. **(B)** Motor proteins attach to their respective cargo via specific adapter proteins. Different classes of motors might bind to the same cargo simultaneously.

The **processive myosin motors myosin V and VI** are implicated in the transport and recycling of transmembrane proteins, such as ion channels, receptors and transporters, into and out of dendritic spines (Esteves da Silva *et al*, 2015; Kneussel & Wagner, 2013).

Additionally to the transport of cargo within spines themselves, the actin cytoskeleton and associated myosins have been shown to mediate the anchoring of certain dendritic, MT-based cargos at the spine neck, which include mRNA, translational machinery, mitochondria, lysosomes, endosomes, and the ER (Figure 4) (Sung *et al*, 2008; Ligon & Steward, 2000; Martin & Ephrussi, 2010; Goo *et al*, 2017; Hangen *et al*, 2018; Wagner *et al*, 2011).

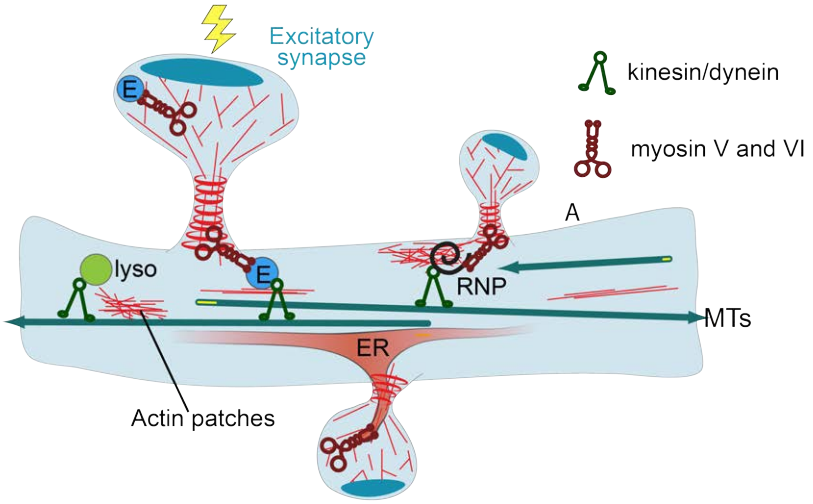

Figure 4. Schematic representation of dendritic trafficking systems. Fast, long distance transport is carried out by MT-based kinesin and dynein motors. Locally, certain cargo is taken over by actin-based myosin motors and stalled at or transported into dendritic spines. Lyso = lysosome. E = endosome. RNP = ribonucleoprotein particle.

In cerebellar Purkinje neurons, myosin Va is required for the transport and continuous localization of the ER to the dendritic spines, a hallmark of this cell type (Wagner *et al*, 2011). Apart from lipid- and membrane protein synthesis, the ER governs intracellular calcium homeostasis. It acts as a Ca^{2+} reservoir, providing both a source and a sink for intracellular calcium ions, and thus plays an important role in synaptic calcium signaling (Karagas & Venkatachalam, 2019). In pyramidal neurons of the hippocampus, the ER does not permanently reside inside individual spines, instead thin protrusions of the ER infrequently enter spines for few minutes to hours (Toresson & Grant, 2005). Although the function of those ER protrusions is not completely clear, they have been shown to induce large calcium spikes in stimulated spines, which led to a long-term depression of synaptic activation (Holbro *et al*, 2009). Whether myosin Va is also involved in this dynamic spine-localization of the ER in hippocampal neurons still remains to be explored (Figure 4).

Intriguingly, the stopping and anchoring of dendritic cargo at a spine neck is frequently observed after the spine received a synaptic input, dubbing this phenomenon "**activity-dependent targeting**". It is widely assumed that this accumulation of vesicles and organelles at recently activated spines is necessary to ensure sufficient local supply of materials and energy needed for the stabilization and potentiation of the synaptic contact (Chang *et al*, 2006; Redondo & Morris, 2011).
For example, activity-dependent targeting has been described for ribonucleoprotein particles (**RNPs**). For long-range transport, **mRNA** is packaged into RNPs containing specific targeting factors, and is delivered from the soma to the dendrite via MTs. Some RNPs are targeted to spines in an activity-dependent manner, which requires the presence of F-actin (Huang *et al*, 2007; Yoon *et al*, 2016). Likewise, myosin Va was shown to facilitate the accumulation of RNPs in spines (Figure 4) (Yoshimura *et al*, 2006). Activity-dependent capture and anchoring of mRNA, and subsequent mRNA translation, could constitute one mechanism to locally enrich proteins needed for potentiation of the activated spine. Similarly, it was shown that **lysosomes** can be stalled at the base of individual spines in response to local synaptic stimulation (Goo *et al*, 2017). In addition, synaptic activity can trigger the Ca^{2+}-dependent fusion of lysosomes with the dendritic plasma membrane, resulting in the local release of lysosomal proteases. These in turn activate matrix metalloproteinases, which are instrumental for the remodeling of the extracellular matrix to allow spine growth and potentiation (Padamsey *et al*, 2017). As a general model, activity-dependent targeting of cargo to activated synapses has been proposed to involve myosins located at the spine neck, which take up cargo that has been unloaded from passing MT-motors in a Ca^{2+}-dependent manner (Hanus *et al*, 2014).

One intriguing question that remains open is how exactly this "switch" of cargo from MT-based to actin-based transport (or anchoring) is accomplished. It was found that most intracellular cargoes are associated with different types of motors at the same time, which defines their transport characteristics and can explain the mechanism of motor switching (van Bergeijk *et al*, 2016). In this model, an inactive myosin motor would ride along on the surface of a kinesin-bound vesicle that is being transported along a MT, until that vesicle would reach an area rich in F-actin, where the myosin could become activated and initiate stalling or F-actin based transport (Figure 4). A recent study corroborated this model, using an artificial transport system consisting of peroxisomes coupled to constitutively active kinesin in primary neurons. Additional recruitment of constitutively active myosin V to the same organelle rapidly anchored them at the actin-rich axon initial segment, illustrating how **combined motor activity** can influence transport (Janssen *et al*, 2017). Interestingly, myosin V-induced anchoring of peroxisomes was sometimes observed along the axon, in dendrites and in the soma, suggesting that it occurs whenever cargoes with active myosin V encounter actin-rich regions (Janssen

et al, 2017). In addition to active anchoring mechanisms, the presence of dense cytoskeletal structures, like dendritic F-actin patches, and other organelles can physically hinder cargo trafficking and induce stalling (Katrukha *et al*, 2017; Sood *et al*, 2018; Bommel *et al*, 2019).

Actin in dendrites

Actin is a versatile and ubiquitous cytoskeletal protein that plays a major role in the maintenance of neuronal polarity. A myriad of actin binding proteins (ABPs), summarized in (Konietzny *et al*, 2017), dynamically shapes and regulates the actin cytoskeleton in response to intrinsic and extrinsic stimuli. Monomeric actin can spontaneously polymerize into filaments under the right circumstances (e.g. a critical actin concentration and presence of salt). The polymerization reaction requires the - energetically unfavorable - formation of a "nucleus", i.e. actin dimers and trimers (Figure 5A). Furthermore, inside the cell, actin monomers are mostly bound by specific ABPs such as profilin or cofilin, which buffer the available actin and affect its propensity to polymerize (Figure 5B). Thus, as the rate-limiting step in actin polymerization, nucleation is a crucial point in the regulation of F-actin dynamics. Several actin nucleators, including formin-homology (FH) proteins and the Arp2/3-complex, facilitate this process. **Formins** polymerize single longitudinal filaments (Figure 5C), whereas the **Arp2/3-complex** is the only known regulator for actin branching (Figure 5D). It requires an existing actin filament, from which it nucleates a new filament branch (Smith *et al*, 2013). The Arp2/3-complex is activated by membrane-associated interactors, such as neuronal Wiskott–Aldrich Syndrome protein (N-WASP) (Korobova & Svitkina, 2010). Arp2/3-complex-dependent polymerization of branched actin networks generates widespread pushing forces against the plasma membrane, accounting for its prominent role in the maturation and enlargement of dendritic spines (Spence *et al*, 2016; Bosch *et al*, 2014). Another mechanism of Arp2/3 activation involves the F-actin stabilizing protein **cortactin**, which can bind and activate the Arp2/3-complex (Figure 5D) (Kowalski *et al*, 2005; Korobova & Svitkina, 2008).

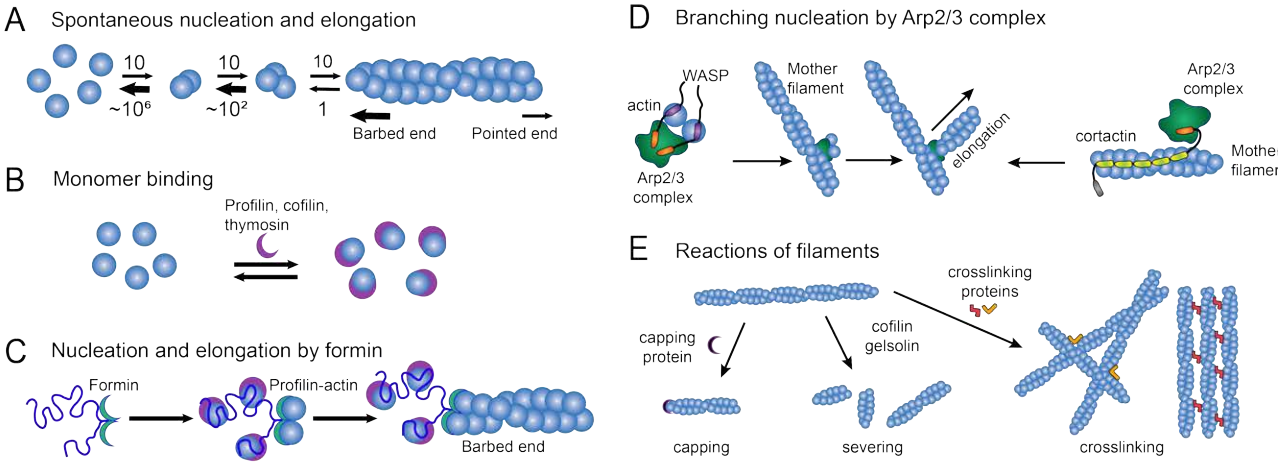

Figure 5. F-actin polymerization and shaping of actin-based structures. (A) Spontaneous nucleation and elongation of actin filaments. **(B)** Monomer-binding ABPs buffer the available actin pool. **(C)** Nucleation and elongation by formin. **(D)** Branching nucleation mediated by the Arp2/3 complex. **(E)** Reactions of actin filaments: Capping reduces spontaneous deploymerization; filaments are actively severed by proteins such as cofilin and gelsolin; crosslinking of F-actin can create dense networks or parallel bundles. *Modified from Pollard & Cooper (2009) Science 10.1126/science.1175862*

Individual actin filaments can be stabilized by capping proteins that prevent depolymerization, or be subjected to severing by ABPs such as cofilin or gelsolin (Figure 5E). Further, crosslinking ABPs can shape longitudinal, parallel F-actin bundles, or branched and cross-linked networks (Figure 5E). The latter is especially prevalent in the so-called **actin cortex**, a thin, specialized layer of F-actin and other proteins associated with the inner face of the plasma membrane. Here, the F-actin network is involved in stabilizing as well as dynamically shaping the membrane, including the regulation of processes such as endo- and exocytosis. Moreover, it serves as an anchoring point for both intracellular and transmembrane proteins, including receptors and cell adhesion molecules. Like in any other cell type, many functions of **actin in neurons** relate to its ability to polymerize and depolymerize in response to cellular signaling, most notably synaptic activity and receptor signaling.

With respect to neuronal dendrites, perhaps the most striking and best-described F-actin-based structures are so-called **spines**, small membranous protrusions that harbor synapses (Figure 1, Figure 4). For a long time, most research that treated actin in dendrites was focused on dendritic spines, since those compartments contain large accumulations of actin filaments that can be readily visualized using electron- and fluorescence microscopy. However, thanks to the development of super-resolution microscopy in the past few years, so far unknown structures of the actin cytoskeleton have been discovered: actin patches, longitudinal actin fibers, and "actin rings" (Figure 1, Figure 4). **Actin rings**, now more descriptively called the "membrane-associated periodic skeleton" (MPS), are periodic cortical actin-spectrin structures that are present in axon, dendrites and even in necks of dendritic spines, as our group has recently shown (Xu *et al*, 2013, D'Este *et al*, 2015; Bär *et al*, 2016; He *et al*, 2016). These structures are thought to support neurite shape, help in organization of proteins along the plasma membrane (Xu et al., 2013), stabilize the underlying MT cytoskeleton (Qu *et al*, 2016) and could influence spine neck elasticity during transport of organelles (Bär *et al*, 2016). **Longitudinal actin fibers** are long bundles of F-actin that are localized inside dendritic shafts (D'Este *et al*, 2015; Bär *et al*, 2016). Their properties and functions have so far not been investigated in detail. **Actin patches** are accumulations of branched F-actin (Willig *et al*, 2014) in the µm size range, and were suggested to serve as outgrowth points for filopodia (Korobova & Svitkina, 2010). In the course of this doctoral thesis, I and my colleagues have furthermore shown that a subset of these actin patches is associated with shaft synapses, and that they regulate dendritic cargo trafficking (Bommel *et al*, 2019).

At dendritic spines, **calcium signaling** rapidly impacts most cellular processes, including F-actin remodeling, cargo transport and motor activity. The dynamic, activity dependent remodeling of the F-actin cytoskeleton, which can either lead to the strengthening or the loss of the synaptic contact, has been well described (Okamoto *et al*, 2004). Calcium can act directly on target proteins, or induce signaling cascades via the ubiquitous Ca^{2+}-sensor calmodulin (CaM, Figure 6A), which rapidly activates CaM-kinases and calcineurin (Ca^{2+}/CaM-dependent phosphatase). Calmodulin-dependent kinase **CaMKII**, at the center of many signaling pathways, regulates formation, growth, and branching of dendrites locally via Rho-GTPases**,** which modulate cytoskeleton turnover, and globally via activation of transcription factors (Redmond & Ghosh, 2005). Apart from this, CaMKIIβ possesses a direct F-actin binding ability, enabling the dodecameric holoenzyme to cross-link and stabilize actin networks (Lin & Redmond, 2008; Na *et al*, 2016). Activated CaMKII is then released from F-actin, which constitutes one of the many ways to link Ca^{2+}-signaling to the regulation of the actin cytoskeleton. Several other ABPs are known to be directly influenced by CaM/Ca^{2+}, including Cobl (Hou *et al*, 2015), spectrins, actinin, ADF/cofilin and gelsolin (Oertner & Matus, 2005).

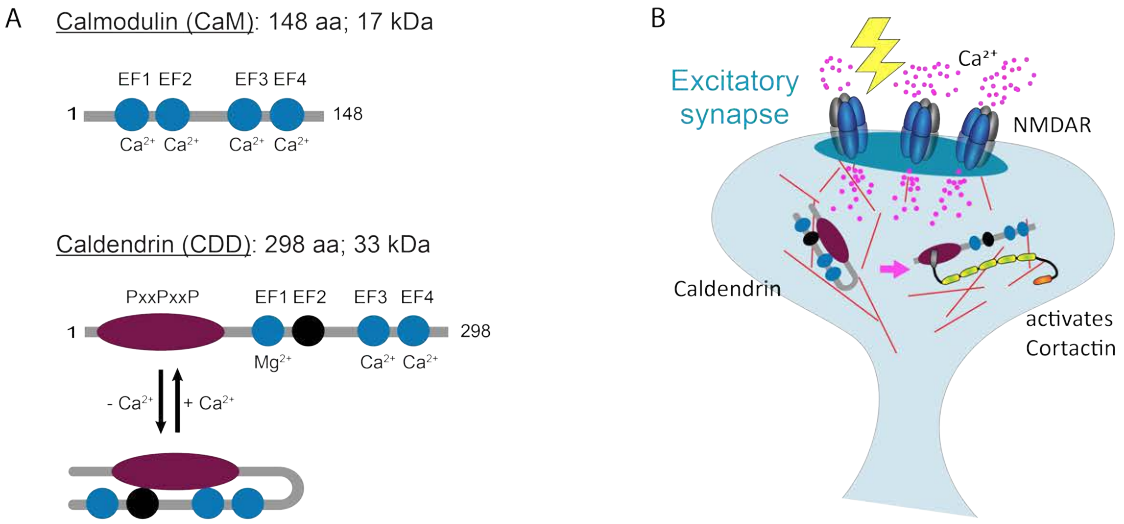

Figure 6. Calcium binding proteins and calcium signaling in synaptic activation. (A) Calmodulin is a small, ubiquitous calcium sensing protein. It contains four EF-hand motifs that cause a conformational change upon calcium binding that regulates CaM interactions. Caldendrin is related to CaM; it contains four EF-hand motifs, two of which are functional calcium sensors (EF3 + EF4), and one has a high affinity for magnesium (EF1). It further contains an unstructured, proline (P)-rich N-terminus, which was shown to interact with SH3 domains of various proteins. In the absence of calcium, CDD exists in a folded, inaccessible conformation. **(B)** In the postsynapse, CDD is activated by inflowing calcium ions during synaptic activation. It then binds and activates the ABP cortactin, which can initiate F-actin branching and protects actin filaments from severing enzymes.

Additionally, our group has recently described a novel mechanism which directly couples postsynaptic calcium signaling to actin remodeling via an interaction between the calcium-binding protein **caldendrin** and the ABP **cortactin** (Mikhaylova *et al*, 2018). Caldendrin (CDD), which is evolutionarily related to CaM, is expressed in neurons of the hippocampus, cortex and cerebellum, where it is enriched in dendritic spines. Like CaM it contains four canonical EF hand motifs, two of which are functional and allow it to bind to calcium (Figure 6A). It additionally contains a unique, proline-rich N-terminus, which does not show any sequence similarity to other known proteins (Figure 6A). Previous work has shown that, in the absence of calcium, CDD assumes an auto-inhibited conformation, which is opened up upon calcium binding, and thus becomes accessible for its interacting partners (Mikhaylova et al, 2018). The open, calcium-bound CDD then binds and activates cortactin. Cortactin itself binds directly to F-actin, whereby it stabilizes the filament and protects it from severing enzymes such as cofilin, and on the other hand it recruits the Arp2/3 complex to induce actin branching as mentioned above (Figure 6B) (Mikhaylova *et al.* 2018).

It is important to note that calcium signaling is not restricted to individual activated spines, but that calcium and calcium-activated proteins can diffuse out of the spine and into the **dendritic shaft**, where they may affect the cytoskeleton and associated transport processes. Several ABPs, including cortactin, and even actin filaments themselves have been described to be released from the spine head into the dendritic shaft upon synaptic activation (Hering & Sheng, 2003; Honkura *et al*, 2008). Frequently, accumulations of branched actin filaments can be observed at the base of dendritic spines, which extend throughout the dendritic shaft, and which are also subject to activity-dependent remodeling (Schätzle *et al*, 2018). These have been shown to sterically affect MT growth (Schätzle *et al*, 2018), and may likewise affect vesicle and organelle trafficking, or play a role in activity-dependent targeting of plasticity-related products.

Myosin motors and caldendrin

Like other motor proteins, myosins consist of a dimer of large **heavy chains**, and a variable number of stabilizing **light chains** (Figure 7A). The heavy chains contain a motor domain, followed by a coiled coil or linker region, and a cargo binding domain. Myosin light chains are small calcium sensing proteins, in the case of myosin V and myosin VI this role is taken over by the ubiquitous protein **calmodulin**. They bind to the neck region of each heavy chain, stabilizing the lever arm and enabling processive movement.

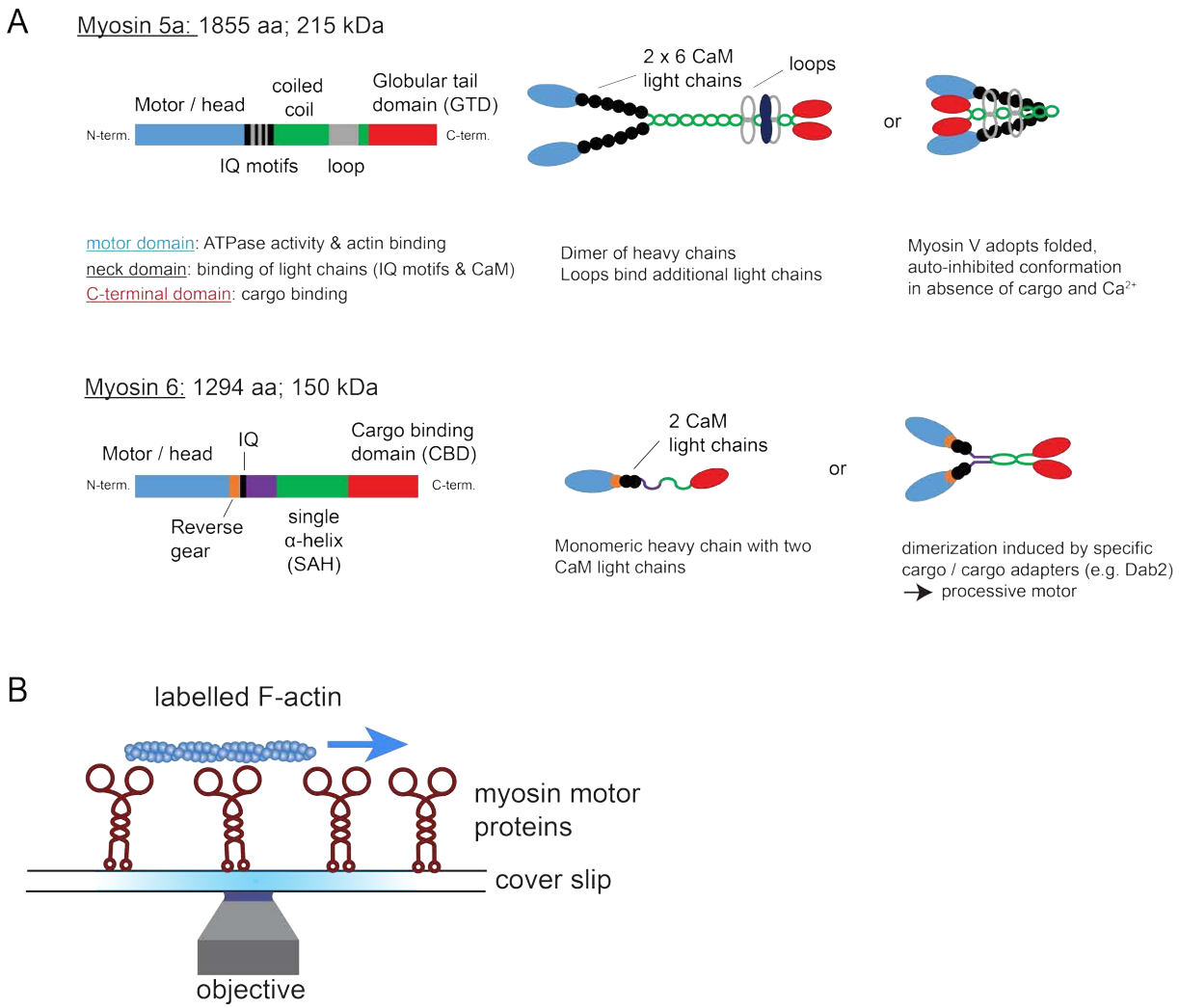

Figure 7. Processive myosin V and myosin VI motor proteins and their regulation. (A) Schematic overview of myosin V and myosin VI domain organization. Both proteins are actively processive as a dimer. They share a similar domain structure, with a motor domain that binds actin and has ATPase activity, IQ-motifs that bind calmodulin (CaM), and a cargo binding domain that binds to specific adapter- and cargo proteins. Myosin V is constitutively dimerized by its coiled coil domains, and adapts a folded, auto-inhibited conformation in the absence of calcium or cargo. Myosin VI does not dimerize on its own but requires the binding of cargo or adapters. As a monomer, it can function as a tether instead of a processive motor. **(B)** Schematic representation of a gliding assay setup to assess myosin activity. Motors are attached to a glass-coverslip, which allows the observation of "gliding" actin filaments.

Both myosin V and VI contain CaM binding sites called "**IQ motifs**", as the consensus sequence (IQ*XXX*RG*XXX*R) starts with isoleucine (I) and glutamine (Q), whereas *X* can be occupied by any amino acid. In the case of myosin VI, each heavy chain contains two IQ motifs. Mysosin VI can exist as a monomer, fulfilling an anchoring function, or it can be dimerized with the help of adapter or cargo proteins, turning it into a processive motor (Figure 7A). Myosin V, on the other hand, contains a coiled coil domain that mediates dimerization of the two heavy chains, each of which contains six IQ motifs (Figure 7A).

There is some dissent in the literature as to how the calcium-bound state of CaM influences the function of myosin V as a processive motor. In the absence of calcium, all six of the IQ motifs of myosin V bind calcium-free CaM (apoCaM) (Wang *et al*, 2000). One method to assess myosin V motor activity are *in vitro* **gliding assays**, in which the myosin motor is bound to a surface, and labeled actin filaments are added to observe "gliding" on top of the myosin motor domains (Figure 7B). These assays have demonstrated that, in the absence of calcium (EGTA buffer), the motor is active and processively transporting the actin filaments. Addition of calcium abolishes the filament gliding, i.e. motor activity, in this assay. Additional supply with CaM can rescue motor activity to some extent, although sliding velocities were still reduced. Various publications report differing calcium concentrations which can cause inhibition of the myosin motor, ranging from 1 µM over 5 µM to 10 µM of Ca^{2+} (Nguyen & Higuchi, 2005; Trybus *et al*, 1999; Nascimento *et al*, 1996; Homma *et al*, 2000). This is generally attributed to some of the CaM light chains dissociating from the lever arm in high calcium concentrations, thus rendering it unstable and unable to translate the force generated by ATP hydrolysis into processive motility (Krementsov *et al*, 2004).

Apart from that, it was shown that low µM concentrations of calcium greatly stimulate the **actin-activated ATPase activity** of both tissue-purified as well as recombinant full-length myosin V in solution (Nascimento *et al*, 1996; Krementsov *et al*, 2004). This is attributed to the fact that in the absence of calcium, myosin V can adopt a folded, auto-inhibited conformation, in which the cargo-binding domain directly binds to the motor domains, thus rendering the motor inactive (Wang *et al*, 2004; Liu *et al*, 2006; Thirumurugan *et al*, 2006) (Figure 7A). There is compelling evidence that the observed activation of the myosin motor in the presence of calcium is due to a conformational change that takes place in some of the bound CaM upon calcium binding, especially the one bound to the first IQ motif. This change is thought to translate to a conformational change in the motor domain, which dissociates the cargo binding domain from the motor domain, and thus leads to the opening and activation of the whole myosin protein (Trybus *et al*, 2007; Shen *et al*, 2016).

The question how **calcium-dependent regulation of myosin V** plays out in the *in vivo* situation is still very much unclear. For example, the fact that myosin V fully occupied with apoCaM shows motility in gliding assays is likely due to the surface adsorption, which could mimic cargo binding and artificially force the protein into the open conformation, or cause further unexplained conformational changes. From what is known so far, apoCaM-myosin V would likely be in the auto-inhibited, inactive state *in vivo*. Further, the aspects that calcium binding to CaM associated with myosin V both activates ATPase activity and inhibits myosin motility still need to be consolidated. *In vivo*, the local concentration of free calcium will have multi-layered effects on myosin V, providing a way to fine-tune myosin activity depending on both the rate of calcium-transition in the IQ-bound CaM, and the rate of calcium-induced CaM dissociation.

To add yet another layer to calcium-dependent regulation of myosin activity, during the course of this study I found that myosin also interacts with the **calcium-binding protein caldendrin** (CDD). We had previously investigated caldendrin for its role in actin dynamics of dendritic spines, through interaction with the actin binding protein cortactin (Mikhaylova *et al*, 2018). In order to gain some insight into the extended interactome of caldendrin, we performed a mass-spectrometric analysis of brain-specific caldendrin interactors during this study, and found that myosin proteins were prominently present, including myosin V and VI. We hypothesize that caldendrin, which becomes activated in dendritic spines during high calcium spikes induced by synaptic signaling (Mikhaylova *et al*, 2018), might play a role in regulating myosin-based activity-dependent targeting of synaptic cargoes.

Synaptopodin and the spine apparatus

Parts of this chapter have been adapted from (Konietzny et al. 2019).

As briefly mentioned above, the ER is one of the organelles prominently present in dendrites, where it regulates lipid and membrane protein synthesis, and notably also calcium homeostasis. In pyramidal hippocampal neurons, the highly complex ER spans the entire cell, including soma, axon and dendritic tree, and thin ER protrusions are frequently observed to enter dendritic spines for short time spans (Figure 4) (Toresson & Grant, 2005). In those cells a subset of spines contains a complex ER-based organelle called the **spine apparatus** (SA / Deller et al., 2003). The SA is usually localized in the spine neck or at the base of the spine head and consists of laminar ER stacks with intervening electron-dense plates, connected to the main ER network (Figure 8A-C). It serves as a calcium store and is important for synaptic plasticity (Deller *et al*, 2003).

The cytosolic protein **synaptopodin** is an essential component of the SA structure. Electron microscopy (EM) imaging has shown that it is deeply embedded in the SA, localizing to the dense spaces between the laminar ER stacks (Figure 8B, C). Dendritic spines of synaptopodin K.O. mice are completely devoid of the SA, while transient entry of single ER tubules can still be observed, and re-expression of synaptopodin is sufficient to rescue the SA (Deller *et al*, 2007, 2003; Vlachos *et al*, 2013). Accordingly, cerebellar Purkinje neurons, which do not express synaptopodin, do not form the SA despite having ER tubules in every single spine. Of note, synaptopodin is also required for the establishment of a similar ER-based structure, called the **cisternal organelle**, in the axon initial segment (Bas Orth *et al*, 2007). Expression of synaptopodin, which is restricted to renal podocytes and telencephalic neurons in the brain, is developmentally regulated and coincides with synaptic maturation (Mundel *et al*, 1997; Czarnecki *et al*, 2005). Synaptopodin itself lacks a clear domain organization, contains several predicted disordered regions, and is known as an actin and α-actinin binding protein (Kremerskothen *et al*, 2005; Asanuma *et al*, 2005; Chalovich & Schroeter, 2010).

In humans and rodents, three splice isoforms of synaptopodin have been identified, but only the shortest isoform is found in the brain (Asanuma et al., 2005; Chalovich and Schroeter, 2010 / Figure 8D). Previously, an interaction between the long splice isoform of human synaptopodin (identifier: Q8N3V7-2; 903 aa) and α-actinin-2 has been suggested to mediate localization of (overexpressed) synaptopodin at spines via a binding motif at the C-terminus (Kremerskothen *et al*, 2005) (Figure 8D). However, this isoform is not endogenously expressed in brain, and several other studies reported that the short splice isoform of mouse synaptopodin, lacking the proposed targeting domain, is also clearly enriched at spines (Figure 8D; Korkotian et al., 2014; Vlachos et al., 2009). Asanuma et al. showed that this short splice isoform contains two α-actinin-2 and α-actinin-4 binding sites of its own (Asanuma *et*

al, 2005). Yet, α-actinin is non-selectively enriched in all types of spines, so its role in localizing synpatopodin and the SA to specific, individual spines is questionable (Matt *et al*, 2018; Hodges *et al*, 2014; Nakagawa *et al*, 2004).

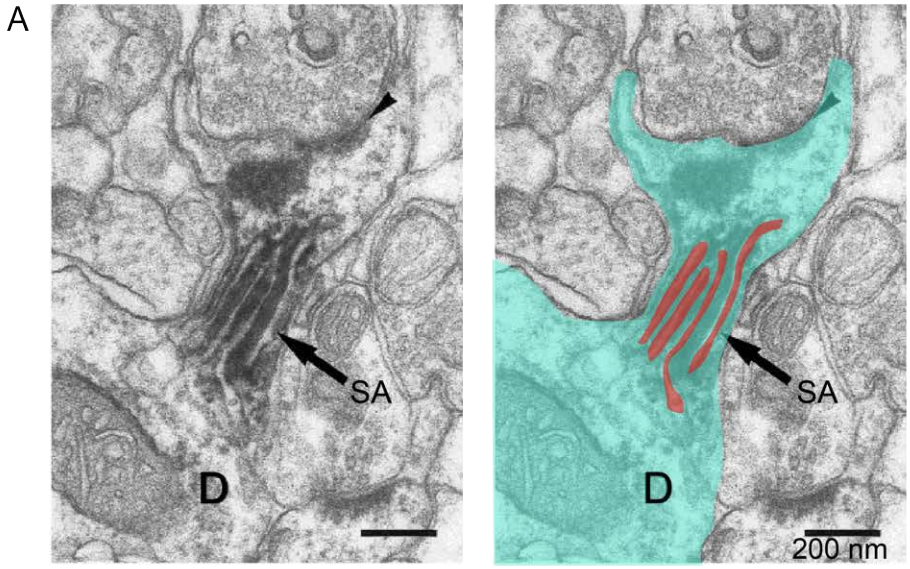

D = dendrite, SA = Spine Apparatus

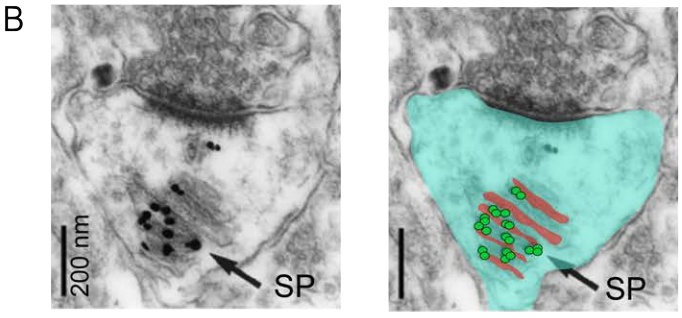

SP = Synaptopodin

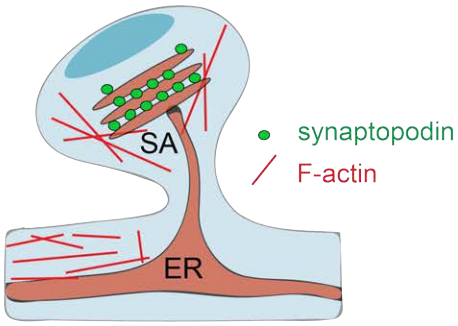

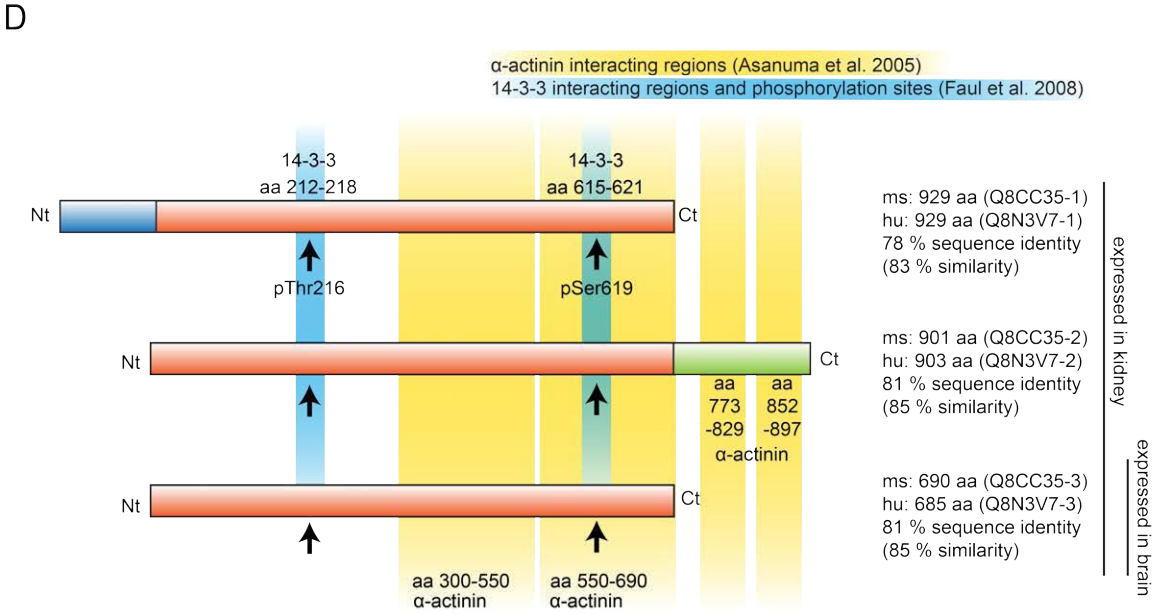

Figure 8. Synaptopodin and the spine apparatus. (A) Electron-microscopy (EM) image of a dendritic spine containing the spine apparatus. **(B)** EM image of a spine head containing the SA, with synaptopodin visualized by immunogold labelling. **(C)** Schematic representation of the SA structure as an extension of the main ER. **(D)** Overview of described synaptopodin splice isoforms in mice and humans, interaction partners and phosphorylation sites. Isoform 1 has a unique N-terminus, and isoform 2 a unique C-terminus, while all of them share the same middle region. It was shown that only the shortest isoform is expressed in the brain. **(A)** *Adapted from Deller et al. (2000) J. Comp. Neurol. 10.1002/(sici)1096-9861(20000306)418:2<164::aid-cne4>3.0.co;2-0.* **(B)** *Adapted from Deller et al. (2007) Annals of Anatomy, 10.1016/j.aanat.2006.06.013.* **(D)** *adapted from Konietzny et al. (2019) J. Cell Sci. 10.1242/jcs.230177.*

It has been demonstrated that about twenty to thirty percent of dendritic spines are positive for synaptopodin, and that it is more frequently present in a subset of spines with a large spine head volume (Vlachos *et al*, 2009; Holbro *et al*, 2009). Interestingly, the presence of synaptopodin correlated with synaptic strength, indicating that SA-containing spines might have different plastic properties (Vlachos *et al*, 2009; Korkotian *et al*, 2014). Further, synaptopodin K.O. mice show impaired long-term potentiation (LTP) of dendritic spines, and impaired spatial learning (Deller *et al*, 2003; Korkotian *et al*, 2014).Notably, synaptopodin mRNA and protein levels are regulated by neuronal activity. For example, it has been shown that in dentate granule cells synaptopodin expression is upregulated following LTP *in vivo* (Yamazaki *et al*, 2001). Moreover, a recent study has found that synaptopodin is required for cAMP-mediated LTP in developing neurons and that it is most likely a substrate of protein kinase A (PKA), which becomes activated during LTP (Zhang *et al*, 2013). Taken together, these data suggest that synaptopodin acts as a powerful tool to induce formation of the SA in dendritic spines, and it is very likely that synaptopodin expression, localization, function, and stability are highly regulated.

Despite the importance of the SA in synaptic function, there are still many open questions about the origin of this organelle. For instance, it is unclear how synaptopodin and the SA are targeted to a selected subset of dendritic spines, or which molecular mechanisms regulate SA localization.

Dissociated primary hippocampal neurons as a model system

Neurons are a challenging cell type to work with. Especially the neurons of the brain are hard to access or visualize *in vivo*, and it is very difficult to obtain live human brain tissue for experiments. Although impressive progress has been made in the recent years to culture human neuronal cell types from induced pluripotent stem cells (Yu *et al*, 2014), this technique is still under development, and it is not yet possible to obtain large quantities of defined neuronal subtypes through this method in a cost- and time-effective manner. For now, a well-established model system to investigate the molecular and cellular biology of CNS neurons are dissociated cultures from specific brain regions (e.g. cortex, hippocampus, cerebellum etc.) of rat or mouse embryos (Poindron *et al*, 2005; Molnár, 2011). In general, the brains of embryos are dissected two to four days before birth, the desired brain region is isolated and the cells within the tissue are dissociated using proteolytic enzymes and/or mechanical force. The dissociated cells can then be cultivated *in vitro*, where they continue their maturation process and develop an adult phenotype. Conventionally the age of such cultures is delineated in “days *in vitro*”, or DIV. Hippocampal cultures from rat embryos, which I used throughout this study, develop random neuronal networks and functional synapses around DIV8-10, are considered “young” from DIV 16-21, and “mature” from DIV21 onwards (Frese *et al*, 2017).

Working objective based on the current state of knowledge

In light of novel discoveries related to the role and organization of dendritic F-actin, in my thesis work I focus on the mechanisms and molecular players that interact with and rely on the **actin cytoskeleton**, thereby influencing dendritic protein transport and synaptic function.

The central aim of my thesis is to investigate the role of actin and processive myosin motors in regulating neuronal organelle trafficking. Specifically, I am addressing the following questions:

- What is the role of actin patches and myosin motors in the localization of endolysosomal compartments in dendrites?

- What are the mechanisms targeting the spine apparatus to selected spines?

- How is calcium-signaling involved in the regulation of the myosin V motor protein?

Results and Discussion

Chapter 1: Actin patches and dendritic transport

The following work has been published in (Bommel & Konietzny et al, 2019). Parts of the presented experimental work have been conducted with the help of Bas van Bommel and Julia Bär from the ZMNH (Hamburg), and Oliver Kobler from the LIN (Magdeburg).

In recent years, advanced microscopy techniques have led to the discovery of novel F-actin based structures in neurites. Previously undescribed patches and bundles of F-actin have been observed along the lengths of dendrites, and were suggested to serve as outgrowth points for filopodia (Willig *et al*, 2014; Korobova & Svitkina, 2010), although their functional relevance has so far not been investigated in detail. Here, we have mapped the dendritic actin cytoskeleton of mature hippocampal neurons and found local enrichments of F-actin networks within the dendritic shaft and at the base of dendritic spines. We hypothesized that these structures influence cargo trafficking, and tested this hypothesis using lysosomes as an example of mobile vesicular organelles.

Dendritic actin patches are associated with excitatory synapse markers

To map the distribution of F-actin in dendrites, we initially performed immunostainings of DIV17 neurons with the F-actin dye phalloidin-Atto647N and for the dendritic microtubule marker MAP2. Confocal imaging suggested the presence of F-actin enrichments in dendritic shafts (Bommel *et al*, 2019). These F-actin patches develop with the maturation of primary neuronal cultures, and were first detectable at approximately DIV6. Their time of appearance coincided with synaptogenesis, and co-localization with the presynaptic marker bassoon indicated a spatial relationship with synapses (Bommel *et al*, 2019). This close proximity to presynaptic sites extended to more mature neurons (DIV 16), where the actin patches were also positive for the excitatory synapse marker homer1. The presence of bassoon and homer1 suggests that about two thirds of the dendritic actin patches are part of functional, excitatory shaft synapses (Bommel *et al*, 2019).

Dendritic actin patches have similar characteristics to spinous rather than axonal F-actin

In contrast to actin in spines, the structural composition of F-actin in dendritic patches was so far unknown (Bosch *et al*, 2014; Konietzny *et al*, 2017; Mikhaylova *et al*, 2018). In order to characterize the type of filaments present in dendritic actin patches, I performed pharmacological inhibitor experiments followed by immunostainings. The inhibitors used were Latrunculin A, SMIFH2 and CK666. Latrunculin A (LatA) is a toxin that binds to actin monomers and thus inhibits polymerization. This means it is not actively severing existing F-actin, but because most F-actin structures have a high physiological turnover rate, they will gradually disappear upon LatA treatment. SIMFH2 is a specific inhibitor of formin-mediated nucleation and polymerization of linear F-actin (Rizvi *et al*, 2009). CK-666 binds to the Arp2/3 complex and stabilizes its inactive conformation, thus specifically inhibiting Apr2/3-mediated nucleation and F-actin branching (Hetrick *et al*, 2013). Interestingly, I found that spine-base associated actin patches were generally more sensitive to pharmacological perturbations than shaft-associated patches: upon depolymerization of F-actin induced by a 30 min treatment with latrunculin A (LatA; 5 µM), spine-base associated F-actin loci disappeared almost completely, while the

number and intensity of shaft associated patches also decreased significantly, but to a much lower extent (Figure 9A-F). I distinguished between spine-associated and shaft-associated patches, as the spine-associated patches might be influenced to a greater extent by synaptic activity in their associated spine, and therefore have different characteristics than shaft-localized actin patches (Figure 9B). The fact that small F-actin puncta still remained even after 30 min LatA treatment indicated that a stable pool of actin filaments is present within dendritic actin patches. Using fluorescence-recovery after photobleaching (FRAP) analysis, it was shown by my colleague Bas van Bommel that the stable pool makes up about 20 % of the F-actin inside dendritic actin patches, which is very similar to what is observed inside dendritic spines (Bommel *et al*, 2019). I next asked what types of filaments are present at dendritic actin patches using selective inhibitors of the Arp2/3 complex (CK666; 50 µM for 2 h) and formins (SMIFH2; 30 µM for 90 min). Both led to a strong reduction in the number of spine-associated patches, and a mild decrease in shaft-associated patches (Figure 9A - F), while patch size and intensity remained largely unchanged (Figure 9A-F).

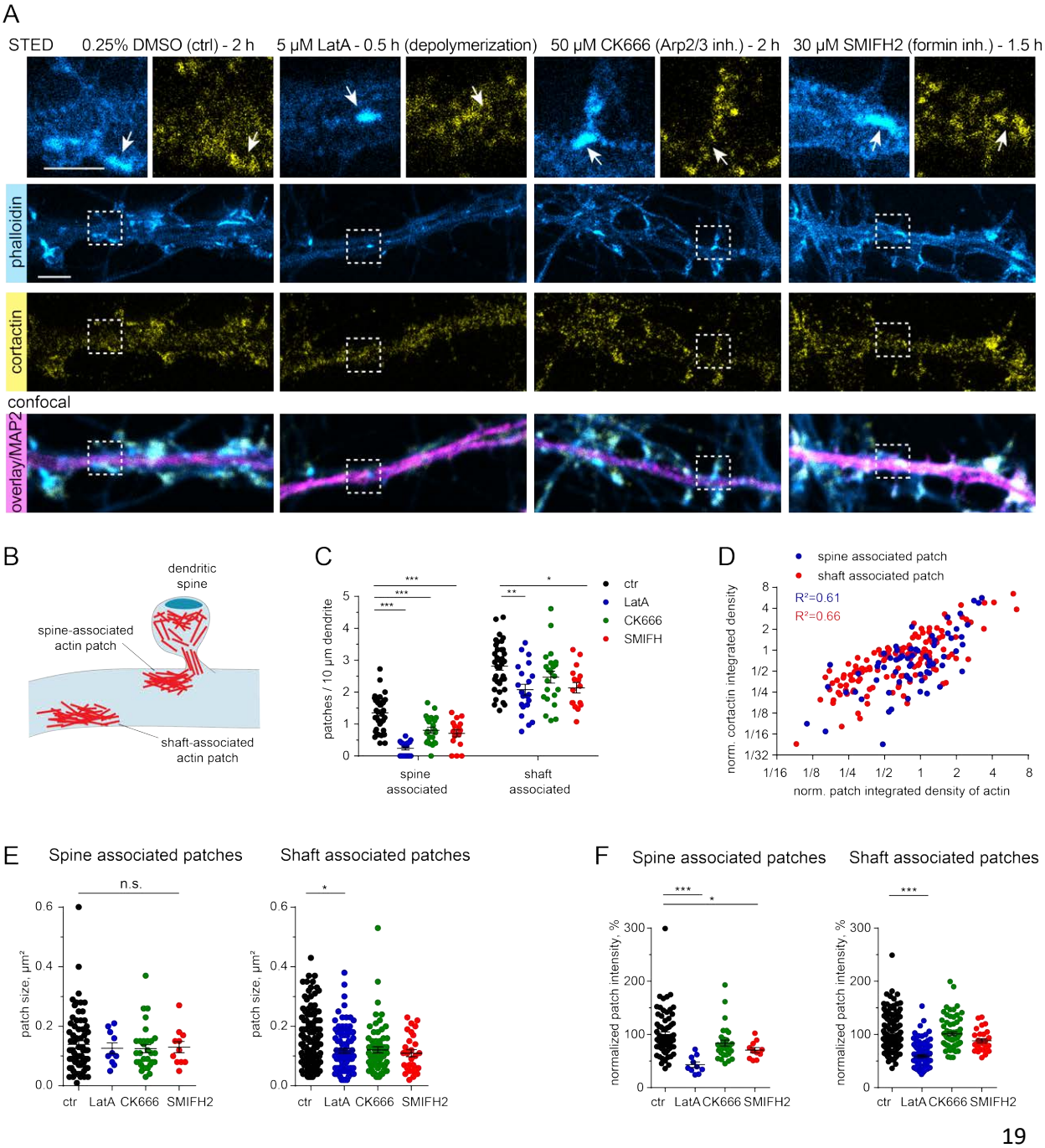

Figure 9. Actin patches have a high actin turnover rate and contain both branched and linear filaments
(A) Representative STED and confocal images of DIV21 rat hippocampal neurons treated with either DMSO (solvent control) for 2 h, the G-actin sequestering agent latrunculin A (LatA, 5 µM) for 0.5 h, an Arp2/3 inhibitor (CK-666, 50 µM) for 2 h, or a formin inhibitor (SMIFH2, 30 µM) for 1.5 h, and labelled for the dendritic microtubule marker MAP2, cortactin and phalloidin-Atto647N. Zoom-ins show higher magnification image with arrow pointing to actin patches. LatA leads to the depolymerization of most, but not all, actin patches, indicating the presence of stable and non-stable actin pools within patches. Scale bar: 2 µm, 1 µm (zoom in).
(B) Quantification of actin patch density along dendritic segments as shown in (**A**), with relation to their location at the spine base or within dendritic shafts. Pharmacological treatments reduced the number of spine- and shaft-associated actin patches. The reduction in both CK-666 and SMIFH2 treated samples suggest a mixed organization of branched and longitudinal actin filaments. 1-way ANOVA with Dunnett's post hoc test. * p=0.01, ** p=0.002, *** p<0.001. *n= 36 (ctr), n= 21 (LatA), n=22 (CK666), n=16 (SMIFH2) dendritic segments of 23 (ctr), 18 (LatA), 19 (CK666), 15 (SMIFH2) cells in 3 independent experiments.*
(C) Correlation of actin patches co-localizing with cortactin as shown in (**A**). The amount of cortactin correlates with the actin intensity for both spine- and shaft-associated actin patches (in DMSO control group). Data is plotted on a logarithmic scale. Pearson correlation. *n=67 (spine associated), n=132 (shaft associated) patches in 20 dendrites of 13 cells in 2 independent experiments*
(D) Quantification of actin patch size in control (DMSO), LatA (5 µM for 30 min), CK666 (50 µM for 2 h), and SMIFH2 (30 µM for 90 min) treated neurons. Patch size for spine associated patches is not significantly changed after treatment. The size of shaft-associated patches was reduced after LatA treatment. 1-way ANOVA with Dunnett's post hoc test. * p=0.02. n=71 (ctr), n=10 (LatA), n=31 (CK666), n=11 (SMIFH2) spine associated patches and n=151 (ctr), n=95 (LatA), n=68 (CK666), n=28 (SMIFH2) shaft-associated patches in 24, 17, 12, 6 dendrites of 16, 15, 10, 6 cells in 2 independent cultures.
(E) Quantification of normalized actin patch intensity as in (C) Normalized actin patch intensity for spine associated patches was reduced in LatA (5 µM for 30 min) and SMIFH2 (30 µM for 90 min) treated groups. For shaft associated patches it was only reduced after LatA treatment. 1-way ANOVA with Dunnett's post hoc test. * p=0.03, *** p<0.001. Same n as in (C)

From this I concluded that dendritic actin patches contain both linear, formin nucleated as well as branched, Arp2/3 nucleated F-actin, with spine-associated F-actin patches having a higher turnover-rate than shaft-associated patches. Moreover, both spine- and shaft-associated actin patches showed a correlation between the amount of F-actin and cortactin, which marks branched and stable actin filaments and is also enriched inside dendritic spines (Figure 9A, D). Since spine-associated patches had a higher turnover rate and were less stable than shaft-associated patches, we hypothesize that spine-associated patches are more often subjected to activity-dependent remodeling, and might be shorter lived than shaft-associated patches. Further, as about two-thirds of the shaft-associated actin patches seem to be part of excitatory shaft synapses as shown in (Bommel *et al*, 2019), their turnover rates might also differ based on synaptic activity, although this still needs to be confirmed in future experiments.

In contrast to the axon, dendritic actin patches are independent of endosomes

Previously, so-called "actin hotspots", local enrichments in F-actin, have been described in the axon (Ganguly et al. 2015). In this case, the F-actin is nucleated on stationary endosomes. To show this, the authors used Brefeldin A, a drug that blocks ER-to-Golgi vesicle transport, and thus impairs the cell's secretory transport system and reduces the number of endosomal vesicles (Chardin & McCormick, 1999). When they disrupted the endosomes by brefeldin A treatment (100 ng/ml), the occurrence of axonal actin hotspots was significantly reduced (Ganguly *et al*, 2015). To test whether this was also true for dendritic actin patches, I reproduced the brefeldin A treatment, and found that it had no

noticeable effect on the size and localization of dendritic actin patches, suggesting an endosome-independent nature of these structures (Figure 10).

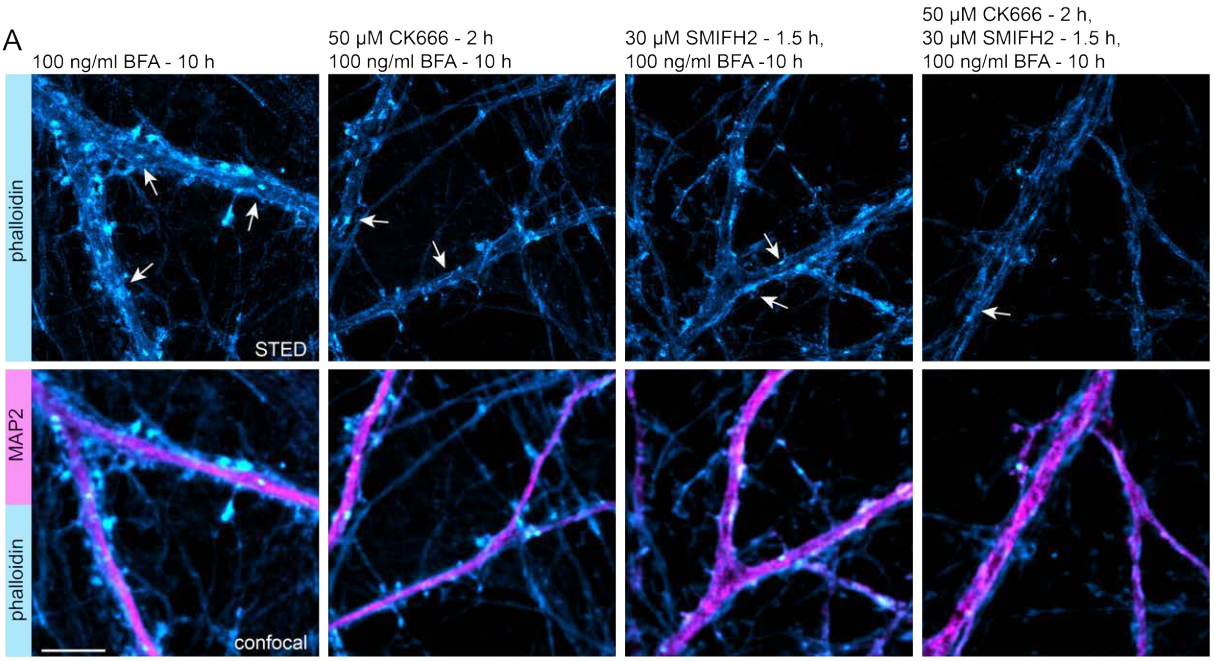

Figure 10. Disruption of the endolysosomal system with Brefeldin A has no effect on actin patches
(A) Representative STED and confocal images of DIV18 primary hippocampal neurons treated with Brefeldin A (BFA, 100 ng/ml for 10 h), a drug that disrupts endosomes. Neurons were stained with anti-MAP2 antibody and phalloidin-Atto647N, arrows indicate examples of actin patches. BFA treatment did not affect the number of actin patches, nor alter the effect of CK-666 (Arp2/3 inhibitor) and SMIFH2 (formin inhibitor) on actin patches. Scale bar: 5 µm.

Lysosomes as a model for processive dendritic vesicular cargo

Since actin patches seem to take up quite some space inside the dendritic shaft, we hypothesized that they affect MT-based organelle and vesicular trafficking, as it was previously shown that in the axons of *C. elegans* neurons, actin-rich regions can cause cargo-crowding and local traffic jams (Sood *et al*, 2018). To evaluate the effect of dendritic actin patches on vesicle trafficking, we chose to look at lysosomes as a representative vesicular organelle. Lysosomes are acidic, degradative organelles that show very active trafficking along dendrites. In recent years, more and more studies have highlighted their significance in neuronal function (Cheng *et al*, 2018; Goo *et al*, 2017; Padamsey *et al*, 2017). Furthermore, lysosomes (or lysosome-like organelles) can be easily visualized using the LysoTracker dye, which selectively labels acidic organelles, or by overexpressing a tagged version of the lysosome-marker protein LAMP1 (lysosome-associated protein 1).

It is important to note that LysoTracker and LAMP1 label slightly different subsets of organelles, and both are not exclusive to bona fide lysosomes. LysoTracker consists of a weakly basic amine group, which mediates the selective enrichment in acidic cellular compartments, coupled to a fluorescent dye. However, since lysosomes are not the only acidic organelles, the dye will also label late endosomes, phagosomes and autophagosomes. LAMP1 is a transmembrane protein which is targeted to lysosomes, however, due to membrane exchange between lysosomes and other organelles, LAMP1 is in dynamic equilibrium with endosomes and the plasma membrane, and has also been detected in the trans-Golgi network (Cheng *et al*, 2018). Further, mature lysosomes are canonically defined to contain

active degradative enzymes, such as the hydrolases cathepsin D and cathepsin B. However, a recent study has shown that only about one third of dendritic LAMP1-labeled organelles in dorsal root ganglion (DRG) neurons of the mouse spinal cord fulfill these criteria (Cheng *et al*, 2018). Still, since the focus of this study is not on the exact identity of the observed organelles, but rather on the observation of their trafficking behavior in relation to actin patches, for the sake of readability I will collectively refer to LAMP1- and LysoTracker-positive organelles as "lysosomes" from here on.

The presence of actin patches induces frequent pauses in lysosome transport behavior

To analyze lysosome trafficking behavior, we tested several freely available tracking programs for automated analysis (TrackMate (Tinevez *et al*, 2017), Particle Tracker (Sbalzarini & Koumoutsakos, 2005), KymoAnalyzer (Neumann *et al*, 2017), HybTrack (Lee & Park, 2018), KymographDirect (Mangeol *et al*, 2016), among others), however we found none of them satisfactory. We finally decided to evaluate lysosome movement by a semi-manual method using the open-source image processing software Fiji (NIH), as this gave us the most detailed information. As a first step, I compared lysosome motility in dendrites before and after treatment with LatA, to assess whether the absence of F-actin would have an effect on lysosome trafficking. Figure 11 shows an example of how this manual analysis was carried out. Labelled lysosomes in dendrites of DIV17-18 hippocampal neurons were imaged over the course of three minutes, a selected dendrite was manually traced and kymographs were constructed using the KymographClear plugin (Mangeol *et al*, 2016). The kymograph was automatically divided into retrograde, anterograde and non-moving events. The individual trajectories were then traced by hand. Trajectories with a uniform speed (= slope) were considered one "event", changes in speed (= slope) or stopping events (= vertical lines) were traced as separate events. Slope and length of each event were then used to calculate instant velocity, instant run length, and pausing time.

Using such kymograph analyses on LysoTracker labelled lysosomes, I found that depolymerization of actin filaments with LatA clearly increased the mobile fraction of lysosomes as judged by various parameters: total time spent in a mobile state increased (Figure 12A-B), summed pausing time was reduced (Figure 12C) and pausing times were generally shorter (Figure 12D). Interestingly, directional net flux analysis indicated that LatA treatment had an effect on the directionality of trafficking (Figure 12E), while instant velocity and instant run length did not change (Figure 12F, G). However, a shortcoming of LysoTracker is that it indiscriminately stains all cells in the cell culture, including all neurons, glia and other cells, which creates a high background. Additionally, after about 45 min to 1 h of incubation with LysoTracker, many neurons began to die. I therefore switched to the expressed, fluorescent lysosome marker LAMP1-eGFP and repeated the same experiments. Similarly, I found that LAMP1-eGFP vesicles became more mobile following actin depolymerization (Figure 13A-B), although the distribution of individual pausing times did not change (Figure 13D). The directional net flux was again strongly biased towards anterograde trafficking (Figure 13E). Run length as well as instant velocity were not affected (Figure 13F, G). Overall, LAMP1-labelled vesicles were slightly more mobile than LysoTracker-labelled ones, which might be due to the different spectrum of endolysosomal compartments labeled by LAMP1 (Cheng et al, 2018). Altogether, these data suggest a contribution of the dendritic F-actin cytoskeleton in directing trafficking of lysosomes. The finding that lysosomes show a bias towards anterograde trafficking, which is diminished upon LatA treatment, is very interesting. We hypothesize that this could be due to differential effects of the F-actin mesh on cargoes powered by different types of MT motors, i.e. different types of kinesins, or a difference between kinesins and dynein.

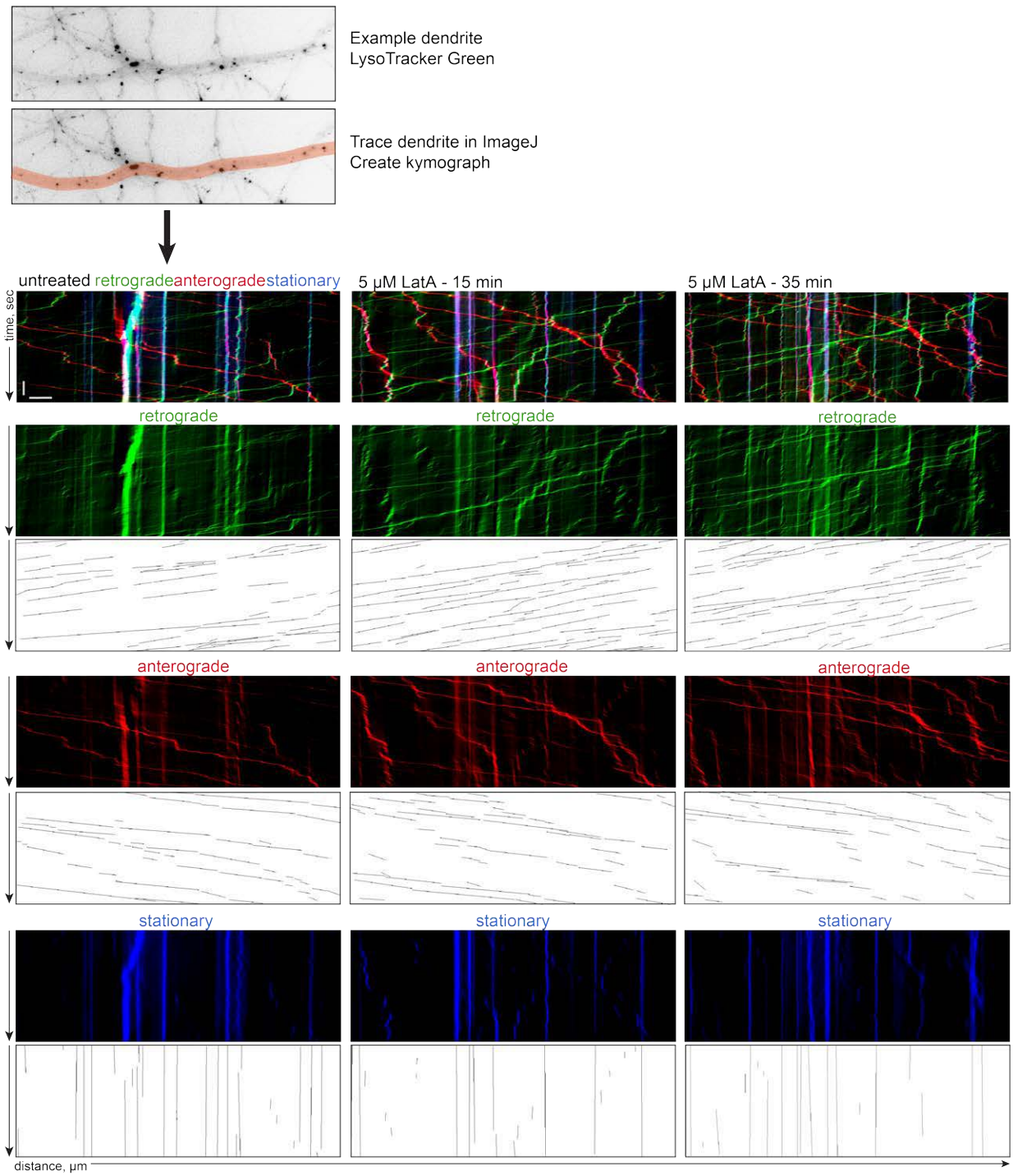

Figure 11. Workflow of kymograph analysis and quantification of additional lysosomal trafficking parameters.

(A) Representative kymographs from a DIV18 hippocampal neuron with LysoTracker Green before (control) and after 15 min or 35 min of 5 µM LatA treatment. Anterograde, retrograde, and stationary kymographs generated using the KymoGraphClear plugin for Fiji were traced manually. Scale bar: 5 µm.

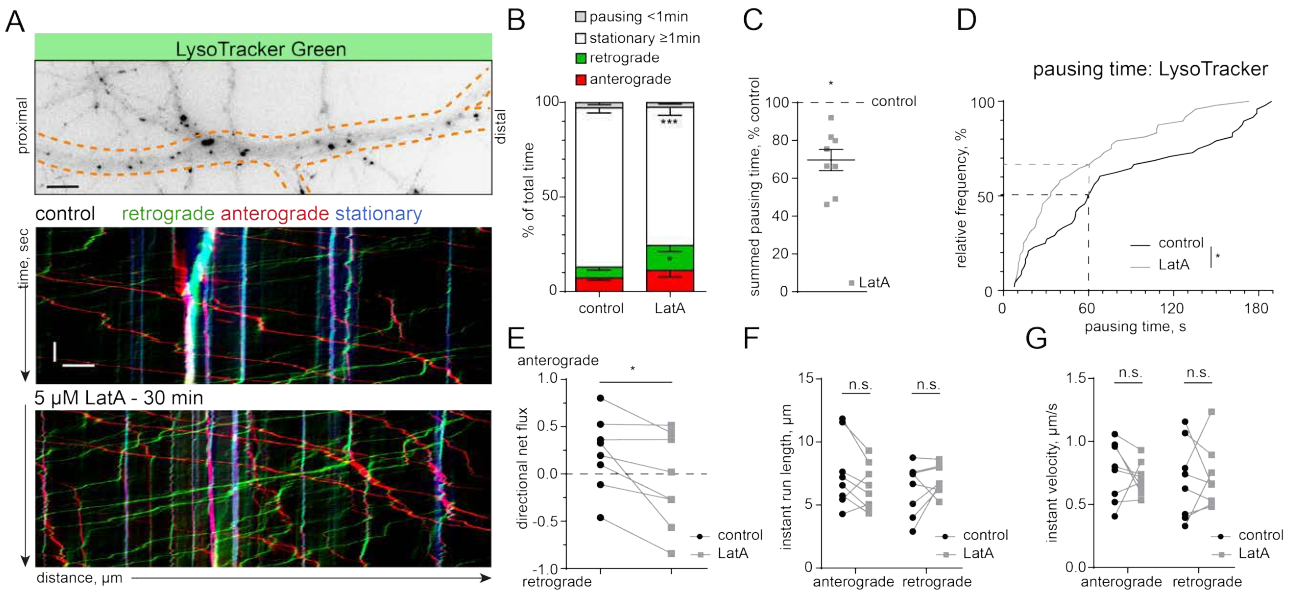

Figure 12. Latrunculin A treatment leads to an increased mobility of lysosomes labelled with LysoTracker

(A) Representative image and kymographs of a time lapse series from a dendritic segment of a DIV17 hippocampal neuron labelled with the cell-permeable lysosomal marker LysoTracker Green, before (control) and after treatment with LatA (5 µM). Scale bars: 5 µm, 10 sec.

(B) Quantification of lysosome motility from kymographs as shown in (**A**). Analyzed were the total time spent pausing (< 1 min), stationary (≥ 1 min), or moving in the anterograde or retrograde direction. LatA treatment (5 µM) increased the mobile retrograde fraction and decreased the stationary fraction. RM-2-ANOVA with behavior of lysosomes and treatment as within group factors. $F(3, 21)=9.2168$, $p=0.0004$, Newman Keuls post hoc test: * $p=0.049$, *** $p=0.00056$. *n= 8 dendritic segments of 6 cells in 3 independent cultures.*

(C) Summed total pausing time of lysosomes (LysoTracker) in LatA treated neurons, relative to the before-treatment control. LatA treatment (5 µM) decreased pausing times of lysosomes. 1-sample t-test against 100 %. * $p=0.01$. *Same n as in (B)*

(D) Cumulative frequency of the duration of pausing events. LatA treatment (5 µM) led to a shift towards shorter pausing times. 2-tailed Mann-Whitney U-test. * $p=0.015$. *n=48 (pausing events) in 8 dendritic segments of 6 cells in 3 independent cultures.*

(E) Analysis of the directional net flux of lysosomes (LysoTracker). LatA treatment (5 µM) abolished the bias towards anterograde flux. 2-tailed paired Student's t-test. * $p=0.02$. *Same n as in (B)*

(F, G) Analysis of the instant velocity and the instant run lengths of lysosomes (LysoTracker) moving in the anterograde or retrograde direction. LatA treatment (5 µM) did not significantly affect either of these parameters. 2-tailed paired Student's t-test. *Same n as in (B)*

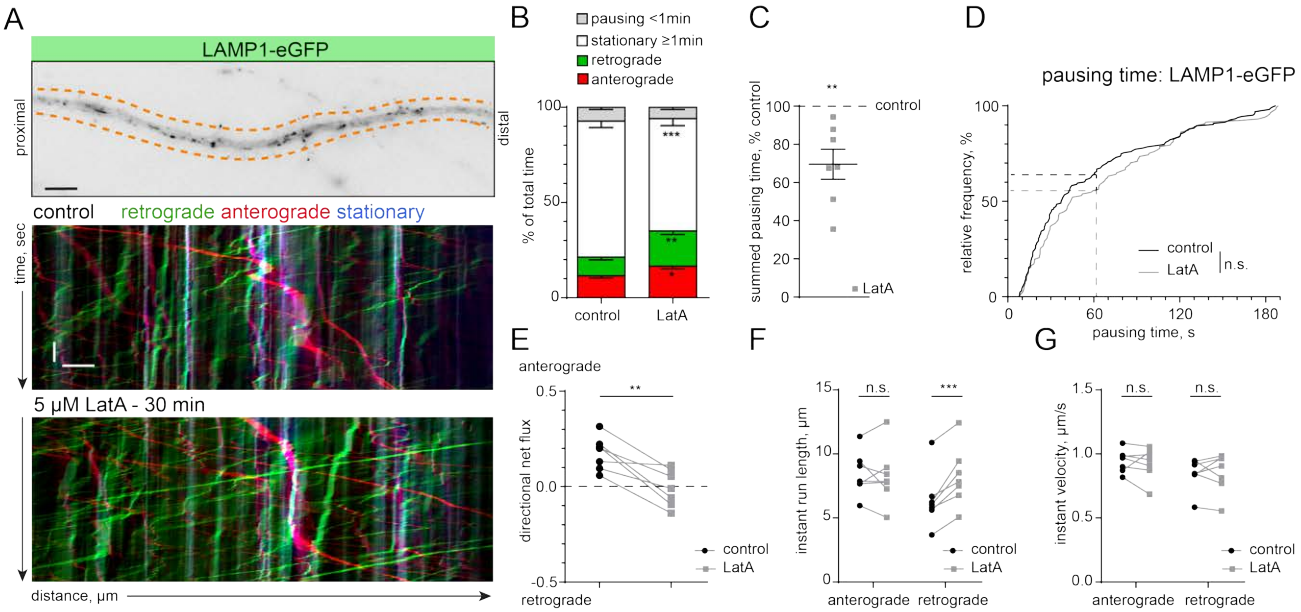

Figure 13. Latrunculin A treatment leads to an increased mobility of lysosomes labelled with GFP-LAMP1
(A) Representative image and kymographs of a time lapse series from a dendritic segment of a DIV16 hippocampal neuron transfected with LAMP1-eGFP, before (control) and after treatment with LatA (5 µM). Scale bars: 5 µm, 10 s.
(B) Quantification of lysosome motility from kymographs as shown in (**H**). Analyzed were the total time spent pausing (< 1 min), stationary (≥ 1 min), or moving in the anterograde or retrograde direction. LatA treatment (5 µM) increased the mobile retrograde and anterograde fractions and decreased the stationary fraction. RM-2-ANOVA with behavior of lysosomes and treatment as within group factors. $F(3, 18)=16.912$, $p=0.00002$. Newman Keuls post hoc test: * p=0.04, ** p=0.005, *** p=0.0002. *n= 7 dendritic segments of 7 cells in 2 independent cultures.*
(C) Summed total pausing time of lysosomes (LAMP1) in LatA treated neurons, relative to the before-treatment control. LatA treatment (5 µM) decreased pausing time of lysosomes. 1-sample t-test against 100 %. p=0.008. *Same n as in B.*
(D) Cumulative frequency of the duration of pausing events. LatA treatment (5 µM) did not significantly change the distribution of pausing events compared to control. 2-tailed Mann-Whitney U-test. *n=163 (ctr), n=117 (Lat(A) pausing events in 7 dendritic segments of 7 cells in 2 independent cultures.*
(E) Analysis of the directional net flux of lysosomes (LAMP1). Similar to the LysoTracker Green experiments (Fig. 13C), LatA treatment (5 µM) abolished the bias towards anterograde flux. 2-tailed paired Student's t-test. ** p=0.003. *Same n as in B.*
(F, G) Analysis of the instant velocity and the instant run lengths of lysosomes (LAMP1). LatA treatment (5 µM) increased the average instant run length in the retrograde direction. 2-tailed paired Student's t-test. *** p=0.001. *Same n as in B.*

Actin patches can act as physical barriers for kinesin-driven cargo

We next wanted to directly observe F-actin together with lysosomes in living cells. There are several methods to label F-actin, the most widespread one being the overexpression of LifeAct-GFP, a small peptide which specifically binds to actin filaments, but not monomeric actin. However, in our hands, neuronal and spine morphology was changed when we expressed this marker, and in the meantime, another study has confirmed that LifeAct affects actin structure and dynamics (Flores *et al*, 2019). We therefore decided to use a fluorescently tagged, expressed nanobody (a single-domain antibody fragment) against F-actin to specifically label actin filaments in neurons (from now on referred to as "chromobody"). My colleague co-transfected LAMP1-eGFP and chromobody-tagRFP to simultaneously visualize lysosomes and F-actin. Time lapse imaging followed by kymograph analysis revealed that

lysosomes frequently stop, reverse or anchor at F-actin-rich structures located within the dendrite, and that lysosome movement in the proximity of F-actin patches is generally slowed down (*shown in* Bommel *et al*, 2019). This suggests that dense meshes of F-actin could create intracellular traps for organelles and either passively slow down MT-based trafficking or interrupt processive transport via active F-actin anchoring mechanisms.

Lysosomes are associated with different types of MT motors (kinesin-1, -2, and dynein) (Farías *et al*, 2017; Pu *et al*, 2016), which makes it difficult to discriminate which motor might be primarily affected by the F-actin mesh, or if the presence of actin patches triggers competition between these motor proteins, a so called "tug-of-war", resulting in stops and switches in transport directionality (Hancock, 2014). In order to be able to rule out tug-of-war effects, I decided to engineer a cargo that is only transported by one type of dendritic MT motors. We chose to use the plus-end directed motor KIF17 (kinesin-2), which is known to be involved in trafficking of dendritic secretory organelles and should therefore provide similar trafficking kinetics and pulling forces as for physiological cargo (Hanus *et al*, 2014). As a cargo we chose peroxisomes, small and relatively stationary organelles that are mostly present in the soma (Kapitein *et al*, 2010). Although it has never been reported that neuronal peroxisomes are associated with any kind of motor-protein, or undergo active transport, I decided to test whether I could find myosin V or myosin VI associated with peroxisomes, as this might obviously impact their susceptibility to be stalled at actin patches. To this end I enriched peroxisomes from rat brain lysate using a differential centrifugation protocol as shown in Figure 14A. In the final ultra-centrifugation step (3), small vesicular compartments and organelles (including peroxisomes) were pelleted and either fixed for immunostaining and microscopy imaging, or subjected to SDS-PAGE and western blot. I used two well-established peroxisome markers, PEX14 and PMP70 (peroxisomal membrane proteins) to verify the enrichment of peroxisomes (Figure 14B, C), and found that neither myosin V nor myosin VI co-localized with the peroxisome signal (Figure 14B) or were enriched in the same fraction (Figure 14C). I therefore concluded that neuronal peroxisomes do not associate with myosin V or myosin VI to a significant degree.

I then designed an expression construct that contained the peroxisomal targeting sequence of PEX3 (peroxisomal membrane protein) C-terminally fused to GFP. This fusion protein on its own would only label the surface on peroxisomes with GFP. Into the same plasmid, I inserted the motor fragment of KIF17, which is constitutively active without its regulatory C-terminal domain, fused to a nanobody directed against GFP (VHH-GFP, Figure 15A). I separated the two fusion proteins by a so-called P2A-site, a short sequence that leads to the separation of the two proteins, even though they lie in the same open reading frame (Liu *et al*, 2017). The P2A peptide is often referred to as "self-cleaving", even though the mechanism is more likely based on a ribosome-skipping effect during translation, rather than a proteolytic "cleavage" of the final translation product (Donnelly *et al*, 2001). With this I circumvented the necessity to co-transfect two separate plasmids, and also ensured that the expression levels of both proteins would be more comparable (Figure 15A). Live imaging of hippocampal neurons transfected with this construct revealed that a part of the cellular peroxisomes became mobile. The organelles were transported unidirectionally in axons and bidirectionally in dendrites, indicating that there is no additional minus-end directed motor (i.e. dynein) attached, and there will indeed be no contribution of a "tug of war" to stalling and reversals of peroxisomes (Figure 15B). Instant velocity and instant run length were the same in anterograde and retrograde directions, confirming the model of a single type of MT motor (Figure 15C).

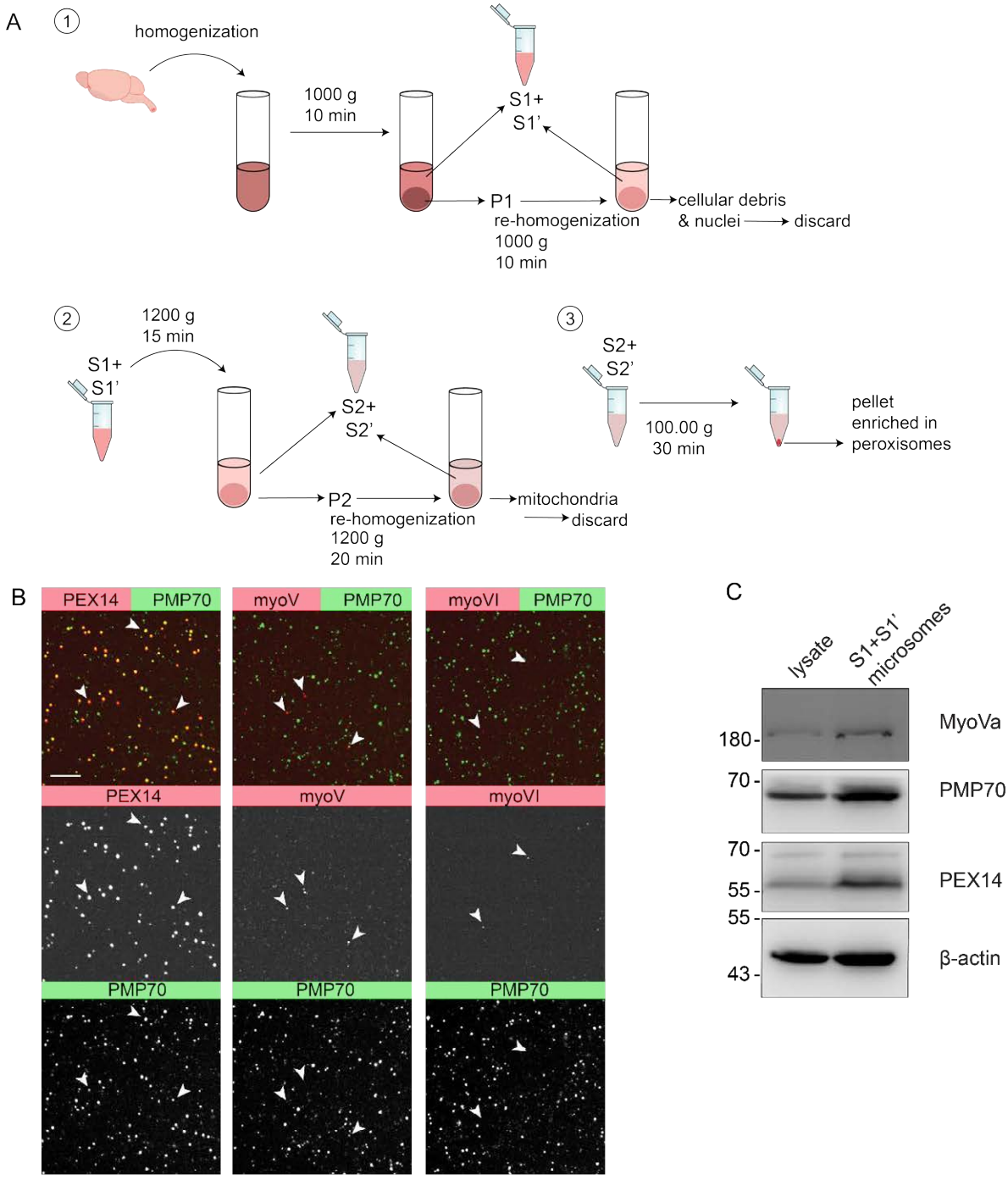

Figure 14. Neuronal peroxisomes are not enriched in myosin V or myosin VI

(A) Enrichment of peroxisomes from whole rat brain. (1) Whole rat brain was homogenized, centrifuged at 1000 g to remove cell debris and nuclei, the pellet P1 was re-homogenized and the centrifugation step was repeated. (2) Supernatants S1 and S1' were combined, centrifuged at 12.000 g to remove mitochondria and large membranous organelles, the pellet P2 was re-homogenized and the centrifugation step was repeated. (3) Supernatants S2 and S2' were combined and ultra-centrifuged at 100.000 g for 30 min to obtain the final fraction. The pellet was resuspended and used for western blot and ICC.

(B) Western blot of cleared cortical lysate (input) and enriched microsome fraction stained with antibodies against myosin Va (myoVa), PMP70, PEX14 and β-actin shows enrichment of peroxisomal markers PMP70 and PEX14, and the presence of myosin V (myoVa) in the fraction.

(C) Immuno-staining of peroxisomes enriched from rat brain, identified with the peroxisome markers PEX14 and PMP70, are negative for myosin V (myoV) and myosin VI (myoVI). Scale bar: 5 µm.

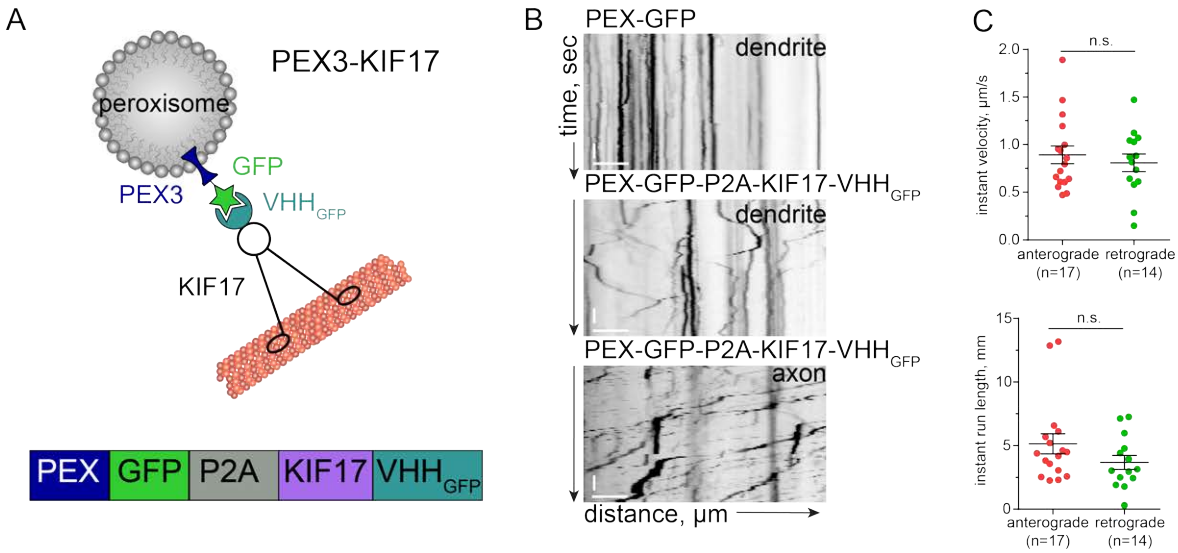

Figure 15. Characterization of PEX-GFP-KIF17 construct
(A) Schematic of a peroxisome coupled to constitutively active KIF17-VHH$_{GFP}$ via PEX3-GFP. Both constructs are expressed on the same bicistronic P2A vector to ensure co-expression. **(B)** Representative kymographs from a time-lapse series of a DIV16 hippocampal neuron expressing PEX3-GFP (control; no motility) or PEX3-GFP-P2A-KIF17-VHH$_{GFP}$. Bidirectional movement in dendrite and unidirectional movement (anterograde) in axon indicate the presence of KIF17 as the only processive microtubule-dependent motor. Scale bar: 2 µm, 10 s.

When co-expressing this construct with an actin-chromobody, we observed that mobile peroxisomes also frequently paused at F-actin patches as evident from the kymograph, as shown in (Bommel *et al*, 2019). I proceeded to analyze the motility of KIF17-coupled peroxisomes in the same way as I did for lysosomes (Figure 12), with the difference that I did not count peroxisomes that were stationary during the whole imaging period, as we could not distinguish between "stalled" peroxisomes, and those that might not have any KIF17 coupled to them. I induced actin depolymerization with LatA and compared various trafficking parameters as I did for lysosomes (Figure 16A-F).

LatA treatment resulted in a decrease of the summed pausing time (72 % from control / Figure 16B), while the frequency distribution of the pause durations did not significantly differ from the distribution before the treatment (Figure 16D). This means that after LatA treatment, peroxisomes took fewer pauses, but the pause duration of stopped peroxisomes was unaltered. This could mean that actin patches are involved in triggering pauses, but not in long-term halting of this artificial cargo. These results suggest that, similar to lysosomes, kinesin-transported peroxisomes can interact with the actin cytoskeleton. The observation that both lysosomes and KIF17-driven peroxisomes stall at actin patches excludes the possibility for a "tug of war" as a pausing mechanism. The remaining options are "passive" stalling due to physical hindrance, or "active" stalling due to activation of associated actin-binding proteins such as myosin motors. As we found no evidence for neuronal peroxisomes associating with the processive myosins V and VI, and, in contrast to lysosomes, LatA treatment did not affect pause duration of peroxisomes, we decided to investigate whether these myosins might be the responsible factor to induce active stalling of lysosomes in dendrites.

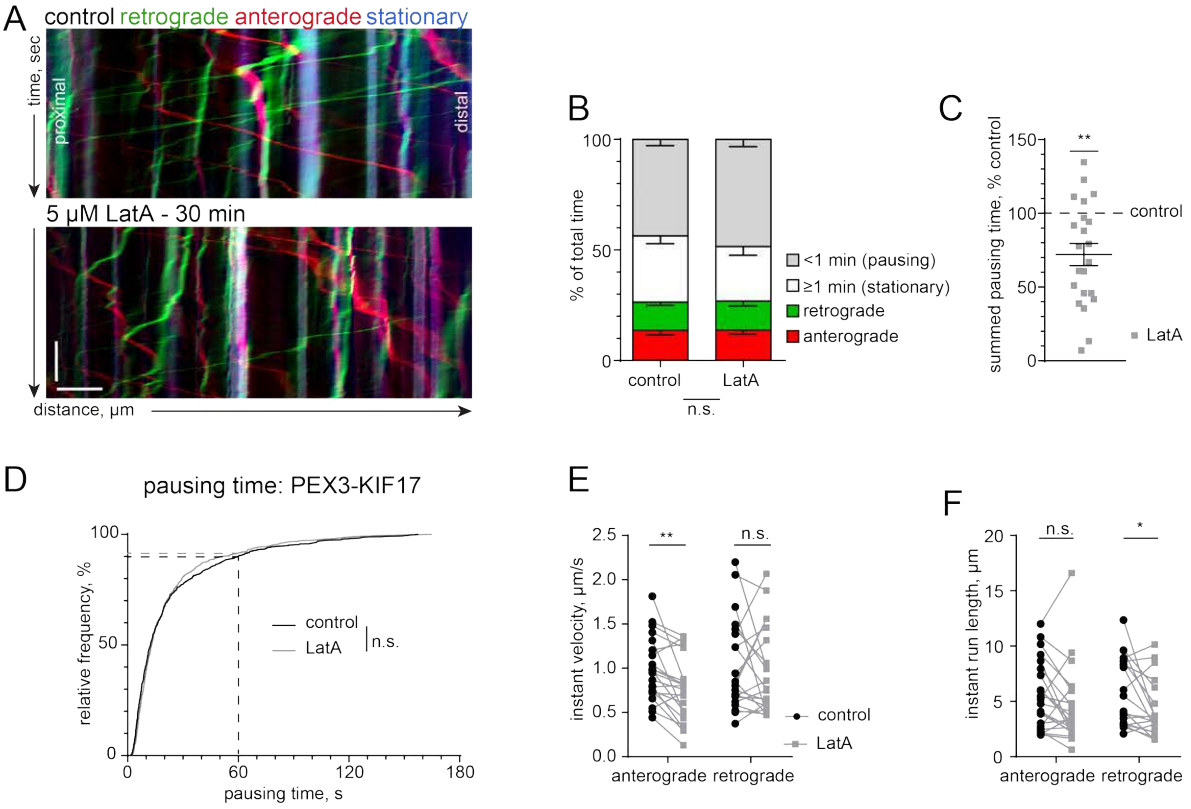

Figure 16. Peroxisomes are hindered by actin patches, but only for short time spans
(A) Representative kymograph from a DIV16 hippocampal neuron expressing PEX-GFP-KIF17 before and after LatA treatment (5 µM). Scale bar: 5 µm, 15 s.
(B) Quantification of KIF17-coupled peroxisome motility from kymographs. Analyzed were the total time spent pausing (< 1 min), stationary (≥ 1 min), or moving in the anterograde or retrograde direction. LatA treatment (5 µM) did not significantly affect motility. RM-2-ANOVA with PEX behavior and treatment as within group factors. F(3, 63)=1.9052, p=0.138. *n=22 dendritic segments of 15 cells in 3 independent cultures.*
(C) Cumulative frequency of the duration of pausing events of KIF17-coupled peroxisomes before (control) and after LatA treatment (5 µM). LatA treatment did not have a significant effect on the distribution of pausing events. 2-tailed Mann-Whitney U-test. *n=695 (control), n= 579 (Lat(A) pausing events in 22 dendritic segments of 15 cells in 3 independent cultures.*
(D) Summed total pausing time of KIF17-coupled peroxisomes in LatA (5 µM) treated neurons, relative to the before-treatment control. LatA treatment significantly reduced the cumulative pausing time. 1-sample t-test against 100 %. ** p=0.0013. *Same n as in (F)*
(E, F) Analysis of the instant velocity and the instant run lengths of KIF17-coupled peroxisomes. LatA treatment (5 µM) decreased the average instant velocity in the anterograde direction and reduced the instant run length in the reterograde direction. I) 2-tailed paired Student's t-test. ** p=0.0012 (I) and 2-tailed Wilcoxon matched pairs test. * p=0.01 (J). *n=22 (anterograde), n=21 (retrograde) dendritic segments of 15 cells in 3 independent cultures.*

Lysosomes are associated with myosins V and VI

Lysosomes can be found inside the head of dendritic spines (Goo *et al*, 2017). Although it is possible that they are deposited there by transiently entering MTs and associated MT motors, it is likely that they are transported into the spine head by processive myosin motors. We hypothesized that the difference we observed in the stalling behavior of lysosomes vs. KIF17-coupled peroxisomes is due to an active anchoring of lysosomes to actin via myosin motors, which are not present on peroxisomes.

To test whether myosin V or myosin VI are present on lysosomes, I enriched lysosomes from rat cortex and hippocampus using the Lysosome Enrichment Kit for Tissues and Cultured Cells (Thermo Fisher), and verified the enrichment by staining with LysoTracker, and immuno-staining with a LAMP1 antibody (Figure 17A). Further immunostaining for the processive myosins Va and VI labeled the same structures as LAMP1 (Figure 17B). Additionally, western blotting of the lysosome-enriched fraction showed the presence of known lysosome-associated MT motor proteins (KIF5C and dynein IC1/2) (Caviston *et al*, 2011; Farías *et al*, 2017) as well as myosin Va and myosin VI (Figure 17C). These results support the hypothesis that, in addition to actin patches posing as passive, physical barriers, myosins could take over kinesin- or dynein-driven lysosomes and actively stall them once they encounter F-actin-rich environments.

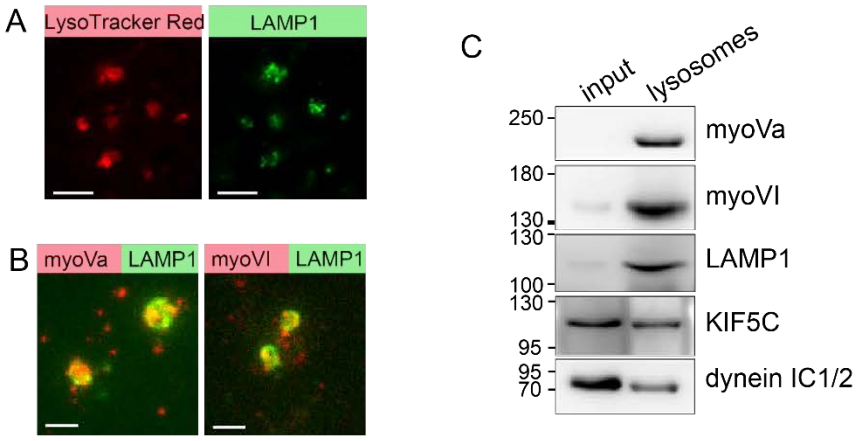

Figure 17. Processive myosins associate with lysosomes
(A, B) Representative fluorescence microscopy images of lysosomes enriched from adult rat cortex and stained with LysoTracker Red and α-LAMP1 antibody (A, scale bar: 5 µm), and α-LAMP1 and α-myosin Va / myosin VI antibody (B, Scale bar: 2 µm).
(C) Western blot of cleared cortical lysate (input) and enriched lysosome fraction stained with antibodies against myosin Va (myoVa), myosin VI (myoVI), LAMP1, KIF5C and dynein IC 1/2 shows the presence of different motor proteins in the lysosome fraction.

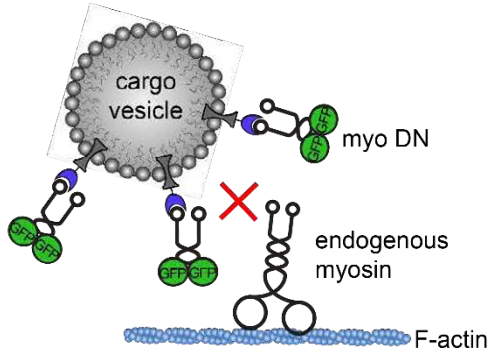

Figure 18. Principle of dominant negative inhibition.
Overexpression of the myosin cargo binding domain leads to the occupation of endogenous binding sites with a non-functional motor, which out-competes the endogenous motor and thereby impairs its function.

Specific inhibition of myosin V, but not myosin VI, affects lysosomal trafficking

To test the contribution of myosins to lysosome stalling more directly, we employed a dominant negative approach to inhibit myosin V and VI. Dominant negative inhibition happens via overexpression of the cargo binding domain of myosin Va (myoV DN) or myosin VI (myoVI DN), which impairs the function of the endogenous myosins by competition (Figure 18) (Osterweil *et al*, 2005; Wu *et al*, 2002).

Kymograph analysis of lysosomal motility in myoVI DN expressing neurons showed only a minimal change in pausing time distribution (Figure 19D), while all other analyzed parameters were unaffected (Figure 19A-D). I subsequently employed a pharmacological myosin VI inhibitor, 2,4,6-triiodophenol (TIP) (Heissler *et al*, 2012) to test whether interference with myosin VI activity can affect pausing of lysosomes. TIP specifically inhibits the actin-activated ATPase activity of myosin VI, but unfortunately the exact mechanism of action is unknown – i.e. whether myosin VI bound by TIP stays attached to actin, thus becoming a tether, or whether it dissociates from actin. I found that TIP treatment slightly increased the fraction of long pauses (> 1 min) and reduced instant velocities and the run length (Figure 19G, J). The pausing behavior, analyzed by summed pausing time as well as relative frequency distribution, was not changed (Figure 19E, F, H, I). I therefore conclude that overall myosin VI contribution to lysosome stalling is negligible. The slightly increased pausing and decreased run length and speed could be explained by TIP turning myosin VI into a tether. In this case, myosin VI could be acting as a brake, though not strongly enough to cause a complete stop of the vesicle. Although, without clear information on the mechanism of TIP inhibition, this remains purely speculative.

Kymograph analysis of LAMP1-mCherry-labelled lysosomes showed that upon overexpression of myoV DN, lysosome motility increased, as judged by the decrease in time spent being stationary (Figure 20C), and pausing time distribution shifted to shorter pauses (Figure 20D). The total number of mobile and stationary lysosomes, as well as instant velocity and instant run length, were not affected (Figure 20B). Notably, live imaging experiments of DIV16-17 neurons overexpressing mCerulean-labelled myoV DN showed visible associations between the myoV DN tail and LAMP1-positive vesicles, again suggesting that lysosomes associate with myosin V motors in living cells (Figure 20E).

In a complementary set of experiments, I used a pharmacological inhibitor of myosin V, MyoVin, which partially inhibits the actin-activated ATPase activity of myosin V, turning it from a motor into a tether (Gramlich & Klyachko, 2017; Heissler *et al*, 2017). 30 min of MyoVin treatment (30 µM) increased the number of stationary lysosomes, the total time of long pausing events (>1 min) and the summed pausing time (Figure 21A-E), while the total time of short pauses (<1 min) and instant velocity decreased (Figure 21C, F). All in all, I interpret these effects as MyoVin treatment leading to an elongation of the pausing time of lysosomes that are already stalled by myosin V, by “freezing” the motor in an actin-bound state. Taken together, the results from MyoV DN and MyoVin suggest that myosin V can elongate, but not initiate the pausing time of lysosomes.

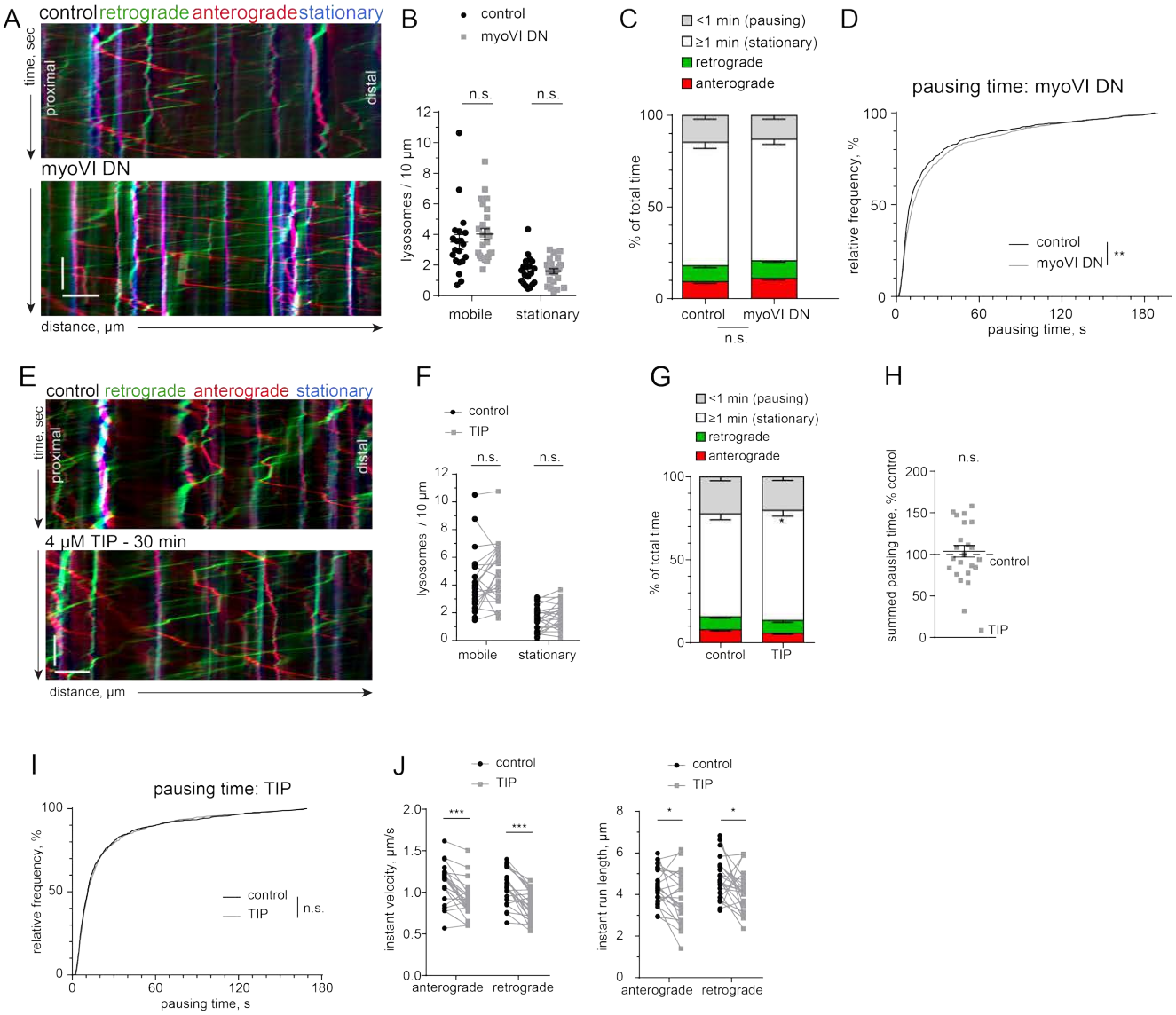

Figure 19. Effects of Myosin VI DN and pharmacological inhibitors on LAMP1-eGFP motility

(A) Representative kymographs from dendritic segments of DIV16/DIV17 primary hippocampal neurons expressing LAMP1-mCherry and either YFP (control) or a myoVI DN-GFP construct. Scale bar: 5 µm, 15 s.

(B) Quantification of mobile and stationary lysosomes. Overexpression of myoVI DN did not have a significant effect on lysosome count. 2-tailed Mann-Whitney U-test. *n=20 (ctr), n= 25 (DN) dendritic segments of 20 cells (control) and 23 cells (myoVI DN) in 2 independent cultures.*

(C) Quantification of lysosome motility from kymographs as shown in **I**. Analyzed were the total time spent pausing (< 1 min), stationary (≥ 1 min), or moving in the anterograde or retrograde direction. Overexpression of myoVI DN did not cause significant changes. RM-2-ANOVA with behavior of lysosomes as within group factor and myoVI DN as categorical factor. F(3, 129)=0.25, p=0.86. *Same n as in J.*

(D) Cumulative frequency of the duration of pausing events of lysosomes (LAMP1-mCherry) in control (YFP) and myoVI DN-GFP expressing neurons. Fully stationary events are excluded. Presence of myoVI DN led to a shift towards longer pausing events. 2-tailed Mann-Whitney U-test. ** p=0.009. *n=838 (control) in 20 dendritic segments of 20 cells, n=853 (MyoVI DN) pausing events in 25 dendritic segments of 23 cells in 2 independent cultures.*

(E) Representative kymographs from a dendritic segment of a DIV16 primary hippocampal neuron expressing LAMP1-eGFP, before (control) and after treatment with the myosin VI inhibitor TIP (4 µM, 30 min). Scale bar: 5 µm, 15 s.

Cont'd Fig. 19: (F) Quantification of mobile and stationary lysosomes (LAMP1-eGFP). TIP has no significant effect on lysosome numbers. Paired 2-tailed Student's t-test (stationary) or Wilcoxon matched pairs test. *n= 22 dendritic segments of 19 cells in 3 independent cultures.*
(G) Quantification of lysosome motility from kymographs as shown in **G**. Analyzed were the total time spent pausing (< 1 min), stationary (≥ 1 min), or moving in the anterograde or retrograde direction. Treatment with TIP slightly increased the long-term (≥ 1 min) stationary fraction. RM-2-ANOVA with lysosome behavior and treatment as within group factors. F(3, 63)=3.46, p=0.021 with Newman Keuls post hoc test. * p=0.01. *Same n as in H.*
(H) TIP treatment did not significantly change the summed pausing time of lysosomes (LAMP1-eGFP). 1-sample t-test against 100 %. *Same n as in H.*
(I) Cumulative frequency of the duration of pausing events of lysosomes (LAMP1-eGFP) in control (DMSO) and in the presence of TIP. Fully stationary lysosomes were excluded. TIP-treatment did not affect the distribution of pausing events. 2-tailed Mann-Whitney U-test. *n=1029 (control), n=908 (TIP) events of 22 dendritic segments of 19 cells in 3 independent cultures.*
(J) Analysis of the instant velocity (left) and the instant run lengths (right) of lysosomes (LAMP1-eGFP) moving in the anterograde or retrograde direction. TIP treatment decreased the instant velocity and run length in both directions. 2-tailed Wilcoxon matched pairs test (anterograde velocity) *** p=0.0003 or paired 2-tailed Student's t-test * p=0.03 (anterograde run length) p=0.04 (retrograde run length), *** p< 0.001 (retrograde velocity). *Same n as in F.*

The involvement of myosin V in active cargo stalling at actin patches has many interesting implications. For example, the Ca^{2+}/calmodulin dependency of myosin V activation could provide a mechanism for activity-dependent positioning of lysosomes (Goo *et al*, 2017; Wang *et al*, 2008). It is conceivable that only a subset of lysosomes will carry myosins, possibly depending on their maturation status, which we could not resolve in this study. It has also been shown that neuronal activity induces lysosomal exocytosis and thereby release of cathepsins (Padamsey *et al*, 2017). The spatially and temporally controlled cathepsin B release from mature lysosomes may be a critical step required for input-specific synaptic potentiation. The close proximity to NMDA receptors at shaft synapses would allow for direct Ca^{2+}-dependent synaptic control of lysosomal exocytosis. A dense actin mesh, surrounding the PSD of shaft synapses, or at the base of spines, could stall mature fusion-competent lysosomes for longer periods. Alternatively, long pausing events might promote endolysosomal maturation. How trafficking rules relate to lysosomal maturation needs to be addressed in future studies.

All in all, we found that a multitude of factors, both passive and active, are involved in lysosome positioning at actin patches. The effects of LatA on KIF17-coupled peroxisome transport suggest that the presence of a dense actin-mesh constitutes a passive, physical barrier for kinesin-mediated trafficking. In the presence of actin patches, peroxisomes, which are not associated with myosin V, take frequent but short pauses. Lysosomes, which are associated with myosin V, decrease their stalling time upon inhibition of myosin V, and increase it when myosin V is locked in the F-actin bound position. From this we conclude that actin patches act as a physical hindrance that indiscriminately causes cargo to stall. This short stop might be sufficient for other factors to initiate active anchoring and longer pauses. It appears that myosin V, but not myosin VI activity, allows lysosomes to stop over longer periods of time. However, neither of these myosins alone seems to be essential for the stalling of lysosomes in dendrites.

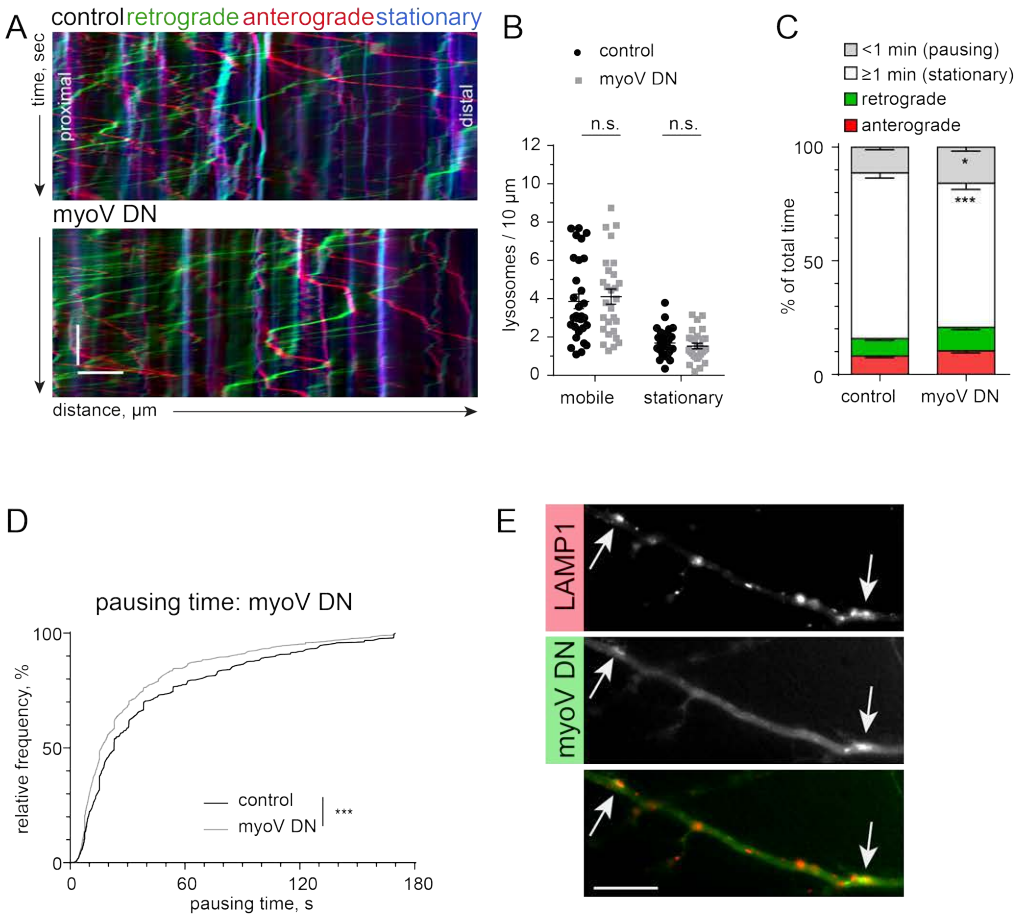

Figure 20. Myosin V DN affects motility of lysosomes in dendrites

(A) Representative kymographs from dendritic segments of DIV16 primary hippocampal neurons expressing LAMP1-mCherry and either mCerulean (control) or a myoV DN-mCerulean. Scale bar: 5 µm, 15 s.

(B) Quantification of mobile and stationary lysosomes. Overexpression of myoV DN did not significantly change lysosome count. Unpaired 2-tailed Student's t-test (mobile) or Mann-Whitney U-test (stationary). *n=30 (ctr), n= 28 (DN) analyzed dendritic segments from 21 cells in 3 independent cultures.*

(C) Quantification of lysosome motility from kymographs as shown in **(E)** Analyzed were the total time spent pausing (< 1 min), stationary (≥ 1 min), or moving in the anterograde or retrograde direction. Overexpression of myoV DN led to an increase in pausing events and decreased the number of stationary lysosomes. RM-2-ANOVA with behavior of lysosomes as within group factor and myoV DN as categorical factor. $F(3, 174)=6.1977$, $p=0.0005$ with Newman Keuls post hoc test: * $p<0.05$, *** $p=0.0003$. *Control: n=31 dendritic segments of 21 cells in 3 independent experiments. MyoV DN: n = 29 analyzed dendritic segments from 21 cells in 3 independent cultures.*

(D) Cumulative frequency of the duration of pausing events of lysosomes (LAMP1-mCherry) in control (mCerulean) and myoV DN-mCerulean expressing neurons. Fully stationary events are excluded. Presence of myoV DN led to a shift towards shorter pausing events. 2-tailed Mann-Whitney U-test. *** $p<0.001$. *n=836 (control) pausing events in 31 dendritic segments of 21 cells, n=973 (myoV DN) pausing events in 29 dendritic segments of 21 cells in 3 independent cultures.*

(E) Dendritic segment of a DIV16 primary neuron transfected with myoV DN-mCerulean and LAMP1-mCherry. Arrows indicate myoV DN enriched at LAMP1 vesicles. Scale bar: 10 µm.

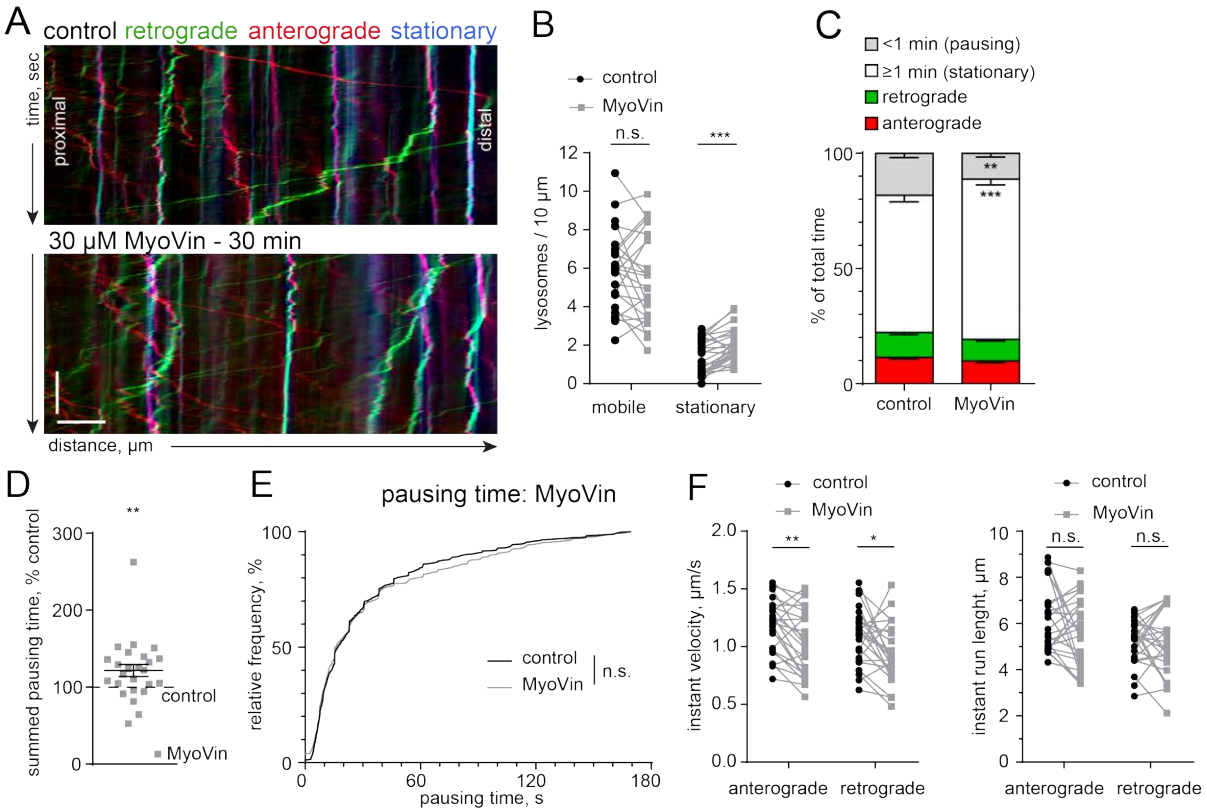

Figure 21. Effects of myosin V pharmacological inhibitors on LAMP1-eGFP motility

(A) Representative kymographs from dendritic segments of a DIV16 primary hippocampal neuron expressing LAMP1-eGFP, before (control) and after treatment with the myosin V inhibitor MyoVin (30 µM, 30 min). Scale bar: 5 µm, 15 s.

(B) Quantification of mobile and stationary lysosomes (LAMP1-eGFP). MyoVin treatment increased the number of stationary lysosomes, but did not significantly change the mobile fraction. 2-tailed paired Student's t-test. *** p<0.001. *n= 25 dendritic segments of 21 neurons in 3 independent cultures.*

(C) Quantification of lysosome motility from kymographs as shown in **(A)** Analyzed were the total time spent pausing (< 1 min), stationary (≥ 1 min), or moving in the anterograde or retrograde direction. MyoVin increased stationary time and reduced short-term pausing. RM-2-ANOVA with lysosome behavior and treatment as within group factors. F(3, 72)=14.623, p<0.001 with Newman-Keuls post hoc test ** p=0.001, *** p<0.001. *Same n as in B*

(D) MyoVin treatment increased the cumulative peroxisome pausing time. Wilcoxon signed rank test. ** p=0.005. *Same n as in (B)*

(E) Cumulative frequency of the duration of pausing events of lysosomes (LAMP1-eGFP) in control (DMSO) and the presence of MyoVin. Fully stationary lysosomes were excluded. The presence of MyoVin did not change the pausing time distribution. 2-tailed Mann-Whitney U-test. *n=782 (control), n=654 (MyoVin) events in 25 dendritic segments of 21 cells in 3 independent culture.*

(F) Analysis of the instant velocity (left) and instant run lengths (right) of lysosomes (LAMP1-eGFP) moving in the anterograde or retrograde direction. MyoVin treatment decreased instant velocities. Paired 2-tailed Student's t-test (mobile) or Wilcoxon matched paired (stationary) * p=0.012, ** p=0.0029. *Same n as in B.*

Chapter 2: Myosin V as a mediator of dendritic synaptopodin localization

The following work has been published in (Konietzny et al., 2019). Parts of the presented experimental work have been conducted with the help of Judit González-Gallego, Julia Bär and Edda Thies from the ZMNH (Hamburg), and with Jeroen Demmers and Dick Dekkers from the EMC mass spectrometry facility (Rotterdam).

Processive myosins are novel interactors of synaptopodin

The protein synaptopodin is an essential component of the SA, and is closely associated with the smooth ER-derived membranes that are forming this specialized organelle (Figure 8). Despite a growing number of studies addressing the role of the SA in neuronal function, it is still unclear what factors selectively localize synaptopodin or the SA to individual dendritic spines. In previous studies, long-term imaging experiments with overexpressed GFP-synaptopodin in primary hippocampal neurons revealed that synaptopodin clusters change their position within the dendrite or spine over large time spans (Vlachos *et al*, 2009). However, since these data were acquired with a one-day interval, it is difficult to judge whether synaptopodin clusters were actively relocated as a whole or whether synaptopodin becomes enriched *in situ* via a different mechanism. We aimed to characterize molecular dynamics, transport and synaptic targeting of synaptopodin in detail in order to answer these questions.

We first set out to obtain unbiased information about the brain-specific synaptopodin interactome (690 aa isoform, Figure 8D) using a mass spectrometry approach. To this end, we produced biotinylated GFP-synaptopodin (and biotinylated GFP as a control) in HEK293T cells and purified it by coupling it to Streptavidin beads. The bio-GFP-synaptopodin and bio-GFP coupled beads were then incubated with a rat brain extract. This allowed brain-specific interactors of synaptopodin to bind (Figure 22).

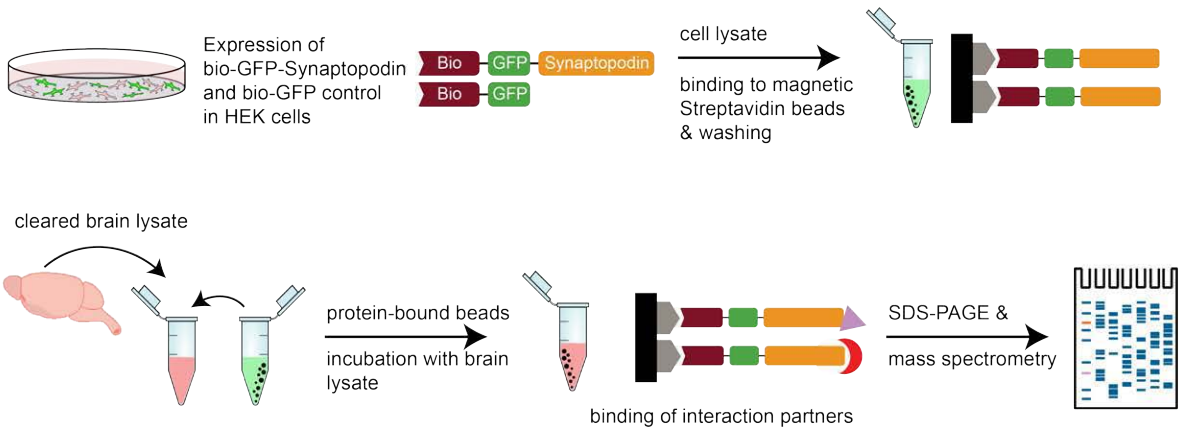

Figure 22. Preparation for mass-spectrometric analysis of synaptopodin interactors
Biotinylated GFP-tagged synaptopodin and biotinylated GFP (control) were expressed in separate batches of HEK293 cells. The HEK cells were lysed and the lysates incubated with magnetic streptavidin-coupled beads, which bind to biotin. The beads, which were now coupled to bio-GFP-synaptopodin or bio-GFP, were washed extensively before they were incubated with rat brain lysate, to capture brain-specific interactors of synaptopodin. After further washing steps to remove unspecific interactions, the captured proteins were released from the beads by boiling them at 95°C, and separated by SDS-PAGE for subsequent mass-spectrometric analysis.

All protein was then eluted from the beads by boiling and separated by SDS-PAGE (Figure 23A). In collaboration with the Erasmus Medical Center in Rotterdam, mass spectrometry was performed on the proteins extracted from the SDS-gel (bio-GFP vs. bio-GFP-synaptopodin), which resulted in a long list of potential synaptopodin interacting proteins, as listed in (Konietzny *et al*, 2019). We found several known interactors (including actinins, actin and 14-3-3), and many hits for potential novel interaction partners (Figure 23B). Interestingly, CamKIIα and CamKIIβ isoforms were also present in complex with synaptopodin, an interaction previously only known from renal podocytes (Faul *et al*, 2008). In this cell type, it was shown that synaptopodin can be phosphorylated by PKA and CaMKII. Together with the phosphatase calcineurin, these kinases regulate the phosphorylation status of synaptopodin and its association with the protein 14-3-3, which can protect synaptopodin from degradation (Faul *et al*, 2008)(Figure 8D). It is therefore plausible that mechanisms similar to those in podocytes regulate synaptopodin stability and degradation also in dendrites and dendritic spines. Since phosphorylation is required for 14-3-3 binding, we hypothesize that CaMKII will have a stabilizing effect on synaptopodin upon synaptic activation, which could be one way to enrich synaptopodin especially at active synapses.

Other potential synaptopodin interacting proteins included several actin stabilizing, capping, severing and modifying proteins including tropomodulins (Tmod2, Tmod3), gelsolin (Gsn), the Arp2/3 complex (Arpc2), coronins (Coro2a, Coro2b), and F-actin-capping proteins (Capza1, Capza2) (Figure 23B). This finding indicates that the association of synaptopodin and actin filaments might be more complex than simply direct binding to actin and can be subjected to regulation.

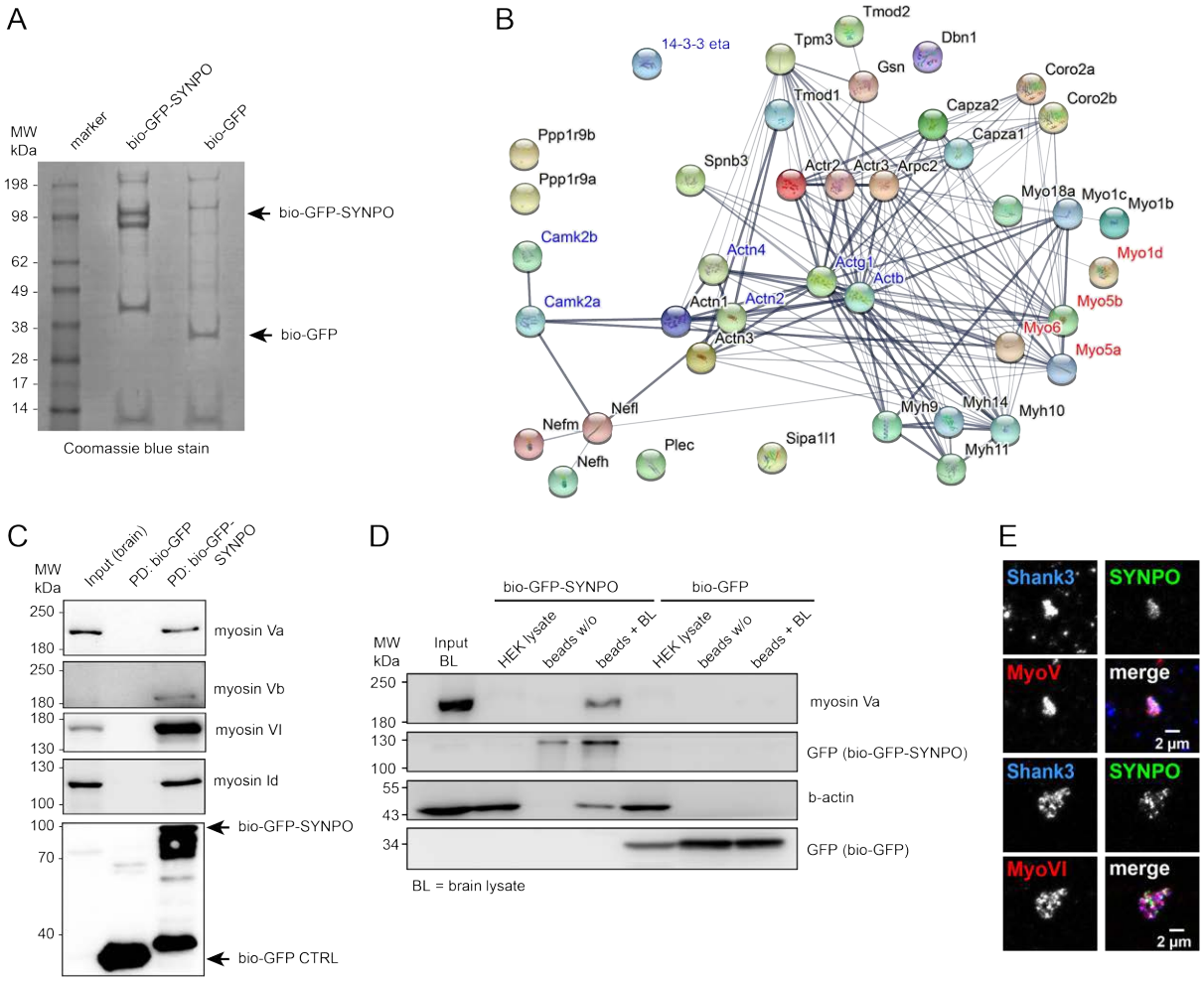

Figure 23. Myosin family proteins are novel interaction partners of synaptopodin
(A) SDS-polyacrylamide gel of the bio-GFP-synaptopodin (SYNPO) and bio-GFP (control) pull-down used for mass-spectrometric analysis. Biotinylated GFP-synaptopodin was expressed in HEK293 cells and bound to Streptavidin-beads. The beads were then incubated with rat brain lysate to pull down brain-specific interactors of synaptopodin.
(B) Network analysis of selected potential synaptopodin-interactors identified in the mass spectrometry analysis using the online STRING analysis tool. Highlighted in blue are known synaptopodin-interacting proteins including actin (Actg1, Actb) and actinins (Actn2, Actn4). In red are myosins that were later tested positively in the co-immunoprecipitation in (D). Line thickness indicates strength of data support.
(C) Western blot analysis of bio-GFP-synaptopodin pull-down from brain lysate confirms interaction with myosin Va, Vb, VI and Id. Input = brain lysate, Strept-HRP = streptavidin coupled to horse-radish peroxidase. Arrows indicate expected MW of bio-GFP-synaptopodin (upper) and bio-GFP (lower).
(D) Western blot analysis of bio-GFP-synaptopodin pull-down probed for the presence of actin before and after incubation with brain lysate. Bio-GFP-synaptopodin-coupled beads are not enriched with myosin Va or actin coming from the HEK293 cells, but show association with myosin Va and actin specifically from brain lysate. BL = brain lysate. Beads w/o = bio-GFP-synaptopodin-coupled beads before incubation in brain lysate. Beads + BL = bio-GFP-synaptopodin-coupled beads after incubation in brain lysate.
(E) Immunostaining of synaptosome-enriched fraction from rat brain. Synaptosomes were enriched from brain lysate using differential centrifugation and stained with antibodies against Shank3 (post-synaptic marker), synaptopodin and myosin V or VI. Both myosin V and VI could are found at synaptopodin- and Shank3-containing structures. Scale bar = 5 µm.

While we found no kinesin or dynein motor proteins or their adapters present in the synaptopodin complex, particularly unconventional myosins as putative prominent binding partners attracted our attention (Figure 23B). Processive myosin V and VI are highly expressed in pyramidal neurons and play an important role in a wide range of neuron-specific functions including organelle and mRNA transport and anchoring (Correia *et al*, 2008; Esteves da Silva *et al*, 2015). We hypothesized that the processive myosins V and VI could transport and anchor synaptopodin to dendritic spines, thereby mediating the synaptopodin-dependent formation of the spine apparatus.

To verify these putative interactions, we performed a pull-down assay from rat hippocampus, and analyzed individual interactors via western blot. This confirmed the association of bio-GFP-synaptopodin but not the bio-GFP control with the endogenous myosin Va, Vb, VI and Id (Figure 23C). Interestingly, we found that β-actin was present in the synaptopodin-myosin Va complex formed in rat brain lysate, but not in the extract from HEK293T cells (Figure 23D). Since all reactions were performed on ice and in the presence of detergents (0.1 % SDS, 0.2 % NP-40), the actin associated with the synaptopodin-beads in the brain lysate must be either G-actin or a brain-specific type of highly stabilized F-actin.

To further confirm the association of synaptopodin with processive myosins in the brain, we isolated a synaptosome-enriched fraction from rat cortex and hippocampus and immunostained it for endogenous synaptopodin, myosin Va, myosin VI and SHANK3 as a post-synaptic marker. Synaptosomes are isolated synaptic terminals that have been pinched off from the neuron during mild homogenization. They contain the presynaptic terminal and parts of the postsynaptic membrane. This assay indicated that synaptopodin-positive synaptosomes indeed contain myosins (Figure 23E). We therefore decided to investigate the role of these myosins in the synaptic targeting of synaptopodin.

Synaptopodin is upregulated during neuronal development

The expression of synaptopodin is developmentally regulated and coincides with synaptogenesis. This has been shown repeatedly in brain slices using antibody-staining against synaptopodin, as well as in-situ hybridization to detect synaptopodin mRNA (Mundel *et al*, 1997; Czarnecki *et al*, 2005). However, no comprehensive timeline has been established for dissociated cultures of primary neurons. We therefore decided to analyze the expression of synaptopodin systematically and to establish a time-line of synaptopodin expression in the model system we are using in this study.

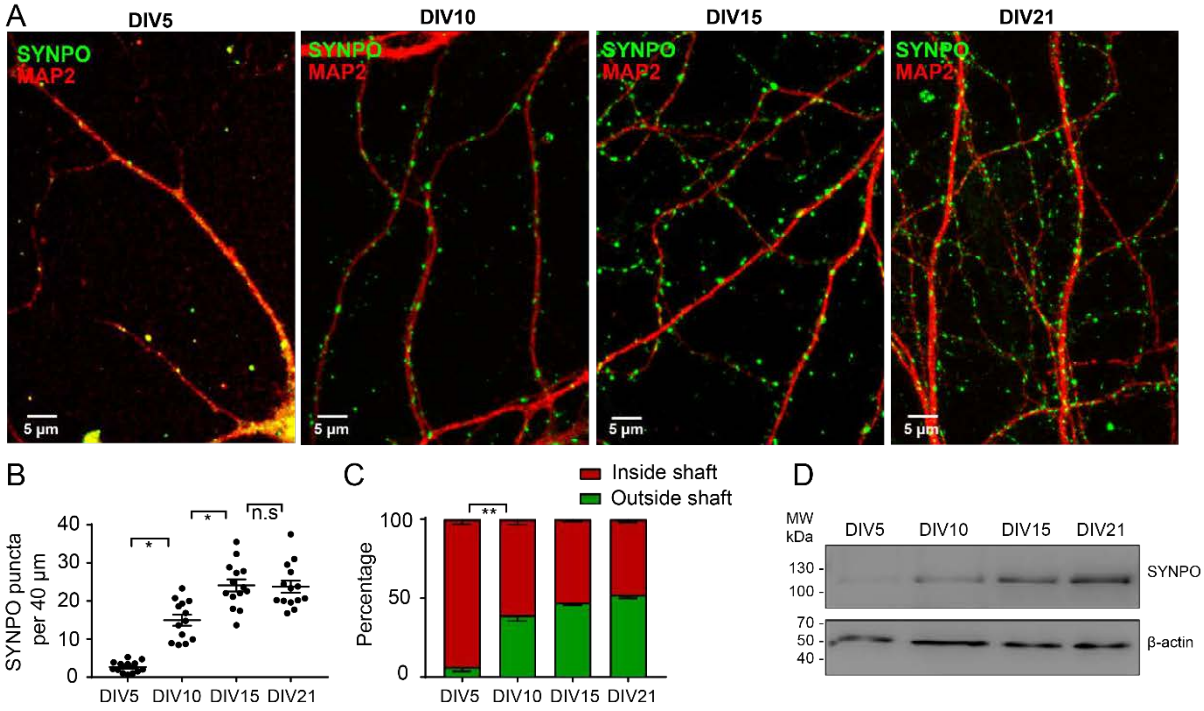

Figure 24. Expression and localization of synaptopodin in hippocampal primary neuron development
(A) Representative confocal images of primary hippocampal neurons on DIV5, DIV10, DIV15 and DIV21 stained with anti-synaptopodin and anti-MAP2 antibodies. Scale bar = 5 µm.
(B) Quantification (mean ± SEM) of the average number of total synaptopodin puncta per 40 µm dendritic segments at DIV5, DIV10, DIV15 and DIV21. Kruskal-Wallis-Test with Dunnett's post hoc test * p=0.0493 (DIV5 vs. DIV10), p = 0.0421 (DIV10 vs DIV15).
(C) Quantification (mean ± SEM) of synaptopodin puncta present inside or outside (spines, filopodia) of dendritic shafts. Kruskal-Wallis-Test with Dunnett's post hoc test ** p=0.0077 (DIV5 vs. DIV10).
(B+(C) DIV5: n = 13 cells from 3 independent cultures with 44 dendritic segments counted. DIV10: n = 14 cells from 3 independent cultures with 63 separate segments counted. DIV15: n = 14 cells from 2 independent cultures with 93 separate segments counted. DIV21: n = 16 cells from 3 independent cultures with 100 separate segments counted.
(D) Immunoblot showing developmental expression of synaptopodin in primary hippocampal cultures. β-actin is used as loading control.

Confocal imaging showed that at DIV5 there were very few synaptopodin puncta found in dendrites labeled by MAP2 staining. At DIV10, a clear synaptopodin signal was detectable (Figure 24A). The total number of puncta increased until DIV15 (Figure 24B-C). Similarly, immunoblotting of cell lysates prepared from DIV5, 10, 15 and 21 primary hippocampal cultures indicated gradual increase in synaptopodin expression during neuronal development and maturation (Figure 24D). In the next set of experiments we included the postsynaptic marker homer1 and the F-actin marker phalloidin, to

visualize dendritic spines. We observed an increased colocalization of synaptopodin with homer1 in mature cultures (Figure 25). On average about 3 % of synaptopodin puncta were adjacent to homer1-positive synapses in DIV5 neurons, while this number increased to 48 %, 64% and 62% on DIV10, DIV15 and DIV21, respectively (Figure 25B), indicating an increase in synaptic association of synaptopodin clusters.

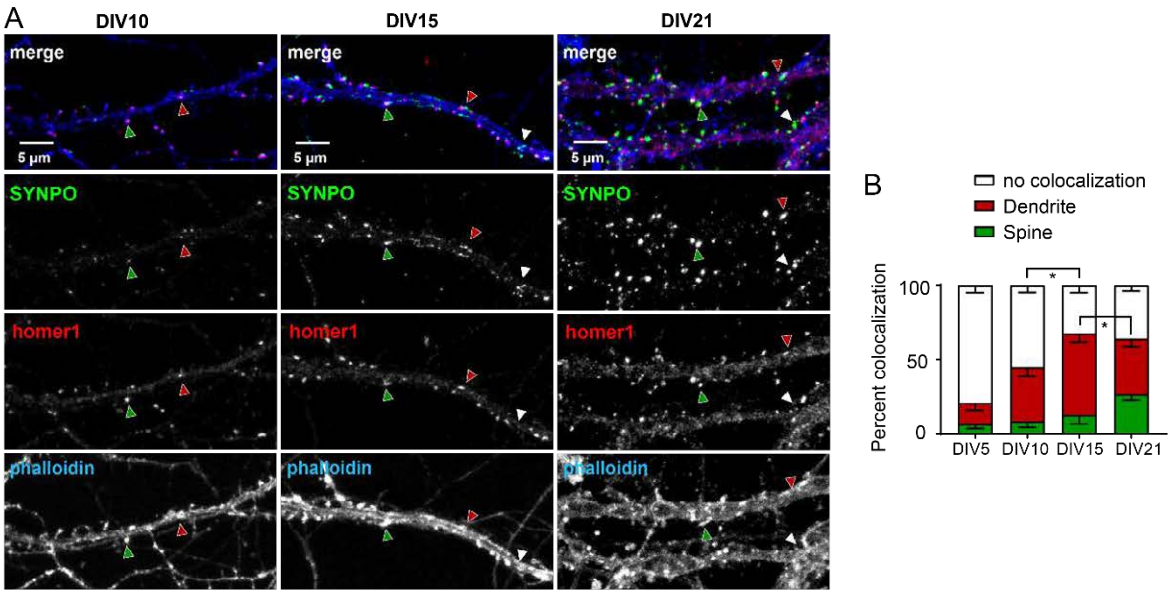

Figure 25. Synaptic localization of synaptopodin (Homer1 co-localization) increases with neuronal maturation

(A) Representative confocal image of primary hippocampal neurons at DIV10, DIV15 and DIV21 stained with anti-synaptopodin, anti-homer1 and phalloidin-A647N. Red arrows: colocalization of synaptopodin and homer1 in dendrite. Green arrow: colocalization in spine. White arrow: no colocalization. Scale bar = 5 µm.

(B) Quantification (mean ± SEM) of the percentage of synaptopodin puncta colocalizing with homer1 in different dendritic subcompartments. Mixed ANOVA with DIV as between and localization as within group factors. $F(4, 36)=4.4359$, $p=0.00512$. Newman-Keuls post hoc test: * $p=0.0348$ (no coloc DIV10 vs DIV15), $p=0.0435$ (DIV15 vs DIV21 dendrite). DIV5: n = 13 cells from 3 independent cultures with 44 separate segments counted. DIV10: n = 8 cells from 3 independent cultures with 44 separate segments counted. DIV15: n = 7 cells from 2 independent cultures with 35 separate segments counted. DIV21: n = 8 cells from 2 independent cultures with 41 separate segments counted.

All in all, we found that synaptopodin levels and the degree of synaptic localization increased with the maturation of the cultures and reached a maximum between DIV15-DIV21. We therefore continued to use DIV17-DIV21 cultures for our experiments. This developmental increase is in accordance with data published on the synaptopodin-dependent maturation of the cisternal organelle of the AIS (Sánchez-Ponce *et al*, 2012, 2011).

Interestingly, we also observed a large number of synaptopodin clusters adjacent to homer1 in locations that seem to be inside the dendritic shaft, as opposed to spine localization. Some of those certainly can be accounted for by spines that reach out orthogonally to the plane of view. However, such spines are generally rare in primary neuronal culture, and we speculate that some of these sites might constitute excitatory shaft synapses that are associated with synaptopodin clusters, or even a proper SA structure.

Synaptopodin clusters are closely associated with F-actin

Synaptopodin is an actin-associated protein (Asanuma *et al*, 2005; Kremerskothen *et al*, 2005; Mundel *et al*, 1997). However, the detailed spatial relation of synaptopodin puncta to neuronal F-actin has never been resolved in detail, due to the diffraction limit of fluorescence imaging techniques used in earlier studies (Sánchez-Ponce *et al*, 2012; Vlachos *et al*, 2009). Only recently, super-resolution imaging based on stochastic optical reconstruction microscopy (STORM) and photoactivated localization microscopy (PALM) were used to show the association of overexpressed Dendra-synaptopodin with F-actin in a neck of dendritic spines in hippocampal primary neurons (Wang *et al*, 2016). Here we decided to visualize endogenous synaptopodin by employing stimulated emission depletion (STED) nanoscopy. To this end, we stained hippocampal primary neurons with antibodies against synaptopodin and MAP2 or homer1, while the F-actin cytoskeleton was visualized by phalloidin-Atto647N. Two-color STED imaging of synaptopodin and F-actin indicated that synaptopodin-labeled structures were embedded inside an F-actin mesh both at the spine- and shaft localizations, as well as the AIS (Figure 26A-D). As already shown in Figure 26E-F, we again identified synaptopodin clusters close to homer1-positive synapses inside the dendritic shaft, which we hypothesize to constitute shaft-synapse associated SAs. This leaves the question about the function of non-synapse associated synaptopodin puncta inside the shaft. We suggest that, in analogy to the AIS, dendrites also may contain an equivalent of the cisternal organelle (Figure 26C, blue arrow) that could be involved in dendritic calcium regulation and buffering. In some cases, we were able to resolve a stack-like organization of individual synaptopodin clusters in dendrites, similar to those found in the AIS (Figure 26D), which speaks in favor of this hypothesis. However, these occasions were rare since the stacks need to be perfectly orthogonal to the imaging plane to visualize them. Electron microscopy studies combined with immunogold labeling could shed some light on the identity of these structures in the future.

Comparative analysis of synaptopodin puncta showed that there were no significant differences in size distribution between spine-localized clusters and those in the shaft (Figure 26E). In both cases more than 90% of them were enriched in F-actin (Figure 26F) and there was a clear correlation between the intensity of synaptopodin and F-actin levels (Figure 26G). As described in the previous chapter and in (Bommel et al. 2019), F-actin patches within the dendritic shaft are often part of (putative) excitatory shaft synapses. A highly interesting follow-up of this project will be to investigate whether the observed synaptopodin clusters in the dendritic shaft might be a structure similar to the SA, but localized at shaft- rather than spine synapses. A percentage of the actin patches we observed in the previous chapter might well have been part of such a structure, rather than “free” F-actin within the dendrite. Furthermore, we hypothesize that those synaptopodin clusters that are not associated with any type of synapse (i.e. not located in a spine head nor at a shaft synapse) could mark a dendrite-specific counterpart of the cisternal organelle, which so far has only been described in the axon initial segment. As a follow-up study, a through quantitative electron-microscopy study of those structures could shed some light on this question.

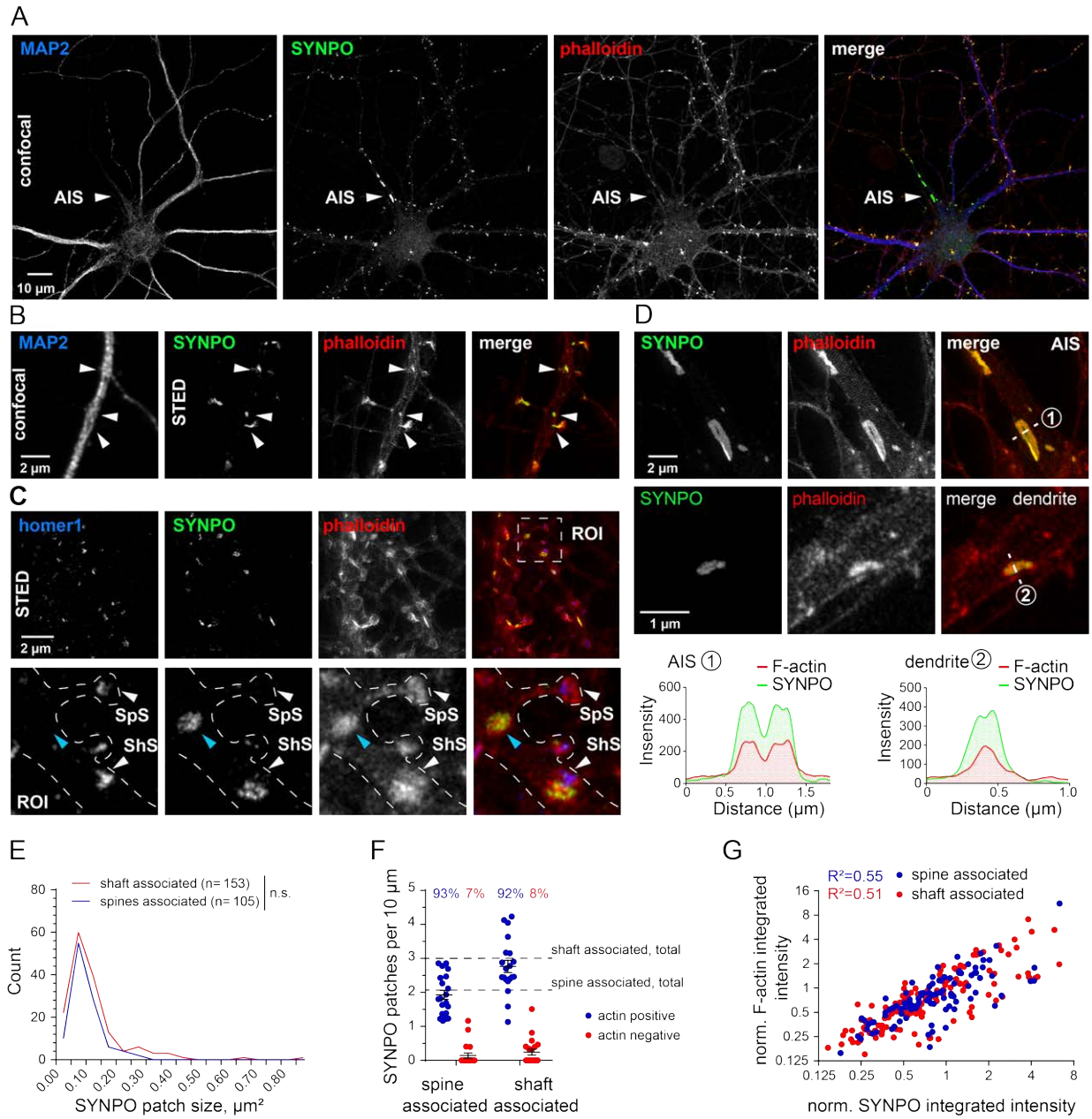

Figure 26. Synaptopodin is closely associated with F-actin in spines and inside dendritic shafts

(A) Confocal overview image of a DIV17 primary hippocampal neuron with F-actin stained by phalloidin-A647N and immunostaining of endogenous synaptopodin and MAP2. White arrow indicated the AIS. Scale bar = 10 µm.

(B) Confocal (MAP2) and STED image (phalloidin, synaptopodin) show F-actin enriched synaptopodin patches in spine necks and dendritic shaft. Scale bar = 2 µm.

(C) Upper row: STED image of DIV17 hippocampal neuron stained for homer1, synaptopodin and F-actin (phalloidin). White box indicates ROI shown in higher magnification in lower row: White arrows indicate homer1-positive synapses (SpS = spine synapse; ShS = shaft synapse). The shaft synapse is also associated with synaptopodin. Blue arrow indicates dendritic synaptopodin cluster positive for F-actin but not associated with a synapse. Scale bar = 2 µm.

(D) Comparison of the cisternal organelle found in the AIS (upper row), and dendritic synaptopodin patches (middle row). Lower row shows line profiles of phalloidin (F-actin) and synaptopodin intensity of the cisternal organelle (1) and dendritic synaptopodin patch (2). Scale bar = 2 µm (upper), 1 µm (middle).

Cont'd from Fig. 26: (E) Size distribution of synaptopodin patches associated with a synaptic spine or the dendritic shaft. Mann-Whitney-U test, p = 0.35. Shaft-associated spots: n = 153; spine-associated spots: n = 105; from 20 dendritic segments of 17 neurons in 2 independent cultures.
(F) Quantification of shaft- and spine-associated synaptopodin patches that are colocalizing with F-actin. n = 20 dendritic segments of 17 neurons in 2 independent cultures.
(G) Correlation of fluorescence intensity of synaptopodin and F-actin in shaft- and spine-associated synaptopodin patches. Shaft-associated patches: n = 141; spine-associated patches: n = 99; from 20 dendritic segments of 17 neurons in 2 independent cultures.

Inhibition of myosin V reduces the number of synaptopodin clusters

The question still remained how synaptopodin clusters, or the SA, are targeted or localized to specific sites. As we found both myosin V and myosin VI as putative interactors of synaptopodin in the mass spectrometry analysis (Figure 23), and we already showed in the previous chapter that myosin V is involved in stopping certain cargoes at F-actin rich sites within the dendrite (Figure 21), we hypothesized that likewise, myosin V (or myosin VI) might play a role in dendritic targeting of synaptopodin.

As myosin VI was a very strong interactor in the pulldown from brain lysate (Figure 23), we first focused on this motor. In collaboration with Dr. Wagner and Prof. Kneussel at the ZMNH we got access to the myosin VI-deficient Snell's waltzer (Myo6 sv/sv) mouse line, described in (Avraham *et al*, 1995). These mice carry a muta tion in the myosin VI gene, which causes a frameshift and a premature stop codon (130 bp deletion), and thus lack functional myosin VI. We prepared primary hippocampal cultures from wild-type and Myo6 sv/sv mice to investigate whether they showed a synaptopodin phenotype. Neurons were fixed at DIV8, 14 and 17 and stained against synaptopodin, homer1 and F-actin (Figure 27A). Quantification of confocal images showed that, very similarly to rat primary neuronal cultures, the number of synaptopodin puncta increased during development in both wild-type and Myo6sv/sv dendrites. Those numbers did not significantly differ between the genotypes (Figure 27B). Also the distribution of homer1-colocalized synaptopodin clusters to spines and dendritic shafts was not statistically different in Myo6sv/sv neurons compared to control (Figure 27C).

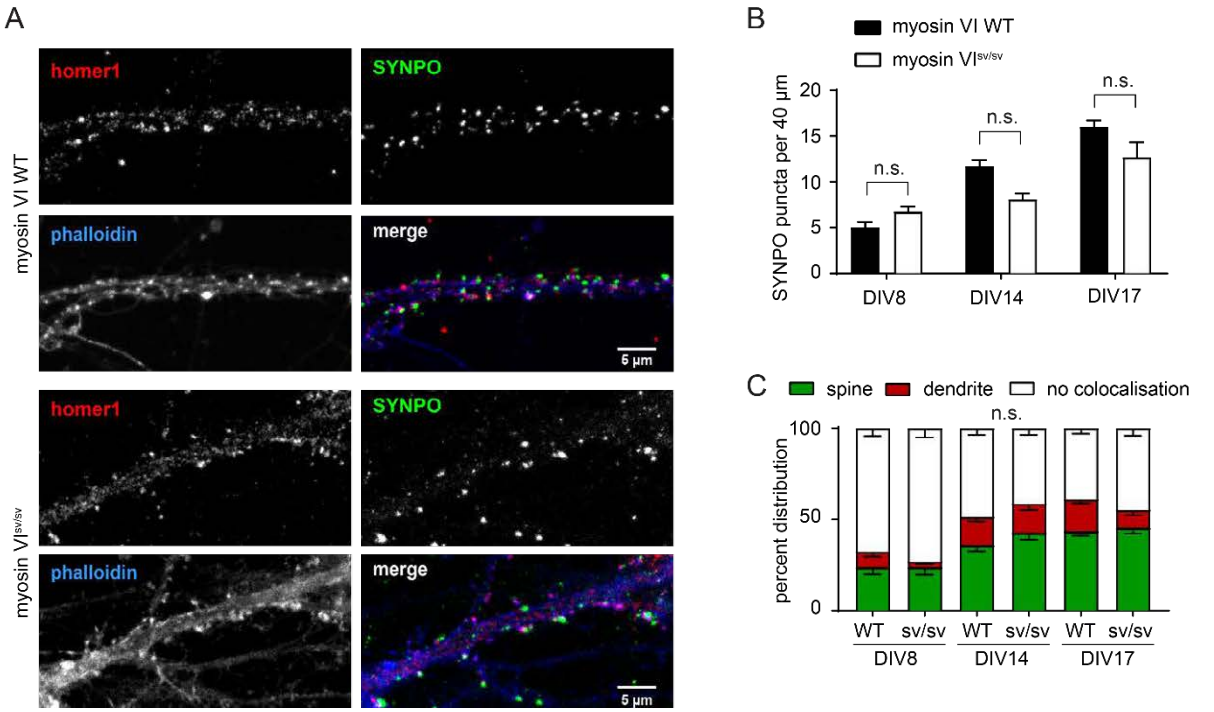

Figure 27. Myosin VI activity is not required for correct localization of synaptopodin
(A) Representative confocal image of primary hippocampal neurons on DIV17 from wild type (WT) and myosin VI-deficient (*Myo6*$^{sv/sv}$) mice stained with anti-synaptopodin, anti-homer1 and phalloidin-A647N. Scale bar = 5 µm. **(B)** Quantification (mean ± SEM) of the number of total synaptopodin puncta per 40 µm dendritic segments in WT and *Myo6*$^{sv/sv}$ neurons. Two-Way ANOVA, wt vs ko p=0.1364 (n.s.). **(C)** Quantification (mean ± SEM) of the percentage of synaptopodin puncta colocalizing with homer1 inside dendritic shafts or spines in WT and *Myo6*$^{sv/sv}$ cultures. Mixed ANOVA with DIV as between and localization as within group factors shows no significant differences. F(2, 22)=1.3869, p=0.271. (B+(C) All data comes from two independent cultures. DIV8 WT: n=7 cells with 30 segments counted. DIV14 WT: n=8 cells with 32 segments counted. DIV17 WT: n=8 cells with 47 segments counted. DIV8 KO: n=6 cells with 23 segments counted. DIV14 KO: n=6 cells with 31 segments counted. DIV17 KO: n=8 cells with 28 segments counted.

To corroborate these findings, we decided to also test the effects of acute myosin VI and myosin V inhibition using a DN approach to inhibit the function of those myosins as described in the previous chapter (Figure 18) (Osterweil *et al*, 2005; Wu *et al*, 2002). To this end, we transfected DIV15-16 primary hippocampal neurons with dominant negative constructs or corresponding controls, fixed them after one day of expression and stained for endogenous synaptopodin and homer1. Both overexpressed DN constructs entirely filled dendrites and spines and thus could be used as a volume marker (Figure 28A, 29A).

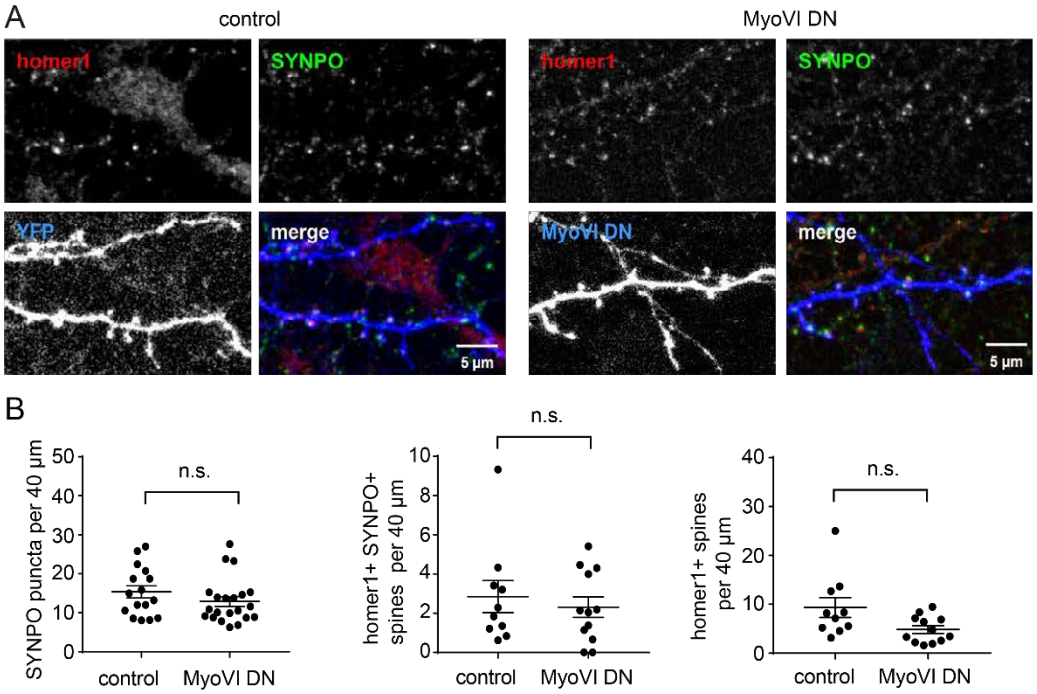

Figure 28. Inhibition of Myosin VI does not affect spine localization of synaptopodin puncta
(A) Representative confocal image of primary hippocampal neurons on DIV16 transfected with mRuby2 (control) or GFP-Myosin-VI-dominant-negative (MyoVI DN) and stained with anti-synaptopodin and anti-MAP2. Right column shows single color channels. Scale bar = 5 µm.
(B) Quantification (mean ± SEM) of the number of total synaptopodin puncta (left), the number of homer1-positive spines containing synaptopodin (middle), and the total number of homer1-positive spines (right) per 40 µm dendritic segments in control and MyoVI DN-expressing neurons. Unpaired t-test (two-tailed) showed no significant change. Left: Myo VI DN: n=21 cells from 4 independent experiments with 66 segments counted. Control: n=16 cells from 4 independent experiments with 40 segments counted. Middle+Right: Myo VI DN: n=12 cells from 2 independent experiments with 21 segments counted. Control: n=10 cells from 2 independent experiments with 18 segments counted.

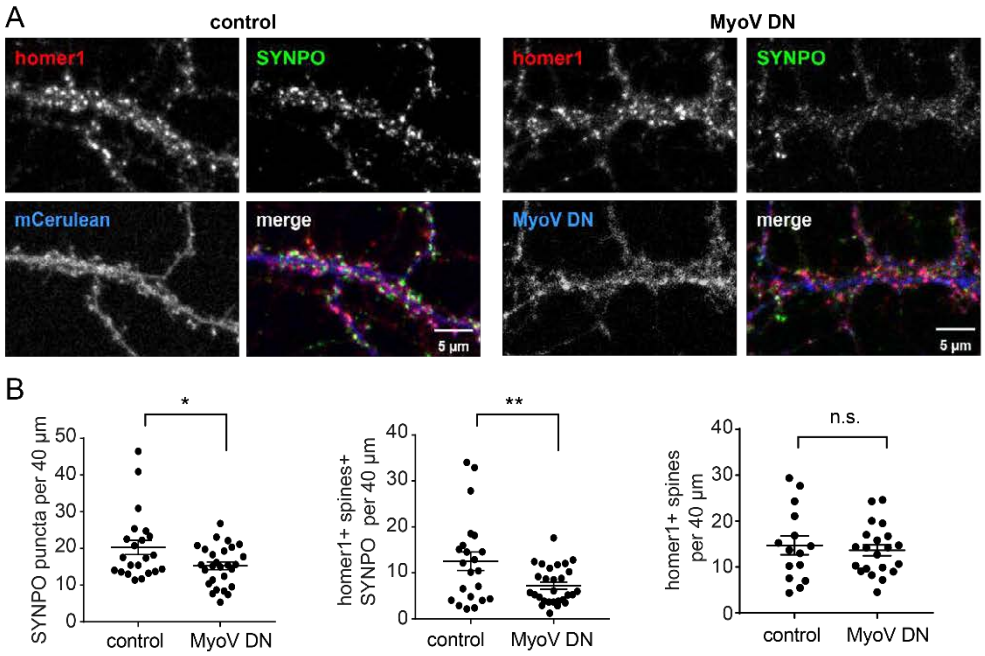

Figure 29. Myosin V inhibition affects spine localization of synaptopodin puncta
(A) Representative confocal images of primary hippocampal neurons on DIV16 transfected with mCerulean (control) or Myosin-V-DN-mCerulean (MyoV DN) and stained with anti-synaptopodin and anti-homer. Scale bar = 5 µm.
(B) Quantification (mean ± SEM) of the number of total synaptopodin puncta (left), the number of homer1-positive spines containing synaptopodin (middle), and the total number of homer1-positive spines (right) per 40 µm dendritic segments in control and MyoV DN-expressing neurons. MyoV DN showed a decrease in total synaptopodin puncta (Unpaired t-test (two-tailed) * p=0.0218), and in puncta localizing to homer1-positive spines (Unpaired t-test (two-tailed) ** p=0.0100), while the total number of spines was unchanged. MyoV DN: n=27 cells from 4 independent experiments with 51 segments counted. mCerulean: n=22 cells from 4 independent experiments with 54 segments counted.

Although quantification showed some reduction of synaptopodin puncta following overexpression of MyoVI DN, the difference to control neurons was not statistically significant (Figure 28B). On the other hand, MyoV DN expression resulted in a significant reduction of total synaptopodin clusters compared to control (on average 13.5 per 40 µm in MyoV DN and 24 per 40 µm in mCerulean control; Figure 29B). Significantly less synaptopodin puncta were found in association with dendritic spines (Figure 29B). Importantly, the total number of homer1-positive dendritic spines did not change (Figure 29B). This indicates that myosin Va is required for the formation or stability of synaptopodin clusters and most likely the associated SA. Thus, we conclude that the interaction of synaptopodin with myosin V, but not VI, is essential for the formation of synaptopodin clusters or for their normal distribution to dendritic spines.

Association of synaptopodin clusters with the ER in dendritic spines depends on myosin V

Since the number of synaptically localized synaptopodin clusters was reduced upon inhibition of myosin V, next we asked whether this would also affect localization of the whole SA. Synaptopodin is the only known marker for the SA, so in immunocytochemistry, its presence in spines is often equaled with the presence of a SA (Verbich *et al*, 2016; Wang *et al*, 2016). However, the only way to doubtlessly proof the presence of a bona fide SA would be to use electron microscopy, as only in EM the resolution is high enough to identify the SA structure. Since a quantitative EM study is technically very challenging

and was quite beyond the scope of this work, we looked for an alternative way to assess SA presence in spines. With the SA being an ER-based structure, we reasoned that simultaneous presence of synaptopodin and the ER inside a dendritic spine would be a good indicator for the presence of an actual SA. To test this, we co-transfected primary neurons with an ER marker fused to DsRed and either MyoV DN, MyoVI DN or control plasmids, and fixed them after one day of expression. Since the DsRed signal proved to be too dim and prone to bleaching during imaging, additionally to the endogenous synaptopodin immunostaining, we stained the ER-marker with an anti-RFP AbberiorStar-580 FluoTag (NanoTag). Confocal imaging showed that ER tubules could be seen inside a subset of dendritic spines (Figure 30A), and we interpreted co-localization of synaptopodin and the ER inside a dendritic spine as a SA. Quantitative analysis indicated that again the total number of synaptopodin puncta was reduced upon overexpression of MyoV DN, but not MyoVI DN (Figure 30B, C). The number of synaptopodin only- or the ER only-containing spines was slightly but not significantly decreased (Figure 30B) but the number of spines containing both the ER marker and synaptopodin (SA) was reduced specifically after expression of MyoV DN (Figure 30B), whereas the total spine density was again not affected by overexpression of either construct (Figure 30B, C). From this we conclude that myosin V, but not myosin VI, plays a role in localization or establishment of a SA at selected dendritic spines.

Synaptopodin clusters do not exhibit processive trafficking, but show differences in their molecular dynamics depending on their localization

As shown previously, the distribution of overexpressed, transfected GFP-synaptopodin closely matches the distribution of the endogenous protein (Vlachos *et al*, 2009). In this study, the authors used a construct expressing GFP-synaptopodin under the viral CMV (Cytomegalovirus) promotor. This is a very strong promotor that creates high overexpression levels, which we thought might have a negative impact on the health of the transfected cells, and which would furthermore express strongly in non-neuronal cells (glia cells) in the culture and create unwanted background. We therefore decided to generate a different construct for GFP-synaptopodin expression under the human synapsin 1 promoter, which is frequently used for low-to-moderate neuron-specific expression of proteins in primary neurons and organotypic slices (Kügler *et al*, 2003; Mikhaylova *et al*, 2016).

We asked whether GFP-synaptopodin clusters are actively transported within the dendrite, and how they are recruited into or removed from dendritic spines. However, time-lapse imaging of GFP-synaptopodin and mRuby2 co-expressing neurons did not reveal a single long-range transport event in dendrites over one hour of imaging with a 2 min interval (Figure 31A). Synaptopodin puncta in both spines and dendritic shafts were stably anchored at the same locations and sometimes oscillated within areas of 1-2 µm (Figure 31A). Subsequent staining of lysosomes in the same cell showed processive bidirectional transport, ensuring that dendritic cargo trafficking in the observed cell was not compromised in any way (Figure 31B). Continued imaging of transfected neurons over a 7 hour period also did not reveal any processive movement of GFP-synaptopodin clusters (Figure 31C). These observations are in line with our mass spectrometry results, as we did not find any kinesin or dynein motor proteins nor their adapters present in the synaptopodin complex (Konietzny *et al*, 2019). Based on this, we rule out the possibility that clusters of synaptopodin might be actively transported via long-distance microtubule-dependent, active transport. This leaves the scenario in which synaptopodin clusters form locally *de novo*, possibly via local mRNA translation, and then build up the SA in place. Further analysis of live imaging data confirmed that there are indeed instances where the synaptopodin signal gradually accumulated in a spine (Figure 31D).

A

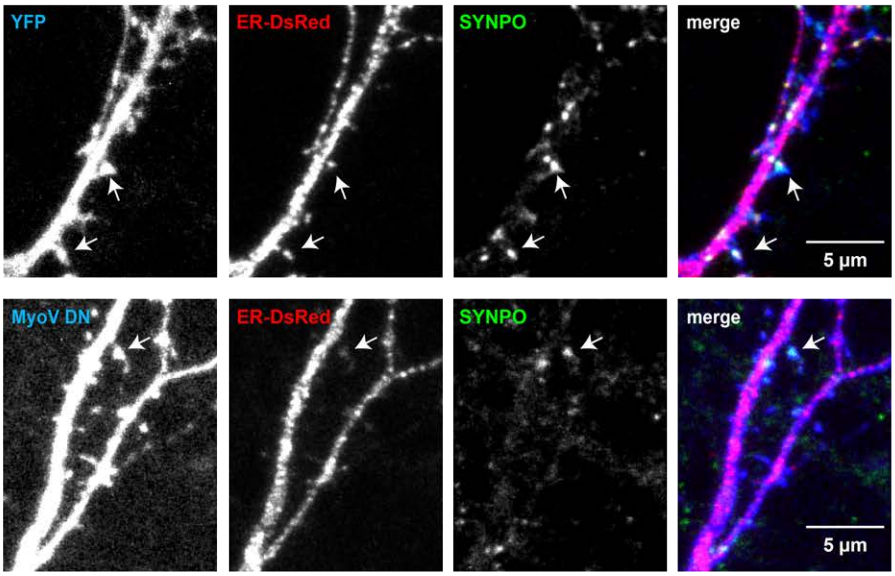

B Effect of MoyV DN on spine-localization of synaptopodin and the ER

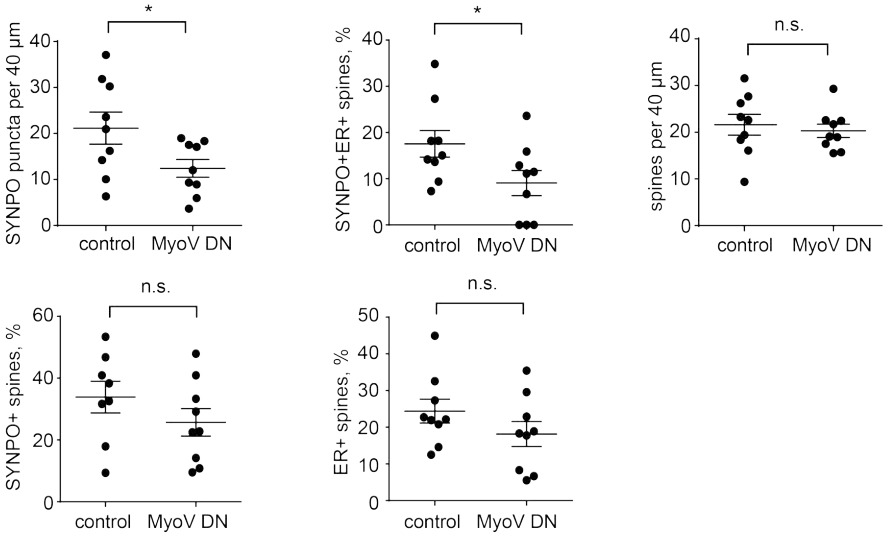

C Effect of MoyVI DN on spine-localization of synaptopodin and the ER

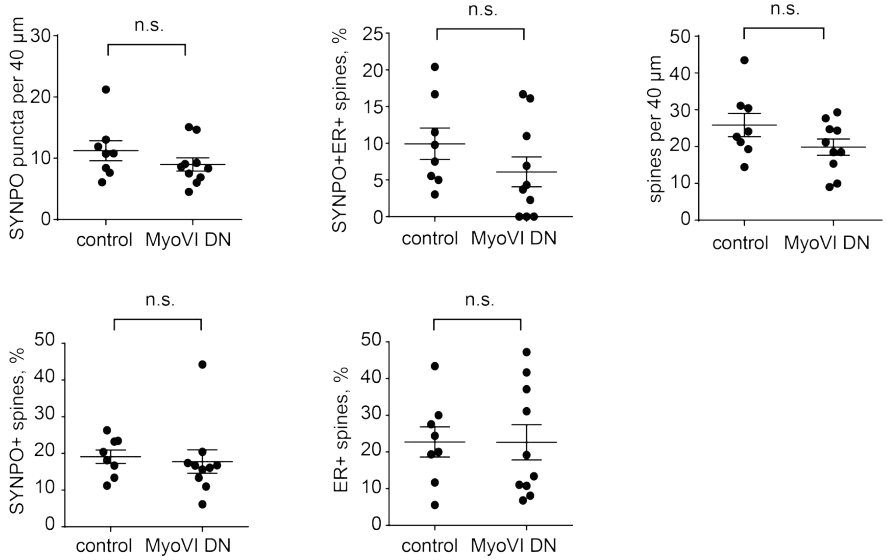

Figure 30. Myosin V inhibition affects the number of spines containing both synaptopodin and the ER
(A) Representative confocal images of primary hippocampal neurons on DIV17 transfected with an ER-marker and a cell fill (YFP; control) or MyoV DN, stained with anti-synaptopodin. Arrows indicate dendritic spines that are positive for both synaptopodin and ER. Scale bar = 5 µm.
(B) Quantification (mean ± SEM) of the number of synaptopodin puncta, the percentage of spines that are positive for both synaptopodin and ER, the number of spines per 40 µm, the percentage of spines that are synaptopodin positive, and the number of ER-positive spines for control and MyoV DN cells. MyoV DN showed a decrease in total synaptopodin puncta (Unpaired t-test (two-tailed) * p=0.043) and in spines containing both synaptopodin and the ER (Unpaired t-test (two-tailed) * p=0.0481). Myo V DN: n=9 cells from 2 independent experiments with 22 segments counted. mCerulean: n=9 cells from 2 independent experiments with 23 segments counted.
(C) Quantification (mean ± SEM) of the number of total synaptopodin puncta, the percentage of spines that are positive for both synaptopodin and ER, the number of spines per 40 µm, the percentage of spines that are synaptopodin positive, and the number of ER-positive spines for control and MyoVI DN cells. Myo VI DN: n=10 cells from 2 independent experiments with 22 segments counted. Control: n=8 cells from 2 independent experiments with 22 segments counted. MyoVI DN had no significant effect on the measured parameters.

So far, we found that both dendritic and synaptic synaptopodin clusters are closely associated with patches of F-actin and are stable at their locations over many hours (Figure 26, Figure 31). To further characterize spine- v s. dendritic shaft-localized synaptopodin clusters, we performed fluorescence recovery after photobleaching (FRAP) experiments in neurons expressing GFP-synaptopodin and mRuby2 as a morphology marker (Figure 32A). Interestingly, a subset of the photobleached synaptopodin clusters did not recover any fluorescence at all, so only those clusters that recovered at least 10% of their initial fluorescence value were considered in the FRAP analysis. We found that GFP-synaptopodin clusters in dendritic spines and in the shaft had very different molecular dynamics: after photobleaching, clusters inside dendritic spines recovered fluorescence intensity much faster than shaft-associated clusters, indicating that spine-localized clusters contain a larger dynamic pool of synaptopodin (Figure 32B,C). Since both shaft- and spine-localized synaptopodin clusters are associated with the F-actin cytoskeleton, and the turnover rate of F-actin is the same in both locations (Bommel *et al*, 2019), it is unlikely that actin dynamics play a role in synaptopodin stability. One possible explanation could be that synaptopodin clusters inside spines represent the SA, whereas shaft-associated clusters might constitute a different kind of ER-based compartment, possibly more similar to cisternal organelles. In this case, the differences in synaptopodin stability are due to the different nature and molecular composition of those organelles.

Incubation of neurons with the pharmacological myosin V inhibitor MyoVin, or with the myosin VI inhibitor TIP, did not significantly affect the recovery kinetics at either location. However, the number of synaptopodin puncta that did not recover at all was significantly increased upon treatment with MyoVin (Figure 32B-D), which indicates an involvement of myosin V in the local availability of synaptopodin.

In summary, we found evidence that myosin V, rather than myosin VI, is involved in the formation or stabilization of synaptopodin clusters and/or the SA at F-actin rich areas. It is plausible that synaptic activity has an influence on synaptopodin accumulation, e.g. via control of myosin V activity, or via downstream phosphorylation of synaptopodin. This would provide an additional explanation for the differences observed in spine- and shaft-localized synaptopodin dynamics.

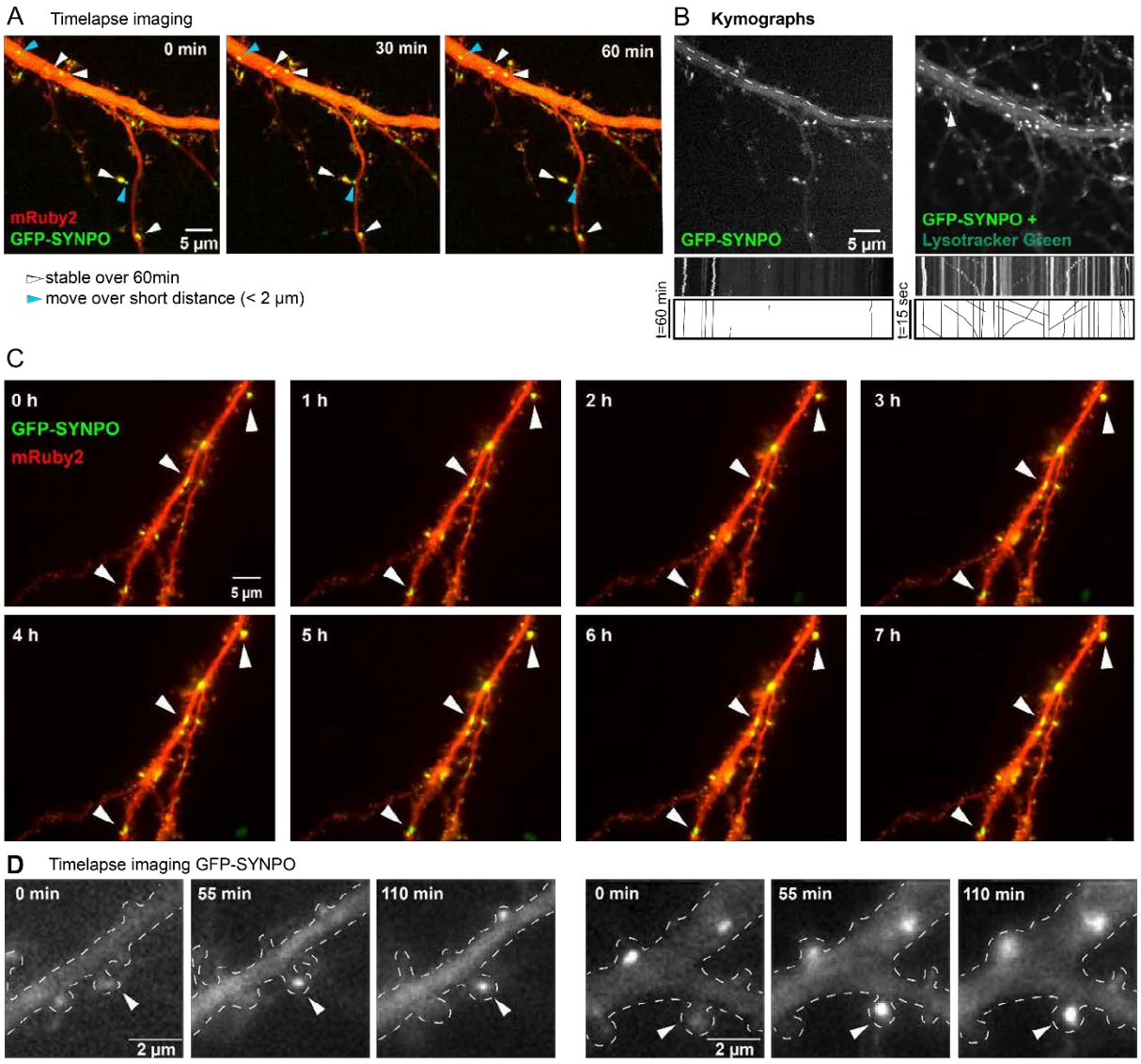

Figure 31. Synaptopodin puncta are largely immobile, are generated *de novo* in dendritic spines
(A) 60 min time-lapse imaging of a primary hippocampal neuron (DIV17) expressing GFP-synaptopodin and mRuby2. Images were acquired with a 2 min interval. White arrows indicate synaptopodin puncta that were stably localized over the entire imaging period. Blue arrows indicate puncta that moved over very short distances (< 2 µm). Scale bar = 5 µm.
(B) Shown is the same neuron as in (A). Left: Kymograph of the main dendritic shaft in the synaptopodin channel over the 60 min imaging period. Right: After 60 min imaging, Lysotracker Green was added to the imaging medium and the cell was imaged for 15 seconds with a 1 second interval. The kymograph shows moving lysosomes in the previously imaged cell. Scale bar = 5 µm.
(C) Time-lapse imaging of a primary hippocampal neuron (DIV15) transfected with mRuby2 and GFP-synaptopodin followed over 7 h with 5 min intervals. Shown are frames 1 h apart, no changes were observed between these timepoints. Arrowheads indicate examples of GFP-synaptopodin puncta that were stable over the entire imaging period. Scale bar = 5 µm.
(D) Example images from a 110 min time-lapse imaging of a primary hippocampal neuron (DIV15) expressing GFP-synaptopodin. Images were acquired with a 5 min interval. Synaptopodin-puncta can be observed gradually emerging in dendritic spines (white arrows). Scale bar = 2 µm.

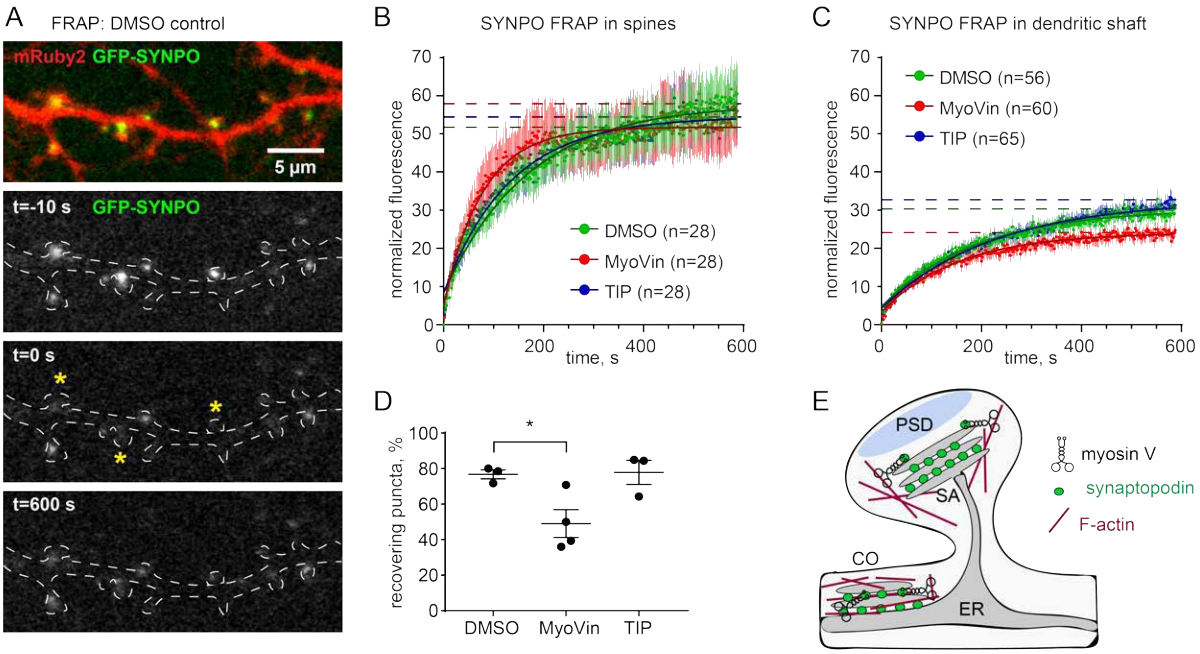

Figure 32. Synaptopodin turnover rate is affected by inhibition of myosin V, but not myosin VI
(A) Analysis of synaptopodin dynamics using FRAP. Example images of a DIV17 primary hippocampal neuron expressing GFP-synaptopodin and mRuby2, before, during and after photobleaching of selected synaptopodin puncta (asterisks).
(B) FRAP quantification for synaptopodin puncta localized in spines. Compared were fluorescence recovery rates in control (DMSO) and myosin V-inhibitor (MyoVin, 30 µM for 20 min) or myosin VI-inhibitor (TIP, 4 µM for 20 min) treated cells. In the analysis, only those puncta that recovered >10% of their initial fluorescence were considered. 1-phase-association fits, n numbers and plateaus are indicated (DMSO 58±1, MyoVin 52±0.7, TIP 54±0.8). RM-2-Way ANOVA: treatment n.s.
(C) FRAP quantification for synaptopodin puncta localized in the dendritic shaft. 1-phase-association fits, n numbers and plateaus are indicated (DMSO 30±0.4, MyoVin 24±0.3, TIP 33±0.5). RM 2-Way ANOVA: treatment n.s.
(D) Percentage of puncta that were considered "recovering" (recovered > 10% of their initial fluorescence). One-Way ANOVA with Dunnett's post hoc test, DMSO vs MyoVin * p=0.0376. DMSO: n=3 independent experiments with 84 puncta analyzed, MyoVin: n=4 with 124 puncta analyzed, TIP: n=3 with 81 puncta analyzed.
(E) Model summarizing the role of myosin V and synaptopodin interaction in localization of the SA to actin filaments associated with spine or shaft synapses. PSD – post-synaptic density. SA – spine apparatus, CO – cisternal organelle.

As for the involvement of myosin V, there are several possible scenarios how it could contribute to SA formation. We speculate that, since myosin V is responsible for targeting the ER to dendritic spines in Purkinje neurons, it might also fulfil this role in hippocampal neurons. It is conceivable that myosin V is required to initially localize an ER protrusion to a dendritic spine, which would be followed by accumulation of synaptopodin and formation of the SA (Figure 32E). While we observed a trend in the decrease of ER-positive spines under myosin V DN conditions, the difference was not statistically significant. It seems more likely that myosin V is involved in the enrichment of synaptopodin at selected spines, which then leads to the formation of a whole SA. This enrichment could be achieved both via interaction of synaptopodin with actin-bound myosin V, or additionally via anchoring of dendritic synaptopodin mRNA that is then locally translated (Balasanyan & Arnold, 2014). In our experiments

we did not unambiguously show whether the synaptopodin-myosin interaction is direct or indirect via a third protein or adapter. It is therefore possible that myosin and synaptopodin are part of the same, larger protein complex that regulates local synaptopodin availability and/or SA formation. Another interesting question for future studies is how local synaptopodin distribution, or *de novo* formation of a SA, relates to synaptic activity. Considering that the activity of myosin V is calcium-dependent, this could provide selectivity for synaptic targeting.

Chapter 3: Caldendrin as a novel interactor of Myosin V

Parts of the presented work have been conducted with the help of Nathalie Hertrich and Jasper Grendel from the ZMNH (Hamburg), and with Jeroen Demmers and Dick Dekkers from the EMC mass spectrometry facility (Rotterdam).

We have recently shown that the calcium-sensing protein caldendrin plays a role in post-synaptic calcium signaling and actin dynamics (Mikhaylova *et al*, 2018). While performing a mass-spectrometric analysis of brain-specific interactors of the caldendrin N-terminus in collaboration with the Erasmus Medical Center in Rotterdam, we found several myosin proteins, including myosin V and VI, as potential new interaction partners. To corroborate these results for the wild type full-length caldendrin protein, I repeated the mass spectrometry analysis in the presence (0.5 mM $CaCl_2$) or absence (2 mM EGTA) of calcium. We again found unconventional myosins in the list of potential interactors, and the number of unique peptides identified was constantly higher in the calcium- compared to the EGTA condition (Figure 33, Figure 34).

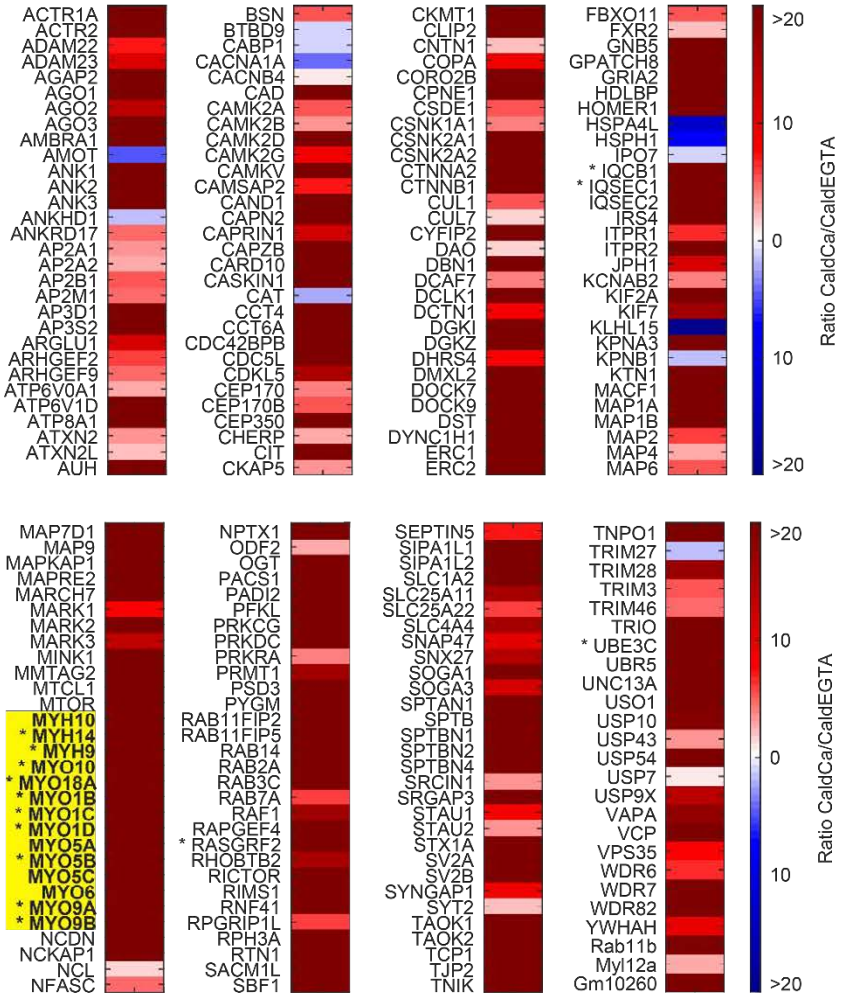

Figure 33. Mass-spectrometry analysis of putative caldendrin interactors. Selection of potential caldendrin-interactors identified in the mass spectrometry analysis. Highlighted in yellow are members of the actin-based myosin motor proteins. The vast majority of interactors are enriched, or exclusively present in the calcium-condition (dark red colour). Asterisks indicate proteins that contain at least one IQ-motif according to the annotation in the Uniprot Database.

	unique peptide hits						
	bioGFP-Caldendrin		bioGFP control				
accession	EGTA	Ca2+	EGTA	Ca2+	symbol	description	
D3Z4J3	15	63	9	13	Myo5a	Myosin-Va	
E9Q175	7	37			Myo6	Myosin-VI	
Q61879	17	56	15	17	Myh10	Myosin heavy chain 10	Myosin-IIb subunit
Q8VDD5	11	29	7	7	Myh9	Myosin heavy chain 9	Myosin-IIa subunit
K3W4R2		24			Myh14	Myosin heavy chain 14	Myosin-IIc subunit
Q9WTI7		13			Myo1c	Myosin-Ic	
Q5SYD0	1	10		2	Myo1d	Myosin-Id	
K3W4L0	1	9			Myo18a	Myosin-XVIIIa	

Figure 34. Selected myosin family members from mass-spectrometry analysis. Excerpt from the mass spectrometry hit list. Several myosins were especially enriched at bio-caldendrin coupled beads in the presence of calcium, and showed little to no binding in the control condition (bio-GFP).

To verify whether caldendrin showed calcium-dependent binding to myosin, I performed co-immunoprecipitation assays from transfected cell lines. I co-transfected HEK293T cells with constructs for the over-expression of full-length caldendrin-tagRFP and either GFP-MyosinVa or GFP-MyosinVI. I further tested the interaction of the caldendrin N- and C-terminus separately with myosin V and VI, to determine whether it was indeed the N-terminus that mediated binding, as suggested by the mass spectrometry results. One day after transfection, the HEK cells were lysed and the lysate was incubated with GFP-trap beads (Chromotek) to pull down GFP-myosin. During the incubation I supplemented the cell lysate with either 0.5 mM $CaCl_2$ or 2 mM EGTA to test for calcium-dependent interaction. The beads were washed to remove unspecific interactors, and bound proteins were separated via SDS-PAGE and subjected to a western blot. GFP-myosin was visualized on the western blot membrane using an anti-GFP antibody, and co-purified caldendrin-tagRFP was visualized using an anti-tagRFP antibody. An empty tagRFP vector (tagRFP only control) was used to make sure that tagRFP did not by itself interact with GFP-myosin or the GFP-trap beads. I found that full-length caldendrin-tagRFP interacts with both GFP-myosin Va and GFP-myosin VI in a calcium-dependent manner, and that this interaction is mediated by the caldendrin N-terminus, rather than the C-terminus, which did not show any binding (Figure 35). We therefore concluded that, despite the similarity of the caldendrin C-terminus to calmodulin, there seems to be no interaction between the caldendrin C-terminus and the myosin IQ-motifs.

As the co-immunoprecipitation experiment was done in cell lysate, which contains thousands of proteins, I could not rule out that this interaction was mediated by a third interaction partner or adapter, rather than a direct interaction between myosin and caldendrin. To test this, I expressed GFP-myosin Va and VI in HEK cells and attached it to GFP-trap beads as described above, then washed and blocked the beads thoroughly to remove possible binding partners from HEK293 cells. Then I incubated the myosin-beads with a 100 nM solution of recombinant caldendrin produced in E. *coli*, both in the presence (100 µM $CaCl_2$) and absence (2 mM EGTA) of calcium. As a control I used a caldendrin calcium binding mutant (D243A, D280A, (Mikhaylova *et al*, 2018). The calcium binding mutant is thought to primarily exist in the closed, inactive conformation (Figure 6A). In accordance with that, I found that recombinant wt caldendrin, but not the mutant version, strongly interacted with GFP-myosin Va and with GFP-myosin VI in the presence of calcium (Figure 36). I therefore concluded that caldendrin interacts directly with myosin V and myosin VI in a calcium-dependent manner via its N-terminus.

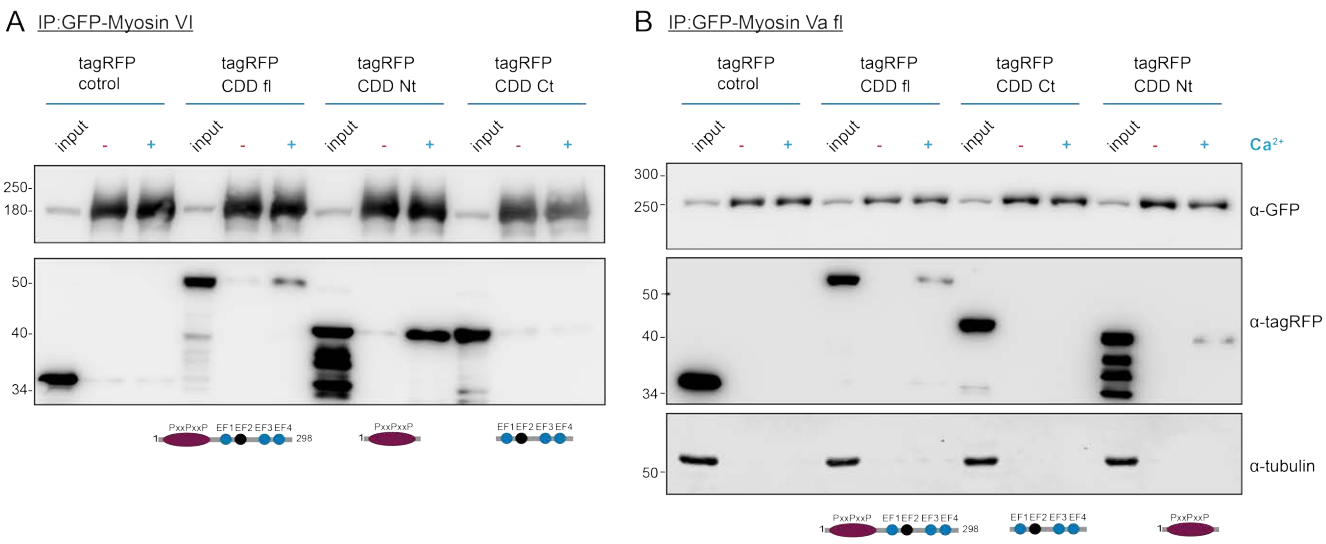

Figure 35. Immunoprecipitation from transfected HEK cells confirms a calcium-dependent interaction between both myosin V and myosin VI with the caldendrin N-terminus. (A) HEK293T cells were co-transfected with GFP-myosin VI, and either tagRFP-caldendrin full length (fl), tagRFP-caldendrin N-terminus (Nt) or tagRFP-caldendrin C-terminus (Ct). The transfected cells were lysed, and GFP-myosin was pulled down using GFP-trap beads. Co-precipitated tagRFP-caldendrin was visualized in a western blot using an anti-tagRFP antibody. **(B)** HEK293T cells were co-transfected with GFP-myosin Va and tagRFP-caldendrin construtcs to show calcium-dependent interaction as in (A). Staining with anti-tubulin was included as a loading control.

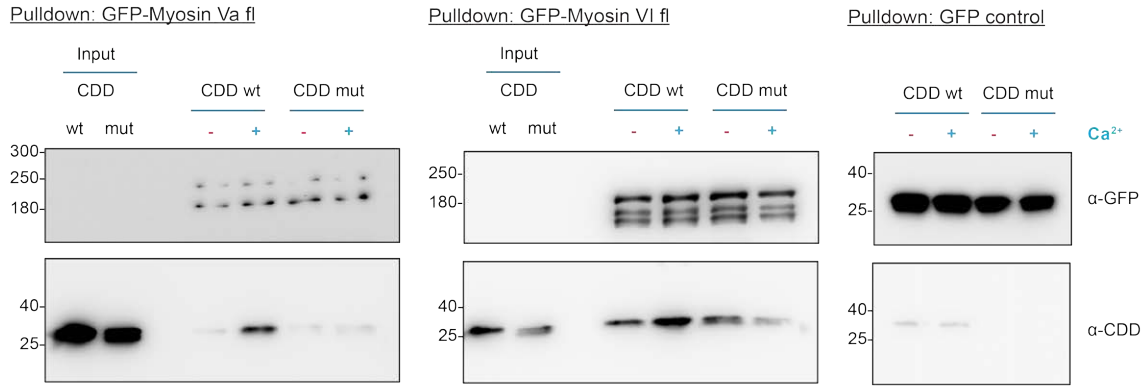

Figure 36. Pull-down of eukaryotically produced myosin Va and myosin VI confirms calcium-dependent interaction with recombinant wild type caldendrin, but not with a caldendrin calcium binding mutant. Left: GFP-myosin Va was produced in HEK cells and bound to GFP-trap beads. After thorough washing steps, the beads were incubated with 100 nM wild type (wt) or mutant (mut) caldendrin produced in E. coli. The mutant form (D243A, D280A) is lacking the calcium-binding ability. Caldendrin that was co-precipitated with the myosin-coupled beads was visualized in a western blot using an anti-caldendrin antibody. **Middle**: Interaction between eukaryotically produced GFP-myosin VI and recombinant caldendrin was shown as described for the left side. **Right**: Negative control, as on the left. Neither caldendrin wt nor caldendrin mut interact with GFP-bound GFP-trap beads.

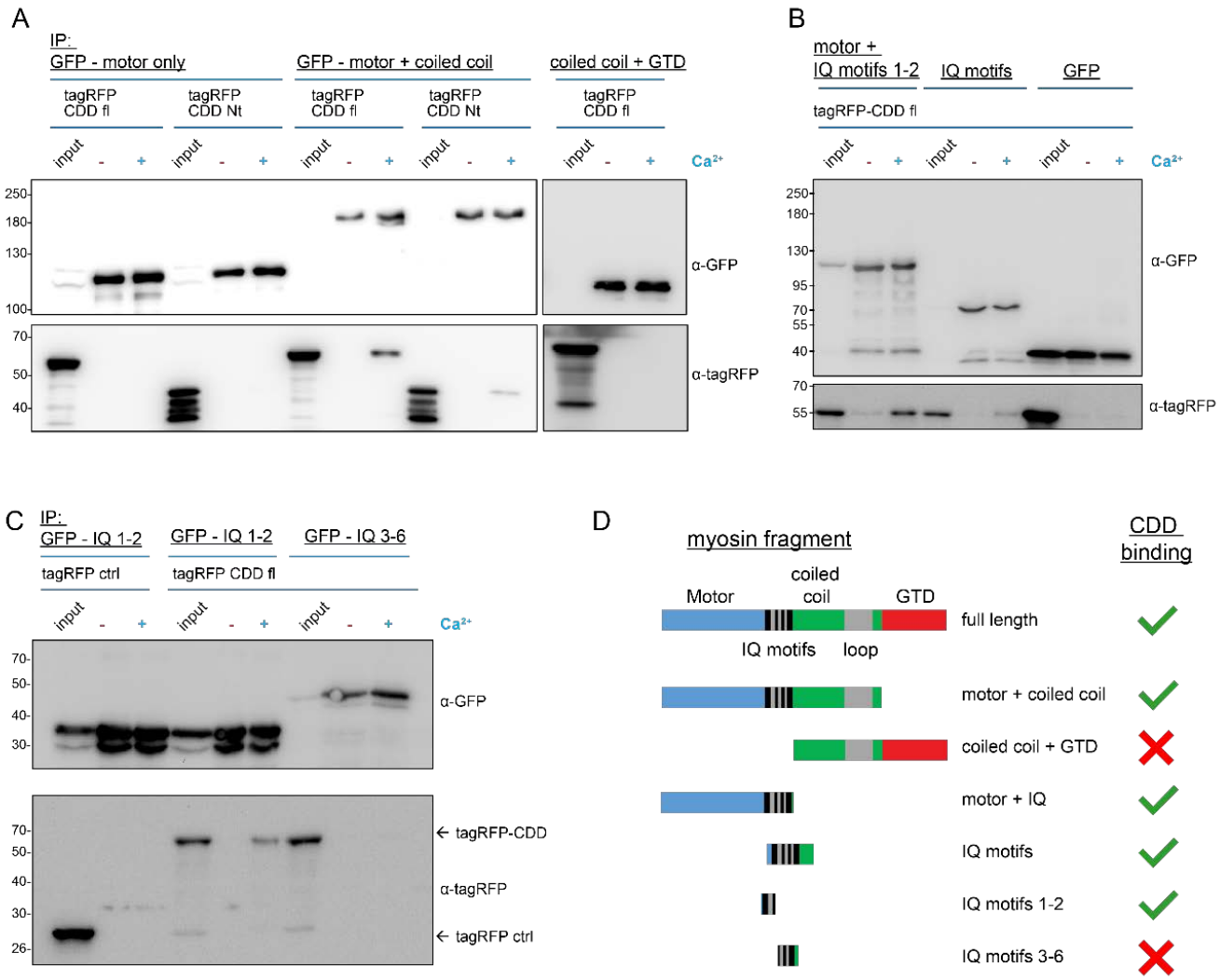

Figure 37. Co-immunoprecipitation of tagRFP-caldendrin with selected fragments of myosin Va narrowed down the binding region to IQ-motifs 1 and 2. (A) In co-immunoprecipitation from HEK293T cells, in the presence of calcium, caldendrin fl and Nt interact with a GFP-myosin Va fragment comprising the motor- and coiled-coil domain, but not with a fragment comprising coiled-coil and globular tail domain (GTD). **(B)** As in (A), in the presence of calcium, tagRFP-caldendrin fl interacts with a GFP-myosin Va fragment comprising the motor domain with only the first two IQ motifs, and with a fragment containing the whole IQ domain, but not with the GFP-tag. **(C)** In the presence of calcium, tagRFP-caldendrin, but not the tagRFP-tag by itself, interacts with a GFP-myosin Va fragment comprising only the first two IQ motifs. It does not interact with a fragment comprising the IQ-motifs 3-6. **(D)** Summary of the findings in (A-C). tagRFP-caldendrin binds a narrow region on myosin Va between the IQ-motifs 1-2 in a calcium-dependent manner.

Due to the involvement of myosin V in dendritic protein trafficking and organelle localization described in chapters 1 and 2, we decided to focus on the interaction between caldendrin and myosin V. To map the binding region I performed co-immunoprecipitation experiments with various fragments of myosin V. To this end, I separated the defined functional domains of myosin (motor$_{aa1-755}$, IQ-motifs$_{aa742-923}$, coiled-coil region$_{aa934-1227}$, and globular tail domain (GTD)$_{aa1228-1829}$) and performed the co-immunoprecipitation with caldendrin as described above for the full-length myosin. I first tested the motor domain only, motor domain + coiled coil region vs. the coiled coil region + GTD and found that both full length (fl) caldendrin and the caldendrin N-terminus bound only to motor + coiled coil (Figure 37A). I could therefore exclude binding to the GTD and the motor domain. In the next set of

experiments, I further tested the motor domain + the first two IQ motifs, and all six IQ motifs alone. I found that caldendrin interacted with both of them, from which I concluded that binding is not mediated via the coiled-coil region, but rather via the IQ motif region (Figure 37B). Finally, I tested Only IQ-motifs 1-2 vs. IQ-motifs 3-6, which revealed that caldendrin specifically interacts with the first two IQ-motifs of myosin V in a calcium-dependent manner (Figure 37C). These results are summarized in Figure 37D. This finding is very interesting, as specifically the calmodulin light chains bound to the first two IQ motifs are thought to regulate myosin V motor activity and processivity (Lu *et al*, 2012; Shen *et al*, 2016; Lu *et al*, 2006). It is very likely that caldendrin binding at this exact site will have an impact on myosin motor function. As caldendrin becomes activated inside dendritic spines during synaptic activity (Mikhaylova *et al*, 2018), we hypothesize that this could be a way of regulating myosin V activity in response to a synaptic input. In order to assess the effect of caldendrin biding to myosin V, I employed an *in vitro* F-actin gliding assay using purified proteins in a reconstituted motor-cytoskeleton system. I used a similar setup for the assay as described in (Preciado-López *et al*, 2014) and as shown in Figure 38.

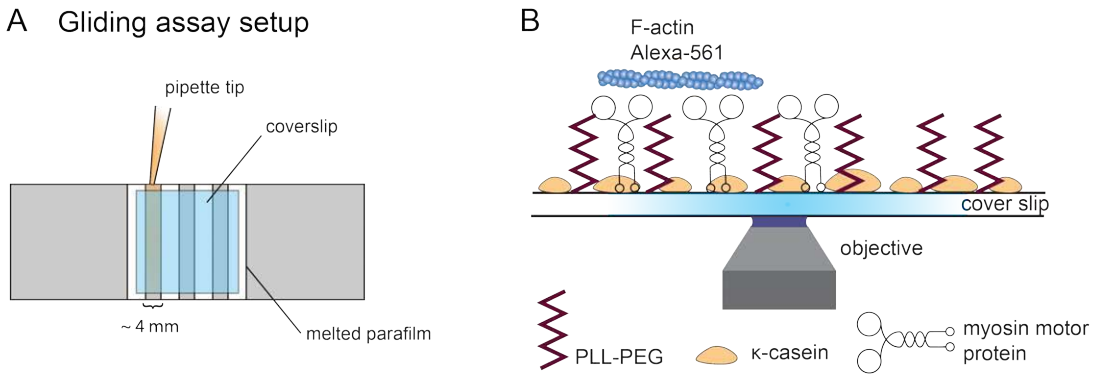

Figure 38. Setup of the in-vitro gliding assay. (A) Construction of the flow chambers from microscopy slice, para-film and glass coverslip. **(B)** Schematic representation of the assay components. The surface of the coverslip is coated with PLL-PEG and κ-casein to avoid excessive protein "stickiness". Purified myosin V motor proteins bind to un-occupied spaces on the surface. F-actin labelled with the Alexa-561 fluorophore can be observed being moved by the motor proteins.

To create small, separate reaction chambers for this assay setup, narrow flow-channels (~ 4 mm) are constructed on a microscope slide using parafilm and a coated glass coverslip (Figure 38A). The coverslip is coated with PLL-PEG (Poly-L-lysine-Polyethyleneglycol) and κ-casein to block the glass surface and prevent "sticking" of proteins. When the purified motor protein is added, some of it binds to still unoccupied spaces on the glass coverslip and forms a so-called "lawn" of motor-proteins. Fluorescently labelled actin filaments added to the channel can be observed "gliding" across the lawn of motor proteins (Figure 38B). We decided to use this assay setup to test full-length myosin Va activity in the presence or absence of CaM and caldendrin (Figure 39A). In order to reconstitute a minimal actin-myosin system *in vitro*, I purified full-length myosin Va, as well as caldendrin and calmodulin. Alexa-568 labelled and unlabeled actin were purchased from Thermo Fisher (A12374) and Tebu Bio (AKL99), respectively. I purified untagged CaM from E. *coli* via hydrophobic interaction chromatography with the help of H. Tidow (Uni Hamburg / Figure 39B), and untagged caldendrin from E. *coli* via a self-cleaving intein tag (Figure 39C). As full-length myosin V has never been successfully produced in bacteria, I opted for eukaryotic production using the HEK293T cell line. HEK cells were transfected with full length myosin V (StrepTag-GFP-tagged) and the protein was purified via

StrepTactin beads and eluted with biotin. Using this method, the purified myosin was already complexed with endogenous CaM from the HEK cells (Figure 39D, E).

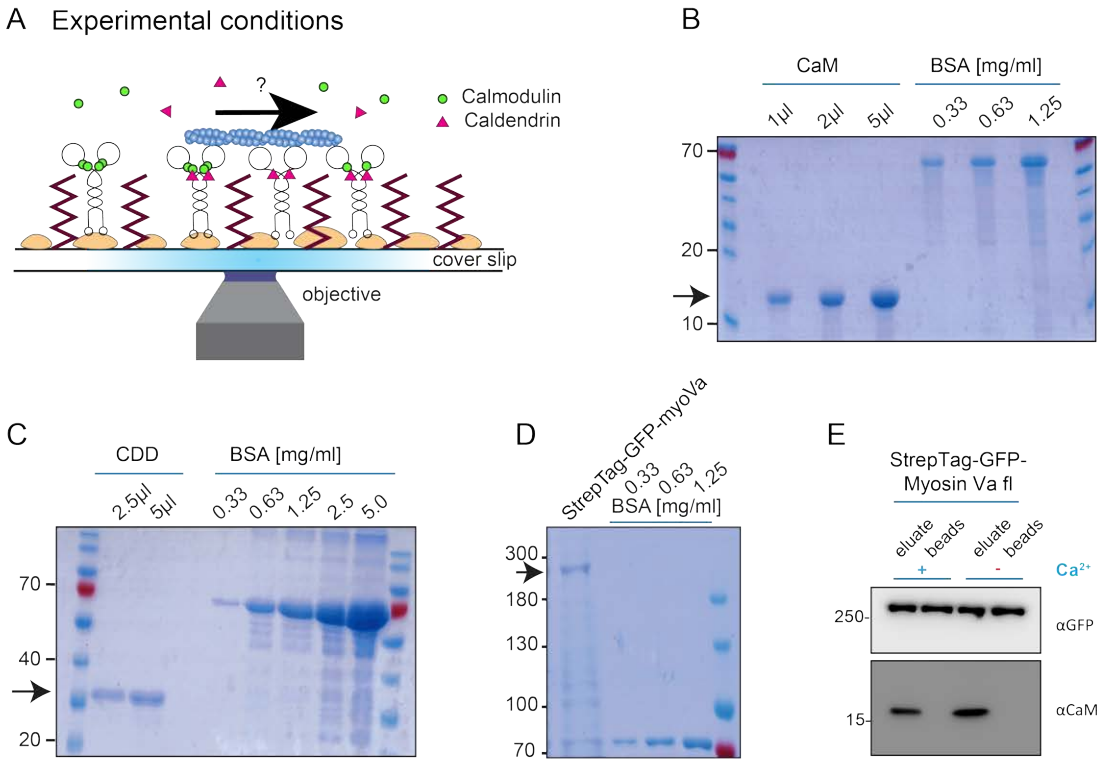

Figure 39. Purification of StrepTag-GFP-myosin Va, caldendrin and calmodulin for the in vitro gliding assay. (A) Experimental conditions. Tested were the motor activity of myosin Va in the presence of either calmodulin only, or calmodulin and caldendrin. **(B)** SDS-PAGE and coomassie staining of untagged calmodulin purified from E. *coli*. Different concentrations of BSA were loaded to estimate protein concentration. The arrow indicates the purified protein. **(C)** Purification of untagged caldendrin from E. *coli*. **(D)** Purification of StrepTag-GFP-myosin Va from HEK293T cells. **(E)** Western blot of StrepTag-GFP-myosin Va. Anti-GFP-antibodies were used to visualize the myosin construct. Development with anti-CaM antibodies shows the presence of cell-endogenous CaM in the eluate both the calcium (+) and in the EGTA (-) condition. Eluate = eluted myosin fraction. Beads = residual myosin protein bound to the beads after elution step.

Using this assay, I was able to observe actin filaments gliding over the lawn of myosin V (Figure 40A). When only CaM (30 µM) was present in the channel, on average 80 % of all filaments in the field of view were subjected to gliding over a course of thirty seconds (Figure 40B,C). Notably, when caldendrin was additionally present at a concentration of 4-5 µM, the number of mobile actin filaments dropped to about 35 % (Figure 40B, C). This indicates that caldendrin can act as an inhibitor of processive myosin V walking behavior.

To corroborate this finding, in the near future we are planning to employ native mass spectrometry in collaboration with Dr. C. Uetrecht (HPI Hamburg). This technique allows to unravel the stoichiometry of a native protein complex, and we are aiming to use this approach to test whether the binding stoichiometry of caldendrin to the myosin heavy chain is 1:1 or higher, and whether caldendrin can displace one or more CaM from myosin. If the latter holds true, this would be a strong additional indication for caldendrin being a negative regulator of myosin motor activity. Further, to gain a more direct judgement of how caldendrin affects myosin activity in the cellular context, we are going to

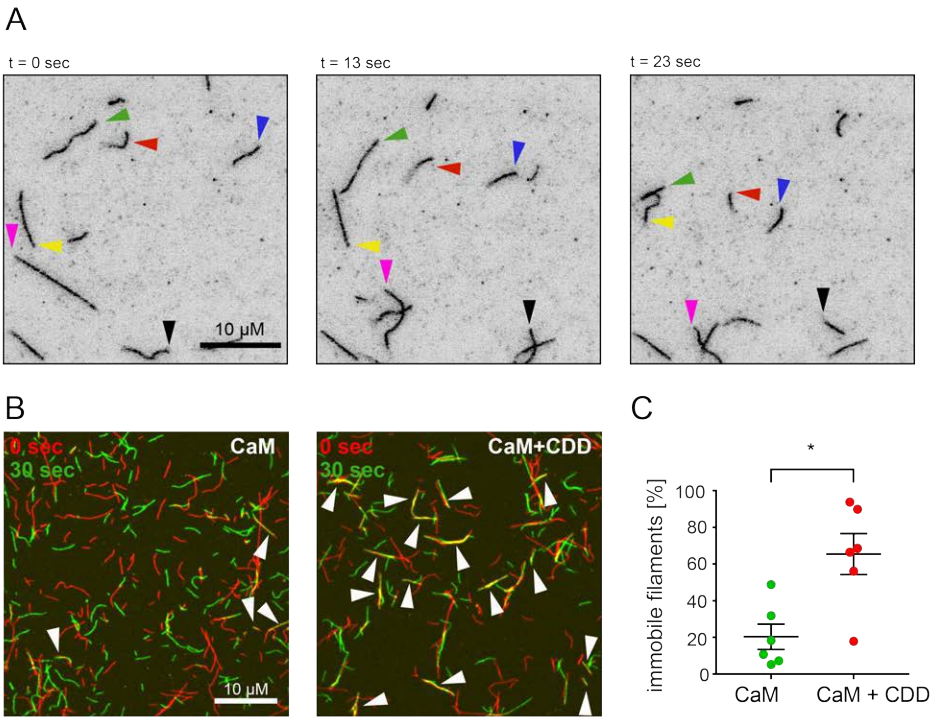

Figure 40. Analysis of the gliding assay. (A) Example images from time-lapse microscopy observing the movement of labeled actin filaments in the myosin Va gliding assay. Colored arrows follow the movement of individual filaments over time. **(B)** Analysis of myosin V activity in different experimental conditions. The first frame (0 sec, red) and 30th frame (30 sec, green) of a microscopy timelapse were overlayed to visualize immobile filaments (yellow). Left: Gliding assay in the presence of 30 µM CaM. Right: Gliding assay in the presence of 30 µM CaM and 5 µM CDD. Scale bar = 10 µm. **(C)** Quantification of immobile filaments in presence / absence of CDD as shown in (B). Wilcoxon matched pairs test. * p = 0.0313. n = 6 independent experiments with 12 flow channels analyzed.

employ a similar assay as described in (Kapitein *et al*, 2013; van Bergeijk *et al*, 2015). Here, the authors used a constitutively active kinesin-peroxisome construct similar to the one described in Figure 15, and added the option to additionally recruit a constitutively active myosin V (lacking the GTD) to the same organelle. This is made possible either through rapamycin-induced dimerization of the FRB-FKPB domains, or via light-inducible dimerization of the engineered LOV-ePDZ domain pair (Kapitein *et al*, 2013; van Bergeijk *et al*, 2015). It has been shown that in this scenario, firstly, myosin V is stronger than the coupled kinesin motor, and can take over the organelle, i.e. force it to brake. Secondly, with constitutively active myosin V coupled to the peroxisome, slow, actin-based movement can be observed that is carried out by the myosin motor. We are planning to use this system as a readout for myosin V activity in the presence or absence of caldendrin. I have already established a COS7 cell line stably expressing caldendrin, which we will use as a model to carry out this experiment.

Finally, if caldendrin is indeed used as a calcium-dependent regulator of myosin V in hippocampal neurons, we expect to see an effect on myosin V dependent transport processes in caldendrin knock-out neurons. Through our collaborator Dr. M. Kreutz (LIN Magdeburg) we have access to primary hippocampal cultures of caldendrin knock-out mice (Mikhaylova *et al*, 2018). We are planning to use those cultures to assess trafficking of AMPA-receptors in Rab11-positive vesicles, which are a known cargo of neuronal myosin V (Wang *et al*, 2008), in a caldendrin-deficient background. Those future experiments, together with the data presented here, should give us a comprehensive insight into the role of caldendrin in myosin V-dependent dendritic cargo trafficking.

Final conclusions

According to the current consensus, the flexibility and dynamics of neuronal networks is the basis of complex cognitive abilities, such as learning and memory. Forming and re-forming of those networks happens at the level of synaptic contacts, which are constantly exchanged and remodeled. An underlying necessity for this continuous flux is a functioning intra-cellular trafficking machinery, which I have further characterized in this thesis.

I and my colleagues were able to show that dendritic actin patches play an active role in organelle positioning, and that this function at least partly relies on the activity of the myosin V motor protein. Further, we showed that this motor protein is involved in the establishment and / or maintenance of the SA organelle, which plays a role in the basic process of learning and memory. We characterized turnover rates of both actin patches and synaptopodin clusters in different micro-domains (spine-associated vs. localized inside the dendritic shaft), and in both cases found considerable variance, which indicates an underlying functional difference. Based on this we hypothesize that both structures might be differentially affected by calcium-signaling depending on their location, i.e. their proximity to an active synapse. Regarding the role of calcium signaling, we described a novel calcium-dependent interactor of myosin V, the protein caldendrin. We provided initial evidence that caldendrin can act as an inhibitor of myosin V in high calcium environments, which makes it a candidate for the activity-dependent regulation of synaptic cargo transport. Finally, we proposed a future direction to pin-point the role of caldendrin in the neuronal environment.

Material and Methods

Animals and neuronal cell culture

Animals (Chapter 1 & 2)

Wistar rats Crl:WI(Han) (Charles River) and Wistar Unilever HsdCpb:WU (Envigo) rats were used in this study. Sacrificing of pregnant rats (E18) for primary hippocampal cultures and for biochemistry were carried out in accordance with the European Communities Council Directive (20110/63/EU) and with the Animal Welfare Law of the Federal Republic of Germany (Tierschutzgesetz der Bundesrepublik Deutschland, TierSchG) and with the approval of local authorities of the city-state Hamburg (Behörde für Gesundheit und Verbraucherschutz, Fachbereich Veterinärwesen, from 21.04.2015) and the animal care committee of the University Medical Center Hamburg-Eppendorf. The mice used in this study were bred and maintained in the animal facility of the Center of Molecular Neurobiology of Hamburg (ZMNH), Hamburg, Germany. Snell's waltzer mice carrying a spontaneously arisen ~1.0 kb genomic deletion in Myo6 were obtained from The Jackson Laboratory (B6 x STOCK Tyrc-ch Bmp5se +/+ Myo6sv/J; stock no. 000578) and were repeatedly backcrossed to C57BL/6J to obtain Myo6sv/+ mice carrying the Snell's waltzer allele but lacking the Tyrc-ch and Bmp5se alleles (Avraham et al., 1995).

Primary neuronal culture and transfections (Chapter 1 & 2)

Primary hippocampal rat cultures were essentially prepared as described previously (Kapitein et al., 2010). In brief, hippocampi were dissected from E18 embryos, treated with trypsin (0.25 %, Thermo Fisher Scientific) for 10 min at 37°C, physically dissociated by pipetting through a syringe, and plated on poly-L-lysine (*Sigma-Aldrich*, #P2636) coated glass coverslips (18mm) at a density of 40000-60000 cells per 1ml on in DMEM (*Gibco,* #41966-029) supplemented with 10 % fetal calf serum (*Gibco*, 10270) and antibiotics (*Thermo Fisher Scientific,* #15140122). After 1 h, plating medium was replaced by BrainPhys neuronal medium supplemented with SM1 (*Stem Cell kit,* #5792) and 0.5 mM glutamine (*Thermo Fisher Scientific,* #25030024). Cells were grown in an incubator at 37 °C, 5 % CO_2 and 95 % humidity.

Primary hippocampal rat cultures were transfected with lipofectamine 2000 (Thermo Fisher Scientific) according to the manufacturer's instructions. For co-transfection of plasmids the ratios of different constructs were optimized per combination, and optionally by addition of an empty vector (pcDNA3.1), to tune expression levels. Before transfection the original neuronal medium was removed. Neurons were transfected in BrainPhys medium, optionally supplemented with glutamine, but lacking SM1. Transfection medium was added for 45 min – 1.5 h. After transfection, the medium was exchanged back to the original BrainPhys containing SM1. Experiments on transfected neurons were performed 1 day after transfection.

Primary hippocampal mouse cultures from Myo6sv/sv and Myo6+/+ mice were prepared as described (Spilker et al., 2016). Briefly, hippocampi were dissected from male and female P0 Myo6sv/sv and Myo6+/+ mice and cells were dissociated after 10 min treatment with trypsin at 37 °C. Neurons were plated on glass dishes coated with poly-L-lysine (Sigma-Aldrich) at a density of 30.000 cells per well in a 12 well plate) in DMEM medium (Gibco) supplemented with 8 % FCS, 1% penicillin/streptomycin. Following attachment, mouse cultures were kept in Neurobasal medium (Gibco) supplemented with 2

mM glutamine, 1 % penicillin/streptomycin and 1X B27 supplement (Gibco), at 37 °C, 5 % CO2 and 95 % humidity.

Virus production and transduction

Production of AAV and infection of primary hippocampal neurons (Chapter 2)

Adeno-associated viruses were produced at the Vector Facility of the University Medical Center Hamburg-Eppendorf (UKE). pAAV-hSyn1-mRuby2 (Addgene 99126) and pAAV-hSyn1-GFP-synaptopodin (this study) were respectively packaged by pE2/rh10 and p5E/9 (Julie C. Johnston, University of Pennsylvania, USA) and pHelper (CellBiolabs). For infection with AAV, the viruses were added directly into the culture medium at final concentrations between 1011-109 vg/ml. pSyn-GFP-Synaptopodin AAV9 was added to the culture at DIV10, mRuby2 AAVrh10 was added on DIV14, and cells were imaged on DIV17.

Cell lines

Culture, transfection and harvest of HEK293 cells (Chapter 2 & 3)

HEK293T cells (from Mikhaylova et al., 2018) were maintained in full medium consisting of Dulbecco's modified Eagle's medium (DMEM; GIBCO, Thermo Fisher) supplemented with 10 % fetal calf serum (FCS), 1 x penicillin/streptomycin and 2 mM glutamine at 37 °C, 5 % CO2 and 95 % humidity. For the expression of biotinylated proteins, HEK293T cells were grown in full medium made with a 50 % DMEM, 50 % Ham's F-10 Nutrient Mix (GIBCO, Thermo Fisher) mixture. All transfections were done using MaxPEI 25K (Polysciences) in a 3:1 MaxPEI:DNA ratio according to the manufacturer's instructions. Transfected HEK cells were harvested 18-24 hours after transfection. The cells were washed 1 x in cold TBS, resuspended in 2 ml TBS and pelleted for 3 min at 1000g. The cell pellet was lysed in in 500 µl extraction buffer (20 mM Tris pH 8, 150 mM NaCl, 1% Triton-X-100, 5 mM $MgCl_2$, complete protease inhibitor cocktail (Roche)), kept on ice for 30 min and centrifuged for 15 min at 14000 x g. The supernatant (cleared lysate) was then further used for experiments.

Co-Immunoprecipitations and pull-downs

Pull-down for western blot and mass spec analysis (Chapter 2 & 3)

HEK293T cells were co-transfected with HA-BirA and either Synaptopodin-pEGFP-bio, Caldendrin-pEGFP-bio, or pEGFP-bio (control vector) and harvested on the next day as described above. Magnetic Streptavidin M-280 Dynabeads (Invitrogen) were washed 3 x in washing buffer (20 mM Tris pH 8, 150 mM KCl, 0.1 % Triton-X 100), blocked in 3 % chicken egg albumin (Sigma) for 40 min at RT, and again washed 3 x in washing buffer. The cleared cell lysate was added to the blocked beads and incubated at 4 °C on a rotator overnight. After the incubation period, the beads were washed 2 x with low salt washing buffer (100 mM KCl), 2 x in high salt washing buffer (500 mM KCl) and again 2 x in low salt washing buffer. For preparation of whole rat brain extract, 9 ml lysis buffer (50mM Tris HCl pH 7.4, 150 mM NaCl, 0.1 % SDS, 0.2 % NP-40, complete protease inhibitor cocktail (Roche)) were added per 1 g of tissue weight, and the tissue was lysed using a Dounce homogenizer. The lysate was cleared first for 15 min at 1000 x g, and the supernatant was again centrifuged for 20 min at 15000 g to obtain the final

lysate. The washed beads were then combined with 1 ml of the cleared rat brain lysate and incubated for 1 h at 4 °C on a rotator. In the case of Caldendrin-pEGFP-bio and the pEGFP-bio control, the beads were divided into 2 x samples, and incubated with rat brain lysate that was either substituted with 2 mM EGTA or with 0.5 mM $CaCl_2$ and 1 mM $MgCl_2$. After the incubation period, the beads were washed 5 x in washing buffer and resuspended in Bolt LDS sample buffer (Invitrogen) for subsequent SDS-PAGE and mass-spectrometry or western blot analysis. For mass-spectrometric analysis, the samples were separated on a commercial Bolt Bis-Tris Plus Gel (Invitrogen) and the intact gel was sent to Erasmus MC Proteomics Center, Rotterdam, for mass spectrometry analysis (see below).

Co-immunoprecipitation from HEK cells (Chapter 3)

HEK293T cells were transfected with the respective GFP-tagged myosin constructs and either with tagRFP-tagged caldendrin or tagRFP as a control, and harvested as described above. 45 µl of the cleared lysate were taken as an "input" sample. The remaining SN was split into 2 x 200 µl, distributed into separate tubes and substituted with either 2 mM EGTA or 0.5 mM $CaCl_2$ and 1 mM $MgCl_2$. GFP-trap beads (Chromotek) were washed 2 x in extraction buffer and an equivalent of 7 µl slurry was added to the tubes containing the cell lysates. The beads were then incubated on a rotor at 4°C for 2 – 4 hours. After the incubation period, the beads were washed 3 x in washing buffer (20 mM Tris, 150 mM NaCl, 0.5 % Triton-X-100, complete protease inhibitor cocktail (Roche)) that was either substituted with 2 mM EGTA or 0.5 mM $CaCl_2$ and 1 mM $MgCl_2$. The beads were then taken up in 30 µl SDS sample-buffer (250 mM Tris-HCl, pH 6.8, 8 % (w/v) SDS, 40 % (v/v) glycerol, 5 % (v/v) β-mercaptoethanol, 0.004% bromophenol blue, pH 6.8) for SDS-PAGE.

Co-immunoprecipitation of purified myosin with recombinant caldendrin (Chapter 3)

The purified caldendrin calcium binding mutant was a gift from R. Raman, LIN Magdeburg. HEK293T cells were transfected with the respective GFP-tagged myosin constructs and either with tagRFP-tagged caldendrin or tagRFP as a control, and harvested as described above. The cleared lysate was incubated with an equivalent of 7 µl GFP-trap slurry (Chromotek) for 6 h at 4°C on a rotor, then the beads were washed 3 x with washing buffer (20 mM Tris, 150 mM NaCl, 0.5 % Triton-X-100, complete protease inhibitor cocktail (Roche)), blocked with washing buffer supplemented with 5 % BSA, and then divided into 4 equal samples. Each one was incubated with washing buffer supplemented with 100 nM of either purified, recombinant wt caldendrin, or a caldendrin calcium binding mutant (D243A, D280A, Mikhaylova *et al.* 2018), in the presence or absence of 2 mM EGTA or 100 µM CaCl2. After the incubation period, the beads were washed 3 x in washing buffer (20 mM Tris, 150 mM NaCl, 0.5 % Triton-X-100, complete protease inhibitor cocktail (Roche)) that was either substituted with 2 mM EGTA or 100 µM CaCl2. The beads were then taken up in 30 µl SDS sample-buffer (250 mM Tris-HCl, pH 6.8, 8 % (w/v) SDS, 40 % (v/v) glycerol, 5 % (v/v) β-mercaptoethanol, 0.004% bromophenol blue, pH 6.8) for SDS-PAGE.

<u>Constructs and cloning</u> (Chapters 1, 2, 3)

For cloning of the PEX3-EmeraldGFP-KIF17 construct, the peroxisome targeting sequence of PEX3 (Accession NM_003630; previously described by (Kapitein et al, 2010)) was amplified via PCR and inserted into an empty pAAV2 vector using AgeI and HindIII restriction sites. GFP (mEmerald variant) was amplified via PCR and inserted behind the PEX3 via HindIII and BamHI restriction sites. The P2A

sequence including a 3' KpnI restriction site was amplified via PCR and inserted behind the GFP in the BamHI-cut vector using the Cold Fusion Cloning Kit (SBI, MC010B-1). The constitutively active KIF17 construct (β-actin KIF17(1-547)-FRB) was used as a PCR template and is a kind gift from Casper Hoogenraad and was described previously (Kapitein et al, 2013). KIF17 sequence was inserted behind the P2A sequence via KpnI and NheI restriction sites. The GFP-nanobody including the GSG9-linker (GSG9-vhhGFP4) was described before (Caussinus et al, 2011; Katrukha et al, 2017). The whole sequence including a 3' NheI restriction site was amplified via PCR and inserted into the NheI-digested vector using the Cold Fusion Cloning Kit (SBI, MC010B-1).

To produce the pEGFP-bio-synaptopodin construct, synaptopodin (mouse isoform 3, identifier: Q8CC35-3) was subcloned from a pEGFP-Synaptopodin plasmid (Asanuma et al., 2005) into pEGFP-C1-bio (kind gift from Anna Akhmanova) with SacII and SalI restriction. For cloning of the hSyn1-GFP-synaptopodin construct, GFP-synaptopodin was amplified via PCR, pAAV-hSyn1-mRuby2 was digested with EcoR1 and HindIII to remove mRuby2. GFP-synaptopodin was inserted into the digested plasmid using homologous recombination (Jacobus and Gross, 2015). To produce the MyoVI DN construct, the Syn-GFP-synaptopodin vector was digested with HindIII and NdeI to remove synaptopodin, and the C-terminal domain of mouse myosin VI (bp 3177-3789; NCBI reference sequence: NM_001039546.2) was amplified via PCR and cloned into the backbone (Aschenbrenner et al., 2003).

The TwinStrep-GFP-Myosin constructs were produced by amplifying the TwinStrep-tag sequence by PCR from a TwinStrep-mCherry empty vector template (gift from A. Aher, Utrecht University), and pasting it into the pmEmerald/MyosinV vector using the NheI cutting site. GFP-myosin fragments for co-immunoprecipitations were amplified from the pmEmerald/MyosinV template by PCR. The whole Myosin V sequence was cut from the vector using the NotI cutting site, and the PCR amplified fragments were re-inserted into the vector using sequence overlap and the Cold Fusion Cloning Kit (SBI, MC010B-1).

The caldendrin-tagRFP constructs were made by amplifying full length or caldendrin fragments from the pcDNA3.1/caldendrin vector and pasting them into the tagRFP-N plasmid (Evrogen, #FP142) using EcoRi and BamHI restriction and ligation.

pET/Calmodulin construct: Untagged human calmodulin was amplified from addgene plasmid #47603 via PCR and cloned into an empty pET/T7 expression vector (gift from H.J. Kreienkamp, UKE Hamburg) using NdeI and HindIII restriction and ligation.

All constructs were verified by sequencing. A complete list of expression constructs used in this study is provided on page 75.

Microscopy Imaging and Analysis

Immunocytochemistry (Chapter 1 & 2)

Cells were fixed in 4 % Roti-Histofix (Carl Roth), 4 % sucrose in PBS for 10 min at RT and washed three times with phosphate buffered saline (PBS), before they were permeabilized in 0.2 % Triton X-100 in PBS for 10 min. The cells were then washed 3 x in PBS and blocked for 45 min at RT with blocking buffer (BB / 10 % horse serum, 0.1 % Triton X-100 in PBS).. Incubation with primary antibodies was performed in BB at 4 °C overnight. After 3 x washing in PBS, cells were incubated with corresponding secondary

antibodies in BB for 1 h at RT. If the staining included phalloidin, an additional step was added where the coverslips were incubated with phalloidin-647N (1:40) overnight at 4 °C. Finally, coverslips were washed 3-5 x 10 min in PBS and mounted on microscope slides with mowiol. Mowiol was prepared according to the manufacturer's protocol (9.6 g mowiol 4-88 (*Carl-Roth*), 24.0 g glycerine, 24 ml H_2O, 48 ml 0.2 M Tris pH 8.5, including 2.5 g Dabco, (*Sigma-Aldrich* D27802).

STED Imaging (Chapter 1 & 2)

Confocal and STED images of phalloidin (Atto647N), MAP2 (Alexa488), cortactin (Abberior Star 580) or synaptopodin (Abberior Star 580) were acquired on a Leica TCS SP8-3X gated STED microscope equipped with a pulsed 775 nm depletion laser and a pulsed white light laser (WLL) for excitation. Samples were imaged with a 100x objective (Leica, HC APO CS2 100x/1.40 oil).

Fluorescence of the respective channel was excited by the WLL at 650 nm (STED and confocal), 488 nm (confocal mode) and 561 nm (STED and confocal), respectively. STED was attained with the 775 nm laser for Atto647N/Abberior 580 and with the 592 nm laser for Alexa Fluor 488. Emission spectra were detected at 660-730 nm for Atto647N, 580-620 nm for Abberior Star 580, and 500-530 nm for Alexa Fluor 488. The detector time gates were set to 0.5-6 ns for Abberior Star 580/Atto647N and 1.5 ns-6 ns for Alexa Fluor 488. Images were taken as single planes of with 18 nm2 pixel size, with 1024x1024 pixels, optical zoom factor 5 (for oil: x/y 22.73 nm), 600 lines per second and 16 x line averaging. Corresponding confocal channels had the same setting as STED channels, except the excitation power was reduced and the detection time gates were set to 300 ps - 6 ns for all channels.

Analysis of STED data (Chapter 2)

The number, size and integrated fluorescence intensity of synaptopodin patches, the presence of F-actin and association with homer1 or MAP2 were analyzed using Fiji. 2D STED images of dendritic stretches were used for analysis. ROIs around synaptopodin patches were drawn manually in the synaptopodin channel and subsequently, integrated intensities within these ROIs were measured in the F-actin channel. Co-localization of synaptopodin with homer1 or MAP2 was scored manually by the presence or absence of a signal in the respective channels inside of the synaptopodin ROI. Differentiation between spine- and shaft-associated was based on the proximity to clearly discernable dendritic spines (not further than 0.5 µm from the spine base).

Fixed cell imaging: confocal microscopy (Chapter 2)

Z-stack images of fixed primary hippocampal neurons and fixed synaptosomal preparations were acquired on Leica TCS SP8 and Leica TCS SP5 confocal microscopes using a 63.0 x 1.40 oil objective using 488 nm, 568 nm and 633 nm excitation lasers. The pixel size was set to 90 nm and z-steps varied between 250-350 nm. For the shown representative confocal images, a Gaussian filter (radius 0.5 px) was applied in ImageJ to reduce the visible background noise.

Live cell imaging: wide field, TIRF and spinning disc microscopy (Chapter 1 & 2)

Live cell wide-field and TIRF microscopy was performed with a Nikon Eclipse Ti-E controlled by VisiView software (*VisitronSystems*). Samples were kept in focus with the built-in Nikon perfect focus system.

Fluorophores were excited by 488 nm, 561 nm, and 639 nm laser lines, coupled to the microscope via an optic fiber. HILO and TIRF illuminations were obtained with an ILAS2 (*Gataca-systems*) spinning-TIRF system. Samples were imaged with a 100x TIRF objective (*Nikon*, ApoTIRF 100x/1.49 oil). Emission light was collected through a quad-band filter (*Chroma*, 405/488/561/640) followed by a filter wheel with filters for GFP (*Chroma,* 525/50m), RFP (*Chroma*, 595/50m), and Cy5 (*Chroma,* 700/75m). Multi-channel images were acquired sequentially with an Orca flash 4.0LT CMOS camera (*Hamamatsu*). Images were acquired at 2- 5 frames per second or at specified intervals.

Spinning-disc confocal was performed with a Nikon Eclipse Ti-E controlled by VisiView software. Samples were kept in focus with the built-in Nikon perfect focus system. The system was equipped with a 100x TIRF objective (*Nikon*, ApoTIRF 100x/1.49 oil), and 488 nm, 561 nm, and 639 nm excitation laser. Lasers were coupled to a CSU-X1 spinning disk unit via a single-mode fiber. Emission was collected through a quad band filter (*Chroma*, ZET 405/488/561/647m) on an Orca flash 4.0LT CMOS camera (*Hamamatsu*). Images were acquired sequentially with specified intervals.

At all systems, live neurons were imaged in regular culture medium. Coverslips were placed in either an attofluor cell chamber (*Thermo Fisher Scientific*) or a Ludin chamber (*Life Imaging Services*). Correct temperature (37 °C), CO_2 (5 %) and humidity (90 %) were maintained with a top stage incubator and an additional objective heater (*Okolab*).

If pharmacological treatment was performed during live imaging, the respective drug was added manually to the culture medium and incubated for the indicated time spans in the top stage incubator.

Kymograph analysis (Chapter 1)

Kymographs were constructed using the *KymographClear* or *KymoResliceWide* plugin for Fiji (*NIH*) . Non-overlapping dendritic stretches of 30 – 80 µm length were traced, using the *segmented line* tool. Maximum 3 dendrites were taken from the same neuron. Line thickness was chosen to cover the dendritic shaft, but to omit spines. Trajectories in the kymographs were traced by hand using the *straight line* tool. Trajectories with a uniform speed (= slope) were considered one "event", changes in speed (= slope) or stopping events (= vertical lines) were traced as separate events. Slope and length of each event were used to calculate instant velocity, instant run length, and pausing time. In general, all lysosomes were analyzed. For experiments with the PEX3-Kif17 construct only peroxisomes that showed at least one moving behavior were analyzed. Non-moving peroxisomes could be due to inefficient coupling and were therefore excluded.

Calculation of the directional net flux (Chapter 1)

The directional net flux F is a measure for the summed transport direction of vesicles.

$$F = [\Sigma(r_{anterograde}) - \Sigma(r_{retrograde})] / [\Sigma(r_{anterograde}) + \Sigma(r_{retrograde})]$$

with r being run length

Outcomes range between -1 (exclusive retrograde movement) and 1 (exclusive anterograde movement), being 0 when anterograde matches retrograde movement.

Cumulative pausing time (Chapter 1)

As a measure for overall pausing behavior, the cumulative pausing time was calculated. All pausing times of all vesicles within one analyzed dendritic segment were summed over the complete imaging period before and after treatment (identical time) and normalized to the control group (before treatment) to obtain an n of 1.

Lysosome count (Chapter 1)

To compare the number of mobile vs. stationary LAMP1-positive organelles (lysosomes) in different treatment conditions, the same time-lapse movies and ROIs selected for kymograph analysis were used. All visible lysosomes in only the first frame of the time-lapse movie were counted manually (=total lysosomes). The number of stationary lysosomes is defined as those that stayed immobile during the whole imaging period (3 min), as visible in the kymograph. Mobile lysosomes are calculated as total lysosomes-stationary lysosomes.

Analysis of actin patches (Chapter 1)

The density of actin patches, size and mean fluorescence intensity of F-actin within given patch, presence of cortactin and association with homer1 were analyzed using Fiji. 2D STED images of dendritic stretches, 13 - 32 µm in length, were used for analysis. ROIs were drawn manually in the phalloidin channel (unprocessed STED) and subsequently; size, integrated and mean intensity and cortactin integrated density were measured in the unprocessed STED channels. Differentiation between spine and shaft associated was based on the proximity to clearly detectable dendritic spines (not further than 0.5 µm from the spine base). PSD positive or negative patches were defined by direct association with homer1.

Analysis and quantification synaptopodin co-localization with homer1 or the ER (Chapter 2)

All of the following quantifications were done using confocal Z-stack imaging of fixed and stained neurons. Z-stacks of dendrites were projected into one plane using the Z projection function of Fiji/ImageJ (Max Intensity). Per cell, 1 - 4 dendritic segments of approximately 40-60 µm length were selected and used for manual quantification as outlined below. The detailed information on the number of dendrites and cells is indicated in the corresponding figure legends.

For initial quantification of density and localization of synaptopodin puncta during neuronal development (Figure 2A), untreated hippocampal neurons were fixed and stained against synaptopodin and MAP2 (dendritic marker). The number of synaptopodin puncta that were localized inside the dendrite (as judged by MAP2 staining) or outside the dendrite (interpreted as filopodia- or spine-localization) were counted.

For quantification of synaptopodin localization with respect to developing synapses, untreated hippocampal neurons were fixed and stained against synaptopodin, homer1 (synaptic marker) and phalloidin (F-actin marker). Spines were defined as protrusions from the main dendrite that were positive for homer1.

To assess the effects of myosin V and myosin VI, dominant-negative or control constructs (mCerulean or YFP) were transfected on DIV16, cells were fixed on DIV17 and stained against synaptopodin and

homer1 (Figure 4, S4). Spines were defined as protrusions from the main dendrite that were positive for homer1.

Similarly, to quantify spinous localization of synaptopodin and the ER (Figure 5), myosin dominant-negative or control constructs were co-transfected with an ER-DsRed-marker on DIV16, cells were fixed on DIV17 and stained with anti-synaptopodin and anti-RFP. Here, spines were defined as spine-shaped protrusions from the main dendrite as visible in the cell fill.

Fluorescence Recovery after Photobleaching (FRAP) (Chapter 2)

Primary hippocampal neurons were co-infected with two AAVs containing GFP-synaptopodin and mRuby2. mRuby2 was imaged with a 563 nm laser and the images were used to determine the localization of synaptopodin puncta. FRAP of GFP-synaptopodin was performed using a Nikon spinning disc confocal microscope. Time-lapse imaging of GFP-synaptopodin was done with a 488 nm laser and bleaching of selected puncta was achieved with a 405 nm laser. Images were acquired at 0.5 Hz for 300 s, starting with a 5 frames baseline before FRAP. FRAP analysis was done using the plug in Time Series Analyzer V3 of FIJI (NIH, Bethesda, MD, USA). ROIs were selected on the bleached ("frapped") synaptopodin puncta, on a non-bleached stretch of dendrite to account for bleaching during imaging (bleach control), and on a non-fluorescent region to account for background fluctuations. The integrated density values of those ROIs were measured, the background values were subtracted from the values of GFP-synaptopodin puncta, then GFP-synaptopodin was normalized to the bleach control and to the pre-bleach value (i.e. the pre-beach value was considered as 100 %).

<u>Data Representation</u>

Statistical Analysis (Chapters 1, 2, 3)

Statistical analysis was performed in Statistica 13 (*Dell Inc* RM 2-way ANOVA.) or Prism 6.05 (*GraphPad*; all other tests). Detailed specifications about the type of test, significance levels, n numbers, and biological replicates are provided in the figure legends. Experimental repeats and n numbers per experiment were chosen according to experience with effect size. Data are represented individually in dot blots or as mean ± SEM throughout the manuscript. The data were tested for normality using the D'Agostino-Pearson test (Prism) and accordingly subjected to parametric (t-test, ANOVA) or non-parametric tests (Mann-Whitney test, Kruskal-Wallis test) for significance. The analysis of the Myo6sv/sv and Myo6+/+ mice data was done blindly.

<u>Subcellular Fractionation</u>

Lysosomal enrichment and characterization (Chapter 1)

Enrichment of lysosomes was done using a Lysosome Enrichment Kit (*Thermo Fisher Scientific*, #89839) according to the manufacturer's instructions. In brief, approximately 100 mg of tissue from the cortex and hippocampus of an adult, female rat was homogenized in buffer provided by the kit, using a Dounce homogenizer and cleared at 500 x g for 10 min at 4 °C. The supernatant was supplemented with 15 % OptiPrep and loaded on top of an OptiPrep gradient (five layers with 30 %, 27 %, 23 %, 20 % and 17 % OptiPrep) in an ultracentrifuge tube. Centrifugation was carried out at 145.000 x g in a swinging bucket rotor for 2 h at 4 °C. After centrifugation, the lysosome enriched band (upper-most

band below the input) was removed and mixed with 3 volumes of PBS to decrease the concentration of the OptiPrep. The sample was centrifuged again at 18.000 x g for 30 min at 4 °C, the supernatant was removed and the lysosome pellet was either taken up in in sample buffer for SDS-PAGE and western blot, or resuspended in PBS, treated with 1:20.000 LysoTracker Red and then fixed for 1 h on ice with 4 % Roti-Histofix/4 % sucrose for immunostaining. For western blot analysis, lysosome samples were subjected to SDS-PAGE on a 4-20 % gradient gel and transferred to a PVDF membrane. The membrane was blocked (5 % milk in TBS + 0.1 % Tween-20) and stained with primary antibodies against myosin VI, myosin Va, dynein IC 1/2, and KIF5C, followed by HRP-coupled anti-mouse and anti-rabbit antibodies. The membranes were imaged on a ChemoCam imager (*Intas*). For immunostaining, coverslips were coated with poly-L-lysine (*Sigma-Aldrich*) for 4 h at RT and washed 5 times with milliQ H_2O. 10 µl droplets with fixed lysosomes were put on top of a parafilm surface, then coated coverslips were placed on the droplets face-down and incubated for 25 min at RT. Afterwards coverslips were flipped over and washed 2 times with PBS. The surface was then blocked for 45 min with blocking buffer, washed 3 x with PBS, and stained with primary antibody (in blocking buffer; mouse anti-lamp1, rabbit anti-myosin VI, rabbit anti-myosin Va) for 1 h at RT (or overnight at 4 °C), washed 3 x in PBS, and stained with secondary antibody diluted in blocking buffer for 45 min at RT, washed 3 x in PBS and mounted in mowiol on a microscopy slide.

Enrichment of peroxisomes from whole rat brain lysate (Chapter 1)

The whole brain of a female adult rat was homogenized in 10 ml homogenization buffer (0.32 M sucrose, 5 mM HEPES, pH7.4, Roche complete protease inhibitors) per 1 g of tissue, using a Dounce homogenizer at 900 rpm (12 strokes). Homogenate was centrifuged for 10 min at 1000 g at 4°C. Supernatant (S1) was removed and kept on ice, the pellet (P1) was resuspended in 10 ml / g homogenization buffer and homogenized again for 12 strokes at 900 rpm. The homogenate was centrifuged at 100 g for 10 min at 4°C. Supernatant (S1') was removed and combined with S1, pellet (P1') was discarded. The combined supernatants (S1+S1') were centrifuged at 12.000 g for 15 min at 4°C. Supernatant (S2) was removed and kept on ice, pellet (P2) was resuspended in 10 ml / g homogenization buffer and homogenized for 6 strokes at 900 rpm. The homogenate was centrifuged again at 12.000 g for 20 min at 4°C. Supernatant (S2') was removed and combined with S2, pellet (P2') was discarded. The combined supernatants (S2+S2') were centrifuged at 100.000 g for 1 h at 4°C. The resulting pellet (enriched in microsomes) was resuspended in 1 ml homogenization buffer and kept on ice. For western blot analysis, 200 µl of the microsome fraction were mixed with 200 µl 2 x SDS-sample buffer, separated on a 4 – 20 % SDS-polyacrylamide-gel and blotted on a PVC membrane. The membrane was stained with primary antibodies against myosin Va(rb), PMP70(ms), PEX14(rb), and β-actin(ms), followed by HRP-coupled anti-mouse and anti-rabbit antibodies. The membranes were imaged on a ChemoCam imager (*Intas*). For immuno-staining, 200 µl of the microsome fraction were fixed by adding 400 µl fixation buffer (4% Roti-Histofix, 4 % sucrose in PBS) and kept over night at 4°C. For immunostaining, coverslips were coated with poly-L-lysine (*Sigma-Aldrich*) for 4 h at RT and washed 5 times with milliQ H_2O. 10 µl droplets with fixed microsomes were put on top of a parafilm surface, then coated coverslips were placed on the droplets face-down and incubated for 45 min at RT. The coverslips were then washed for 3 x 5 min in PBS, blocked for 30 min in blocking buffer (10 % horse serum, 0.1 % Triton X-100 in PBS), and incubated over night with primary antibodes (Myosin Va(rb), Myosin VI(rb), PMP70(ms), PEX14(rb); 1:750 in blocking buffer) at 4°C. The coverslips were washed again for 3 x 10 min with PBS, stained for 1 h at RT with secondary antibodies (ms-alexa488,

rb-alexa 568; 1:500 in blocking buffer), washed for 3 x 10 min with PBS and mounted on microscopy slides in mowiol.

Synaptosome enrichment (Chapter 2)

The whole brain of an adult, female rat was homogenized in cold homogenization buffer (0.32 M sucrose, 5 mM HEPES, pH 7.4) in a ratio 1 g of tissue to 15 ml of buffer, using a Dounce homogenizer at 900 rpm. All steps were performed on ice or at 4°C. The homogenate was centrifuged for 10 min at 1000 x g, the supernatant (S1) was removed and kept on ice. The pellet was re-suspended in homogenization buffer and homogenized again in a Dounce homogenizer. After a second centrifugation step for 10 min at 1000 x g, the supernatant (S1') was combined with S1 and centrifuged for 15 min at 12.000 x g. The supernatant (S2) was removed, and the pellet was re-homogenized in homogenization buffer and centrifuged at 12.000 x g for 20 min. The resulting pellet (P2', enriched in synaptosomes and small vesicular organelles) was resuspended in homogenization buffer. For immunostaining, the sample was fixed by adding 2.7% Roti-Histofix (Carl Roth), 2.7% sucrose and incubated for 1 h at RT. Glass coverslips were coated with poly-L-lysine (Sigma-Aldrich) for 4 h at RT and washed 5 times with milliQ H2O. 10 µl droplets of the fixed microsome fraction were put on top of a parafilm surface, PLL-coated coverslips were placed on the droplets face-down and incubated for 25 min at RT. Then the coverslips were flipped and washed 3 x in PBS. Staining with antibodies against synaptopodin, shank3 and myosin V or VI was done as described under Immunocytochemistry. The samples were imaged using a Leica TCS SP5 confocal microscope.

<u>Western Blot</u> (Chapters 2 & 3)

For Western blot analysis, samples were either taken up in commercial Bolt LDS sample buffer (Invitrogen), or self-made SDS sample-buffer (250 mM Tris-HCl, pH 6.8, 8 % (w/v) SDS, 40 % (v/v) glycerol, 5 % (v/v) β-mercaptoethanol, 0.004% bromophenol blue, pH 6.8) as specified. In general, samples were run on 4 % - 20 % acrylamide gradient gels and blotted on PVDF membranes in blotting buffer (192 mM glycine, 0.1 % (w/v) SDS, 15 % (v/v) methanol, 25 mM Tris-base, pH 8.3). After blocking the membranes in 5 % skim milk in Tris-buffered saline (TBS, 20 mM Tris pH 7.4, 150 mM NaCl, 0.1 % Tween-20), membranes were incubated with primary antibodies diluted in TBS-A (TBS pH 7.4, 0.02 % sodium-azide) overnight at 4°C. Corresponding HRP-conjugated secondary antibodies or HRP-Strepdavidin were applied for 1.5 h at RT in 5 % skim milk in TBS. The membranes were imaged on a ChemoCam imager (Intas).

Western blot analysis of synaptopodin expression (Chapter 2)

At DIV5, DIV10, DIV15 and DIV21, cells were harvested by removing the medium and adding SDS sample buffer (250 mM Tris-HCl, pH 6.8, 8 % (w/v) SDS, 40 % (v/v) glycerol, 5 % (v/v) β-mercaptoethanol, 0.004% bromophenol blue, pH 6.8) directly to the well. In an initial western blot against β-actin, the intensity of the actin band in each sample was measured with the gel analyzer / plot lanes function of ImageJ. For the final western blot, the inputs were normalized to contain the same amount of β-actin as a loading control, and synaptopodin levels were detected using a synaptopodin antibody (Synaptic Systems #163002).

Mass spectrometry and data analysis

Sample preparation (Chapters 2 & 3)

Pull-down samples were separated on a commercial Bolt Bis-Tris Plus Gel (Invitrogen) and the intact gel was sent to Erasmus MC Proteomics Center, Rotterdam, for mass spectrometry analysis. SDS-PAGE gel lanes were cut into 1-mm slices using an automatic gel slicer. Per sample 8 to 9 slices were combined and subjected to in-gel reduction with dithiothreitol, alkylation with iodoacetamide and digestion with trypsin (Thermo Fisher Scientific, TPCK treated), essentially as described by (Wilm et al., 1996). Nanoflow LCMS/MS was performed on an EASY-nLC 1000 Liquid Chromatograph (Thermo Fisher Scientific) coupled to an Orbitrap Fusion™ Tribrid™ Mass Spectrometer (Thermo Fisher Scientific) operating in positive mode and equipped with a nanospray source. Peptide mixtures were trapped on a nanoACQUITY UPLC C18 column (100Å, 5 µm, 180 µm X 20 mm, Waters). Peptide separation was performed on a ReproSil C18 reversed phase column (Dr Maisch GmbH; 20 cm × 100 µm, packed in-house) using a linear gradient from 0 to 80% B (A = 0.1 % formic acid; B = 80% (v/v) acetonitrile, 0.1 % formic acid) in 60 min and at a constant flow rate of 500 nl/min. Mass spectra were acquired in continuum mode; fragmentation of the peptides was performed in data-dependent mode. Peak lists were automatically created from raw data files using the Mascot Distiller software (version 2.1; MatrixScience). The Mascot search algorithm (version 2.2, MatrixScience) was used for searching against a UniProt canonical database (release 2016_07, taxonomies Homo sapiens and Rattus norvegicus combined). The peptide tolerance was typically set to 10 ppm and the fragment ion tolerance to 0.8 Da. A maximum number of 2 missed cleavages by trypsin were allowed and carbamidomethylated cysteine and oxidized methionine were set as fixed and variable modifications, respectively. Quantitative analysis was done with MaxQuant software (version 1.5.4.1) using similar or standard settings and using the UniProt rat and human isoforms databases (both releases 2016_07).

Network analysis of potential (Chapters 2 & 3)

We selected the 50 proteins that had the highest unique peptide count in the synaptopodin or caldendrin pull-down (and where unique peptides were at least 2 x those found in the negative control) from the mass spectrometry analysis of synaptopodin / caldendrin interactors for the network analysis using the “Multiple Proteins” function of the online STRING database (http://string-db.org; Szklarczyk et al., 2015). The parameters changed from the default settings were as follows: Network edges: “Confidence” (line thickness indicates the strength of data support). Active interaction sources: “Experiments” and “Databases”. Selected network statistics / Functional enrichments: Biological Process (GO).

Protein Purification

Calmodulin purification from E. coli (Chapter 3)

A single colony of *E.coli* BL21 transformed with the pET/CaM construct was used to inoculate a 5-ml LB pre-culture. After overnight growth at 30 °C, 2 ml of the pre-culture was used to inoculate a 1-l culture in LB medium and grown at 30 °C for 4 h until the absorbance reached 0.5 at 600 nm. Expression of the plasmid was induced by adding 500 µM IPTG, the culture was put at 16°C and grown for about 16 h. Cells were then harvested at 5000 g for 5 min. The pellet was resuspended in 40 ml lysis buffer (25 mM Tris, 5 mM CaCl2, 2 mM MgCl2, 200 µg/ml lysozyme, 2 µg/ml DNAse) and put on a rotor for 10 min at RT. The lysate was then put on ice and sonicated for 2 x 3 min with a 7 mm sonicator at 30 % with cycle set to 3 x 10 %. After centrifugation at 40.000 g for 35 min, the lysate was passed over a 5 ml HiTrap Phenyl FF (LS) column using the ÅKTA Start chromatography system. Flow rate was set to 3 ml/min and pressure to 0.03 mPa. Bound calmodulin was eluted with 25 mM Tris, 10 mM EDTA buffer. Binding and elution was performed 3 x. In between, the column was washed with 25 mM Tris, 5 mM CaCl2 buffer. The eluate was captured in 4 ml fractions, with the peak appearing in fraction 2. Fraction 2 from all 3 elution steps was pooled and dialysed O/N at 4°C against 2 l of 25 mM Tris, 50 mM NaCl, 2 mM CaCl2 buffer. After the dialysis, the eluate was up-concentrated to 3 ml using an Amicon Ultra 3000 MW centrifugal filter unit (Merck). Concentration assessment with a NanoDrop (ε = 2980, kDa = 17) resulted in an estimated concentration of 15 mg/ml.

Caldendrin purification (Chapter 3)

A single colony of *E.coli* BL21 transformed with the pMXB10/Caldendrin-Intein-tagged construct was used to inoculate a 20 ml LB pre-culture. After overnight growth at 37 °C, the whole pre-culture was used to inoculate a 1 l culture in LB medium and grown at 37 °C for 2 h until the absorbance reached 0.5 at 600 nm. Expression of the plasmid was induced by adding 400 µM IPTG, the culture was put at 18 °C and grown O/N for about 16 h. Cells were then harvested at 5000 g for 5 min. The pellet was resuspended in 40 ml intein buffer (20 mM Tris-HCl pH 8.5, 500 mM NaCl, 1 mM EDTA, 0.5 mM TCEP (tris(2-carboxyethyl)phosphine), 1 x complete protease inhibitors). Then approx. 20 mg lysozyme (100.000 U/mg) was added and after 30 min incubation on ice the lysate was sonicated for 3 x 10 sec with a 5 mm sonicator at 30 % and cycle set to 80 %. After the sonication, 50 U/ml benzonase (Santa Cruz) was added, the lysate was incubated on ice for 1 h and then centrifuged at 20.000 g for 25 min. The supernatant containing the protein was incubated with 5 ml chitin resin on a rotor at 4 °C for 2 h. The protein-bound resin was then put in a column, washed with 100 ml intein buffer and with 15 ml elution buffer (intein buffer supplemented with 50 mM DTT), before incubation with 7 ml elution buffer O/N at 4 °C. The eluate was collected approx. 16 h later, and dialysed for 2 h against 1 l intein buffer without TCEP, after 2 h the dialysis buffer was exchanged and left again O/N at 4 °C. After dialysis, the eluate was diluted with 8 ml of 100 mM Tris pH 8, up-concentrated in a Amicon Ultra 10.000 MW centrifugal filter unit (Merck) to 2 ml, diluted with 1.1 ml of 100 mM Tris pH 8, again up-concentrated to 1.5 ml, and then ultra-centrifuged at 100.000 g for 15 min. Finally, the eluted protein was aliquoted, flash-frozen in liquid nitrogen and stored at -80°C. Yield ~ 1.5 mg from 1 l culture.

Myosin V purification (Chapter 3)

HEK293T cells were transfected with the TwinStrep-pmEmerald/MyosinV construct and harvested as described above. The cell lysate was supplemented with 2 mM EGTA and incubated on a rotor at 4°C

with 40 µl magnetic StrepTactin beads (iba life sciences) for 1 h. The beads were then washed 2 x with washing buffer (20 mM Tris, 150 mM NaCl, 0.5 % Triton-X-100, 2 mM EGTA, complete protease inhibitor cocktail (Roche)), and finally incubated with BXT elution buffer (100 mM Tris ph8, 150 mM NaCl, 1 mM EDTA, 100 mM biotin) for 10 min on ice. After the incubation period, the beads were centrifuged for 2 min at 5.000 g, and the supernatant containing the protein was used for further experiments. Yield ~ 1.5 µg protein from 10 cm HEK cell dish.

In vitro Gliding Assay

The setup for the gliding assay was based on (Preciado López *et al*, 2014).

Cleaning and coating of coverslips (Chapter 3)

Coverslips and microscope slides were cleaned using a "base piranha" solution: Milli-Q water, 30 % hydrogen peroxide and 30 % ammonium hydroxide were mixed in a 5:1:1 volume ratio and heated to 70°C in a glass beaker. Coverslips and microscope slides were placed in the solution using a slide-holder made of Teflon, and incubated for 10 min at 70°C. After the incubation period they were removed and rinsed 5 x with Milli-Q water, before they were dried in an oven at 50 °C. Flow-channels with a width of approx. 4 mm were assembled from the dried microscope slides and coverslips using Para-film as a spacer. The flow channels were coated with PLL-PEG-biotin (SuSoS AG), neutravidin (Sigma) and κ-casein (Sigma) in the following way: 0.1 mg/ml PLL-PEG-biotin in PEM80 buffer (80 mM Pipes pH 6.8, 1 mM EGTA, 4 mM MgCl2) was added into the flow channels and incubated for 1 h at room temperature. The channels were rinsed with 30 µl PEM80 buffer, and 0.25 mg/ml neutravidin in PEM80 was added. After 10 min incubation, the channels were again rinsed with 30 µl PEM80 and 0.5 mg/ml κ-casein in PEM80 was added. After 7-10 min incubation, the channels were rinsed with 50 µl PEM80 and kept in a high humidity chamber until further use.

Preparation of F-actin for gliding assay (Chapter 3)

G-actin (Tebu bio) was stored in G-buffer (20 mM Tris-HCl pH 7.4, 20 µM CaCl2, 200 µM ATP, 1 mM DTT) in 25 µM aliquots at -80°C. Aliquots were slowly thawed on ice O/N the day before they were used. Immediately before use, they were diluted 1:1 in G-buffer, centrifuged at 120.000 g for 5 min at 4°C, and the supernatant was used for experiments. To prepare labelled F-actin, G-actin [12.5 µM] was mixed in a ratio of approx. 3.75:1 with alexa-561-labelled actin [10 µM] (Thermo Fisher) by mixing 3 µl G-actin with 1 µl alexa-labelled actin. The actin mix was centrifuged at 120.000 g for 5 min at 4°C, the supernatant was taken off and mixed with 6 µl G-buffer to achieve a volume of 10 µl. To this, 10 µl of 2xF-buffer (40 mM Imidazole, 200 mM KCl, 4 mM MgCl2, 400 mM DTT, 12 mg/ml glucose (w/v), 80 µg/ml catalase, 400 µg/ml glucose oxidase, 1.6 mM ATP) was added to achieve a "1x" concentration of the F-buffer. The actin was left to polymerize for 20 min at room temperature in a dark chamber before use.

Gliding assay (Chapter 3)

For the myosin V gliding assay, 2 µl F-actin (as described above) were taken up in 13 µl 1 x F-buffer (20 mM Imidazole, 100 mM KCl, 2 mM MgCl2, 200 mM DTT, 6 mg/ml glucose (w/v), 40 µg/ml catalase, 200 µg/ml glucose oxidase, 0.8 mM ATP) and flown into the flow channel. The filaments were left to settle

for 5 min, then 2 µl of freshly purified GFP-myosin V (as above) were taken up in 13 µl 1 x F-buffer and flown into the channel. The channel was left to settle for 5 min, before gliding of actin filaments was imaged. Other components were added to the channel together with myosin in the following final concentrations [stock]: Calmodulin 30 µM [500 µM], Caldendrin 5 µM [75 µM], CaCl2 200 µM [10 mM]. Timelapse imaging was performed on a Spinning-disc confocal with a Nikon Eclipse Ti-E as described under "Live cell imaging", with 1 frame per second for two to three minutes.

Analysis of gliding assay (Chapter 3)

In order to assess what percentage of actin filaments were actively transported ("gliding") as opposed to being immobile, the first and 30th frame of a timelapse stack were overlayed in different colours (first frame = red, 30th frame = green). Filaments that had moved during this timespan appear either red or green, whereas immobile filaments appear yellow. Those filaments were counted manually and the percentage of total filaments was calculated.

List of pharmacological treatments (Chapter 1 & 2)

Latrunculin A (LatA), SMIFH2, CK-666, Brefeldin-A, MyoVin, and TIP were dissolved in DMSO according to manufacturer's recommendations. DIV18 neurons were treated with Brefeldin-A, LatA , SMIFH2, CK-666, or DMSO and after indicated time points were fixed in 4 % Roti-Histofix/4 % sucrose in phosphate buffered saline (PBS), and preceded for immunostainings as described. LatA treatment was initially performed for 15 and 35 min and thereafter all other experiments were performed within this time window.

For myosin inhibitor treatments, DIV14 neurons were transfected with LAMP1-eGFP and mRuby3. One day after, 5-8 cells per condition were imaged before and after treatment with either MyoVin or TIP.

Pharmacological compounds

Pharmacological compounds	**Source**	**Product number**	**Concentration**	**Treatment duration**
TTX	*Tocris*	1078	1 µM	30 min
Latrunculin A	*Tocris*	3973	5 µM	30 min
Brefeldin A	*Cell Signalling*	9972S	100 ng/ml	10 h
SIMFH2	*Sigma-Aldrich*	S4826	30 µM	90 min
CK666	*Sigma-Aldrich*	SML0006	50 µM	2 h
MyoVin	*Merck*	475984	30 µM	30 min
TIP	*Sigma-Aldrich*	19566	4 µM	30 min
DMSO	Carl Roth	4720.4	n.a.	2 h

Other reagents

Reagent	**Source**	**Product number**	**Final concentration**
phalloidin–Atto647N	Sigma-Aldrich	65906	IF: 1:40
Streptavidin-HRP	Pierce	21130	WB: 1:10000
Lysotracker Green DND-26	Thermo Fisher	L7526	1:20.000
LysoTracker Red DND-99	*Thermo Fisher*	L7528	1:20.000

List of constructs (Chapters 1, 2, 3)

Backbone	Promoter	Insert	Source
pAAV	synapsin	mRuby2	Addgene #99126 (Chan et al., 2017)
pAAV	synapsin	YFP	Mikhaylova et al. 2018
pAAV	synapsin	$LAMP1_{(rat.trans.var.x1)}$-eGFP	Bommel et al. 2019
pAAV	synapsin	$LAMP1_{(rat.trans.var.x1)}$-mCherry	Bommel et al. 2019
pAAV	synapsin	Actin-chromobody-TagRFP	Bommel et al. 2019
pCI	Synapsin	mCerulean	Gift from T.G. Oertner, ZMNH
pCI	Synapsin	myosinV-DN-mCerulean (bp 4242 – 5487; NCBI: XM_006510832.3)	Konietzny et al. 2019
pAAV	Synapsin	myosinVI-DN-GFP (bp 3177-3789; NCBI: NM_001039546.2)	Konietzny et al. 2019
pAAV	Synapsin	PEX3-emEGFP-p2A-KIF17	Bommel et al. 2019
pAAV	synapsin	synaptopodin-GFP	Bommel et al. 2019
pMH4	synapsin	ER-pDsRed2 (CALR-DsRed-KDEL)	Gift from T.G. Oertner, ZMNH
pCI	CMV	HA-BirA	Jaworski et al., 2009
pEGFP	CMV	synaptopodin-GFP-bio	Konietzny et al. 2019
peGFP-C1	CMV	eGFP	Clontech #6085-1
pcDNA3.1	CMV	empty vector	Thermo Fisher Scientific #V855-20
pcDNA3.1	CMV	Caldendrin (untagged) (897 bp; NCBI: Y17048.2)	Mikhaylova et al. 2018
pmEmerald	CMV	GFP-myosin Va full length (5487 bp; NCBI: XM_006510832.3)	Gift from W. Wagner, ZMNH
pmEmerald	CMV	TwinStrep-GFP-myosin Va	This study
pmEmerald	CMV	TwinStrep-GFP-myosin VI	This study
pmEmerald	CMV	Myosin motor fragment (bp 1-2265)	This study
pmEmerald	CMV	Myosin motor + IQ 1-2 (bp 1 – 2372)	This study

pmEmerald	CMV	Myosin motor + coiled coil (bp 1 – 3683)	This study
pmEmerald	CMV	coiled coil + GTD (bp 3683-5487)	This study
pmEmerald	CMV	Myosin IQ motifs 1-2 (bp 2227 – 2373)	This study
pmEmerald	CMV	Myosin IQ motifs 3-6 (bp 2373 - 2769)	This study
pTagRFP	CMV	Caldendrin-tagRFP	This study
pTagRFP	CMV	Caldendrin N-terminus tagRFP (bp 1 – 408)	This study
pTagRFP	CMV	Caldendrin C-terminus tagRFP (bp 409 – 897)	This study
pET	T7	calmodulin (untagged)	This study
pMXB10	T7	Caldendrin-Intein-tag	Mikhaylova et al. 2018

List of antibodies (Chapters 1, 2, 3)

Primary antibodies:

IF = Immunofluorescence. WB = western blot.

Antibody	**Species**	**Source**	**Product #**	**Dilution**
Synaptopodin	Rabbit	Synaptic Systems	163002	IF 1:600
Synaptopodin	Mouse	Synaptic Systems	n.a.	IF 1:500
Synaptopodin	Rabbit	Sigma	S9442	IF: 1:1000
MAP2	Mouse	Sigma	M4403	IF 1:500
MAP2	Rabbit	Abcam	Ab32454	IF 1:500
homer1	Mouse	Synaptic Systems	160011	IF 1:500
myosin Va	Rabbit	Sigma	m4812	WB/IF: 1:500
myosin Vb	Rabbit	Santa Cruz	sc-98020	WB: 1:500
myosin Id	Rabbit	Santa Cruz	sc-66982	WB 1:200
myosin VI	Rabbit	Santa Cruz	sc-50461	WB/IF: 1:200
β-actin	Mouse	Sigma	A5441	WB: 1:500
Shank3	Guinea pig	Synaptic Systems	162304	IF: 1:500
GFP	Mouse	Covance	MMS-118P	WB: 1:500
cortactin	Rabbit	*Santa Cruz*	Sc-11408	IF: 1:200
LAMP1	Rabbit	*Abcam*	ab24170	IF: 1:200
LAMP1	mouse	*DSHB*	1D4B	WB: 1:1000
KIF5C	rabbit	*Thermo Fisher*	PA1-644	WB: 1:1000
dynein IC1/2	mouse	*Santa Cruz*	sc-13524	WB: 1:1000
PMP70	mouse	*Sigma*	SAB4200181	IF: 1:750 WB: 1:1000
PEX14	rabbit	*Proteintech*	10594-1-AP	IF: 1:750 WB: 1:1000
tagRFP	rabbit	*Evrogen*	AB233	WB: 1:500
GFP	mouse	*Covance*	MMS-118P	WB: 1:1000
Caldendrin	rabbit	*Mikhaylova et al. 2018*	n.a.	WB: 1:500

Secondary antibodies:

Antibody	**Conjugation**	**Source**	**Product #**	**Dilution**
anti-rabbit	Alexa Fluor 488	Life Technologies	A11034	IF 1:500
anti-rabbit	Alexa Fluor 586	Life Technologies	A11036	IF 1:500
Anti-rabbit	Alexa Fluor 647	Life Technologies	A21245	IF: 1:500
anti-mouse	Alexa Fluor 488	Life Technologies	A11029	IF 1:500
anti-mouse	Alexa Fluor 586	Life Technologies	A11004	IF 1:500
Anti-guinea pig	Alexa Fluor 488	Invitrogen	A-11073	IF: 1:500
Anti-mouse	AbberiorStar 580	Sigma	**52403**	IF: 1:500 (STED)
Anti-rabbit	Abberior Star 580	Sigma	41367	IF: 1:250
Anti-rabbit	Atto-647N	Sigma	**40839**	IF: 1:500 (STED)
anti-rabbit	HRP	Dianova	111-035-144	WB 1:20000
Anti-RFP-X4	AbberiorStar 580	NanoTag	N0404-Ab580-S	ICC: 1:250
Anti-mouse	HRP	Dianova	115-035-146	1:20.000
Anti-rabbit	HRP	Dianova	111-035-144	1:20.000

Appendix

List of hazardous substances used according to the GHS (H- and P-statements)

Chemical	**GHS hazard**	**Hazard statement (H)**	**Precautionary statement (P)**
Acetic acid	GHS02, GHS05	226, 314	280, 305+351+338, 310
Acrylamide 37%	GHS06, GHS08	301, 312, 315, 317, 319, 332, 340, 350, 361f, 372	201, 280, 301+310, 305+351+338, 308+313
Ammonium hydroxide	GHS05, GHS09	314, 400	260, 264, 273, 280, 301+330+331, 303+361+353, 304+340, 305+351+338, 310, 321, 363, 391, 405,501
Ampicillin	GHS08	334, 317	280, 261, 302+352, 342+311
APS (Ammonium persulfate)	GHS03, GHS07, GHS08	272, 302, 315, 317, 319, 334, 335	280, 305+351+338, 302+352, 304+341, 342+311
beta-Mercaptoethanol	GHS05, GHS06, GHS08, GHS09	301+331, 310, 315, 317, 318, 373, 410	260, 262, 273, 280, 301+310+330, 302+352+310, 305+351+338+310, 391, 403+233
Brefeldin A	GHS06	301	264, 270, 301+310, 321, 330, 405,501
CK666	GHS07	319	264, 280, 305+351+338,337+313
cOmplete, EDTA free protease inhibitor tablets (Roche)	GHS05	314	260, 280, 301+330+331, 303+361+353, 304+340+310, 305+351+338+310
DMSO (Dimethylsulfoxide)		315, 319, 335	261, 264, 271, 280, 302+352, 304+340, 305+351+338, 312, 321, 332+313, 337+313, 362, 403+233, 405,501
DTT (Dithiothreitol)	GHS07	302, 315, 319, 335	261, 302+352, 305+351+338, 501

EDTA (Ethylenediaminetetraacetic acid)	GHS07	319	305+351+338
Ethanol	GHS02	225	210
Hydrogen peroxide	GHS03, GHS05,GHS07	271, 302, 314, 332	210, 220, 221, 260, 261, 264, 270, 271, 280, 283, 301+312, 301+330+331, 303+361+353, 304+312, 304+340, 305+351+338, 306+360, 310, 312, 321, 330, 363, 370+378, 371+380+375, 405,501
IPTG (Isopropyl β- d-1-thiogalactopyranoside)	GHS07, GHS08	319, 351	281, 305+351+338
Kanamycin	GHS08	306	201, 308+313
Methanol	GHS02, GHS06, GHS08	225, 301+311+331, 370	210, 280, 302+352+312+304+340+312, 370+378, 403+235
PEI (Polyethylenimine)	GHS07	312, 315	280, 285, 302+352, 305, 313, 351
phalloidin–Atto647N	GHS06	300, 310, 330	260, 264, 280, 284, 301 + 310, 302 + 350
Roti Histofix	GHS02, GHS05, GHS06, GHS08	302, 317, 341, 350	261, 280, 302+352, 308+313
SDS (Sodium dodecyl sulfate)	GHS02, GHS06	228, 302, 311, 315, 319, 335	210, 261, 280, 312, 305+351+338
SMIFH2	GHS06	301	264, 270, 301+310, 321, 330, 405,501
Sodium azide	GHS06, GHS09	300, 400, 410	264, 270, 273, 301+310, 321, 330, 391, 405,501
Streptavidin-HRP	GHS07	315, 319, 335	261, 264, 271, 280, 302+352, 304+340, 305+351+338, 312, 321, 332+313, 337+313, 362, 403+233, 405,501
TEMED (Tetramethylethylenediamine)	GHS07	315, 319, 335	261, 305+351+338

TIP (2,4,6-triiodophenol)	GHS07	302, 312, 315, 319, 332, 335	261, 264, 270, 271, 280, 301+312, 302+352, 304+312, 304+340, 305+351+338, 312, 321, 322, 330, 332+313, 337+313, 362, 363, 403+233, 405,501
Tris-HCl	GHS07	315, 319+335	261, 305+351+338
Triton-X-100	GHS05, GHS07, GHS09	302, 315, 318, 410	280, 301+312+330, 305+351+338+310
Trypsin	GHS07, GHS08	315, 319, 334, 335	261, 264, 271, 280, 285, 302+352, 304+340, 304+341, 305+351+338, 312, 321, 332+313, 337+313, 342+311
TTX (Tetrodotoxin)	GHS06	300, 310, 330	260, 262, 264, 270, 271, 280, 284, 301+310, 302+350, 304+340, 310, 320, 321, 322, 330, 361, 363, 403+233, 405,501

Cited literature:

Asanuma K, Kim K, Oh J, Giardino L, Chabanis S, Faul C, Reiser J & Mundel P (2005) Synaptopodin regulates the actin-bundling activity of α-actinin in an isoform-specific manner. *J. Clin. Invest.* **115:** 1188–1198

Avraham KB, Hasson T, Steel KP, Kingsley DM, Russel LB, Mooseker MS, Copeland NG & Jenkins NA (1995) The mouse Snell's waltzer deafness gene encodes an unconventional myosin required for structural integrity of inner ear hair cells. *Nature* **11:** 369–375

Balasanyan V & Arnold DB (2014) Actin and Myosin-dependent localization of mRNA to dendrites. *PLoS One* **9:** e92349

Bär J, Kobler O, van Bommel B & Mikhaylova M (2016) Periodic F-actin structures shape the neck of dendritic spines. *Sci. Rep.* **6:** 37136

Bas Orth C, Schultz C, Müller CM, Frotscher M & Deller T (2007) Loss of the Cisternal Organelle in the Axon Initial Segment of Cortical Neurons in Synaptopodin-Deficient Mice. *J. Comp. Neurol.* **504:** 441–449

van Bergeijk P, Adrian M, Hoogenraad CC & Kapitein LC (2015) Optogenetic control of organelle transport and positioning. *Nature* **518:** 111–114

van Bergeijk P, Hoogenraad CC & Kapitein LC (2016) Right Time, Right Place: Probing the Functions of Organelle Positioning. *Trends Cell Biol.* **26:** 121–134

Bommel B Van, Konietzny A, Kobler O, Bär J & Mikhaylova M (2019) F-actin patches associated with glutamatergic synapses control positioning of dendritic lysosomes. *EMBO J.* **e101183:** 1–17

Bosch M, Castro J, Saneyoshi T, Matsuno H, Sur M & Hayashi Y (2014) Structural and Molecular Remodeling of Dendritic Spine Substructures during Long-Term Potentiation. *Neuron* **82:** 444–459

Caviston JP, Zajac AL, Tokito M & Holzbaur ELF (2011) Huntingtin coordinates the dynein-mediated dynamic positioning of endosomes and lysosomes. *Mol. Biol. Cell* **22:** 478–492

Chalovich JM & Schroeter MM (2010) Synaptopodin family of natively unfolded, actin binding proteins: Physical properties and potential biological functions. *Biophys. Rev.* **2:** 181–189

Chang DTW, Honick AS & Reynolds IJ (2006) Mitochondrial trafficking to synapses in cultured primary cortical neurons. *J. Neurosci.* **26:** 7035–7045

Chardin P & McCormick F (1999) Brefeldin A: The advantage of being uncompetitive. *Cell* **97:** 153–155

Cheng XT, Xie YX, Zhou B, Huang N, Farfel-Becker T & Sheng ZH (2018) Characterization of LAMP1-labeled nondegradative lysosomal and endocytic compartments in neurons. *J. Cell Biol.* **217:** 3127–3139

Correia SS, Bassani S, Brown TC, Lisé M-F, Backos DS, El-Husseini A, Passafaro M & Esteban JA (2008) Motor protein-dependent transport of AMPA receptors into spines during long-term potentiation. *Nat. Neurosci.* **11:** 457–66

Czarnecki K, Haas CA, Bas Orth C, Deller T & Frotscher M (2005) Postnatal development of

synaptopodin expression in the rodent hippocampus. *J. Comp. Neurol.* **490:** 133–144

D'Este E, Kamin D, Göttfert F, El-Hady A & Hell S (2015) STED Nanoscopy Reveals the Ubiquity of Subcortical Cytoskeleton Periodicity in Living Neurons. *Cell Rep.* **10:** 1246–1251

Deller T, Bas Orth C, Del Turco D, Vlachos A, Burbach GJ, Drakew A, Chabanis S, Korte M, Schwegler H, Haas CA & Frotscher M (2007) A role for synaptopodin and the spine apparatus in hippocampal synaptic plasticity. *Ann. Anat.* **189:** 5–16

Deller T, Korte M, Chabanis S, Drakew A, Schwegler H, Stefani GG, Zuniga A, Schwarz K, Bonhoeffer T, Zeller R, Frotscher M & Mundel P (2003) Synaptopodin-deficient mice lack a spine apparatus and show deficits in synaptic plasticity. *Proc. Natl. Acad. Sci. U. S. A.* **100:** 10494–9

Donnelly MLL, Luke G, Mehrotra A, Li X, Hughes LE, Gani D & Ryan MD (2001) Analysis of the aphthovirus 2A/2B polyprotein 'cleavage' mechanism indicates not a proteolytic reaction, but a novel translational effect: A putative ribosomal 'skip'. *J. Gen. Virol.* **82:** 1013–1025

Esteves da Silva M, Adrian M, Schätzle P, Lipka J, Watanabe T, Cho S, Futai K, Wierenga CJ, Kapitein LC & Hoogenraad CC (2015) Positioning of AMPA Receptor-Containing Endosomes Regulates Synapse Architecture. *Cell Rep.* **13:** 933–943

Farías GG, Guardia CM, De Pace R, Britt DJ & Bonifacino JS (2017) BORC/kinesin-1 ensemble drives polarized transport of lysosomes into the axon. *Proc. Natl. Acad. Sci.* **114:** E2955–E2964

Faul C, Donnelly M, Merscher-Gomez S, Chang YH, Franz S, Delfgaauw J, Chang J-M, Choi HY, Campbell KN, Kim K, Reiser J & Mundel P (2008) The actin cytoskeleton of kidney podocytes is a direct target of the antiproteinuric effect of cyclosporine A. *Nat. Med.* **14:** 931–938

Flores LR, Keeling MC, Zhang X, Sliogeryte K & Gavara N (2019) Lifeact-GFP alters F-actin organization, cellular morphology and biophysical behaviour. *Sci. Rep.* **9:** 1–13

Frese CK, Mikhaylova M, Stucchi R, Gautier V, Liu Q, Mohammed S, Heck AJR, Altelaar AFM & Hoogenraad CC (2017) Quantitative map of proteome dynamics during neuronal differentiation. *Cell Rep.* **18:** 1527–1542

Ganguly A, Tang Y, Wang L, Ladt K, Loi J, Dargent B, Leterrier C & Roy S (2015) A dynamic formin-dependent deep F-actin network in axons. *J. Cell Biol.* **210:** 401–417

Goo MS, Sancho L, Slepak N, Boassa D, Deerinck TJ, Ellisman MH, Bloodgood BL & Patrick GN (2017) Activity-dependent trafficking of lysosomes in dendrites and dendritic spines. *J. Cell Biol.***:** 1–15

Gramlich MW & Klyachko VA (2017) Actin/Myosin-V- and Activity-Dependent Inter-synaptic Vesicle Exchange in Central Neurons. *Cell Rep.* **18:** 2096–2104

Gulledge AT, Kampa BM & Stuart GJ (2005) Synaptic integration in dendritic trees. *J. Neurobiol.* **64:** 75–90

Hangen E, Cordelières FP, Petersen JD, Choquet D & Coussen F (2018) Neuronal Activity and Intracellular Calcium Levels Regulate Intracellular Transport of Newly Synthesized AMPAR. *Cell Rep.* **24:** 1001-1012.e3

Hanus C & Ehlers MD (2016) Specialization of biosynthetic membrane trafficking for neuronal form and function. *Curr. Opin. Neurobiol.* **39:** 8–16

Hanus C, Kochen L, Tom Dieck S, Racine V, Sibarita JB, Schuman EM & Ehlers MD (2014) Synaptic Control of Secretory Trafficking in Dendrites. *Cell Rep.* **7:** 1771–1778

He J, Zhou R, Wu Z, Carrasco MA, Kurshan PT, Farley JE, Simon DJ, Wang G, Han B, Hao J, Heller E, Freeman MR, Shen K, Maniatis T, Tessier-Lavigne M & Zhuang X (2016) Prevalent presence of periodic actin-spectrin-based membrane skeleton in a broad range of neuronal cell types and animal species. *Proc. Natl. Acad. Sci.* **113:** 6029–6034

Heissler SM, Chinthalapudi K & Sellers JR (2017) Kinetic signatures of myosin-5B, the motor involved in microvillus inclusion disease. *J. Biol. Chem.* **292:** 18372–18385

Heissler SM, Selvadurai J, Bond LM, Fedorov R, Kendrick-Jones J, Buss F & Manstein DJ (2012) Kinetic properties and small-molecule inhibition of human myosin-6. *FEBS Lett.* **586:** 3208–3214

Hering H & Sheng M (2003) Activity-dependent redistribution and essential role of cortactin in dendritic spine morphogenesis. *J. Neurosci.* **23:** 11759–11769

Hetrick B, Han MS, Helgeson LA & Nolen BJ (2013) Small molecules CK-666 and CK-869 inhibit actin-related protein 2/3 complex by blocking an activating conformational change. *Chem. Biol.* **20:** 701–712

Hodges JL, Vilchez SM, Asmussen H, Whitmore LA & Horwitz AR (2014) α-Actinin-2 mediates spine morphology and assembly of the post-synaptic density in hippocampal neurons. *PLoS One* **9:**

Holbro N, Grunditz A & Oertner TG (2009) Differential distribution of endoplasmic reticulum controls metabotropic signaling and plasticity at hippocampal synapses. *Proc. Natl. Acad. Sci. U. S. A.* **106:** 15055–60

Homma K, Saito J, Ikebe R & Ikebe M (2000) Ca2+-dependent regulation of the motor activity of myosin V. *J. Biol. Chem.* **275:** 34766–34771

Honkura N, Matsuzaki M, Noguchi J, Ellis-Davies GCR & Kasai H (2008) The Subspine Organization of Actin Fibers Regulates the Structure and Plasticity of Dendritic Spines. *Neuron* **57:** 719–729

Hou W, Izadi M, Nemitz S, Haag N, Kessels MM & Qualmann B (2015) The Actin Nucleator Cobl Is Controlled by Calcium and Calmodulin. *PLoS Biol.* **13:** 1–30

Huang F, Chotiner JK & Steward O (2007) Actin polymerization and ERK phosphorylation are required for Arc/Arg3.1 mRNA targeting to activated synaptic sites on dendrites. *J. Neurosci.* **27:** 9054–9067

Janssen AFJ, Tas RP, van Bergeijk P, Oost R, Hoogenraad CC & Kapitein LC (2017) Myosin-V Induces Cargo Immobilization and Clustering at the Axon Initial Segment. *Front. Cell. Neurosci.* **11:** 1–11

Kapitein LC, Schlager M a., Van Der Zwan W a., Wulf PS, Keijzer N & Hoogenraad CC (2010) Probing intracellular motor protein activity using an inducible cargo trafficking assay. *Biophys. J.* **99:** 2143–2152

Kapitein LC, van Bergeijk P, Lipka J, Keijzer N, Wulf PS, Katrukha EA, Akhmanova A & Hoogenraad CC (2013) Myosin-V Opposes Microtubule-Based Cargo Transport and Drives Directional Motility on Cortical Actin. *Curr. Biol.* **23:** 828–834

Karagas NE & Venkatachalam K (2019) Roles for the Endoplasmic Reticulum in Regulation of Neuronal Calcium Homeostasis. *Cells* **8:** 1232

Katrukha EA, Mikhaylova M, van Brakel HX, van Bergen en Henegouwen PM, Akhmanova A, Hoogenraad CC & Kapitein LC (2017) Probing cytoskeletal modulation of passive and active intracellular dynamics using nanobody-functionalized quantum dots. *Nat. Commun.* **8:** 14772

Kneussel M & Wagner W (2013) Myosin motors at neuronal synapses: drivers of membrane transport and actin dynamics. *Nat. Rev. Neurosci.* **14:** 233–247

Konietzny A, Bär J & Mikhaylova M (2017) Dendritic Actin Cytoskeleton: Structure, Functions, and Regulations. *Front. Cell. Neurosci.* **11:** 1–10

Konietzny A, González-Gallego J, Bär J, Perez-Alvarez A, Drakew A, Demmers JAA, Dekkers DHW, Hammer JA, Frotscher M, Oertner TG, Wagner W, Kneussel M & Mikhaylova M (2019) Myosin V regulates synaptopodin clustering and localization in dendrites of hippocampal neurons. *J. Cell Sci.***:** jcs.230177

Korkotian E, Frotscher M & Segal M (2014) Synaptopodin Regulates Spine Plasticity: Mediation by Calcium Stores. *J. Neurosci.* **34:** 11641–11651

Korobova F & Svitkina T (2008) Arp2/3 Complex Is Important for Filopodia Formation, Growth Cone Motility, and Neuritogenesis in Neuronal Cells. *Mol. Biol. Cell* **19:** 1516–1574

Korobova F & Svitkina T (2010) Molecular Architecture of Synaptic Actin Cytoskeleton in Hippocampal Neurons Reveals a Mechanism of Dendritic Spine Morphogenesis. *Mol. Biol. Cell* **21:** 165–176

Kowalski JR, Egile C, Gil S, Snapper SB, Li R & Thomas SM (2005) Cortactin regulates cell migration through activation of N-WASP. *J Cell Sci* **118:** 79–87

Krementsov DN, Krementsova EB & Trybus KM (2004) Myosin V: Regulation by calcium, calmodulin, and the tail domain. *J. Cell Biol.* **164:** 877–886

Kremerskothen J, Plaas C, Kindler S, Frotscher M & Barnekow A (2005) Synaptopodin, a molecule involved in the formation of the dendritic spine apparatus, is a dual actin/??-actinin binding protein. *J. Neurochem.* **92:** 597–606

Kügler S, Kilic E & Bähr M (2003) Human synapsin 1 gene promoter confers highly neuron-specific long-term transgene expression from an adenoviral vector in the adult rat brain depending on the transduced area. *Gene Ther.* **10:** 337–347

Lee BH & Park HY (2018) HybTrack: A hybrid single particle tracking software using manual and automatic detection of dim signals. *Sci. Rep.* **8:** 1–7

Ligon LA & Steward O (2000) Role of microtubules and actin filaments in the movement of Mitochondria in the Axons and Dendrites of Cultured Hippocampal Neurons. *J Comp Neurol* **427:** 351–361

Lin Y-C & Redmond L (2008) CaMKIIbeta binding to stable F-actin in vivo regulates F-actin filament stability. *Proc. Natl. Acad. Sci. U. S. A.* **105:** 15791–6

Liu J, Taylor DW, Krementsova EB, Trybus KM & Taylor KA (2006) Three-dimensional structure of the myosin V inhibited state by cryoelectron tomography. *Nature* **442:** 208–211

Liu Z, Chen O, Wall JBJ, Zheng M, Zhou Y, Wang L, Ruth Vaseghi H, Qian L & Liu J (2017) Systematic comparison of 2A peptides for cloning multi-genes in a polycistronic vector. *Sci. Rep.* **7:** 1–9

Lu H, Krementsova EB & Trybus KM (2006) Regulation of myosin V processivity by calcium at the single molecule level. *J. Biol. Chem.* **281:** 31987–31994

Lu Z, Shen M, Cao Y, Zhang HM, Yao LL & Li XD (2012) Calmodulin bound to the first IQ motif is responsible for calcium-dependent regulation of myosin 5a. *J. Biol. Chem.* **287:** 16530–16540

Magee JC (2000) Dendritic integration of excitatory synaptic input. *Nat. Rev. Neurosci.* **1:** 181–190

Mangeol P, Prevo B & Peterman EJG (2016) KymographClear and KymographDirect: two tools for the automated quantitative analysis of molecular and cellular dynamics using kymographs. *Mol. Biol. Cell* **27:** 1948–1957

Maravall M, Mainen ZF, Sabatini BL & Svoboda K (2000) Estimating intracellular calcium concentrations and buffering without wavelength ratioing. *Biophys. J.* **78:** 2655–2667

Martin KC & Ephrussi A (2010) mRNA Localization : Gene Expression in the Spatial Dimension. *Cell* **136:** 1–21

Matt L, Kim K, Hergarden AC, Patriarchi T, Malik ZA, Park DK, Chowdhury D, Buonarati OR, Henderson PB, Gökçek Saraç Ç, Zhang Y, Mohapatra D, Horne MC, Ames JB & Hell JW (2018) α-Actinin Anchors PSD-95 at Postsynaptic Sites. *Neuron* **97:** 1094-1109.e9

Mikhaylova M, Bär J, van Bommel B, Schätzle P, YuanXiang P, Raman R, Hradsky J, Konietzny A, Loktionov EY, Reddy PP, Lopez-Rojas J, Spilker C, Kobler O, Raza SA, Stork O, Hoogenraad CC & Kreutz MR (2018) Caldendrin Directly Couples Postsynaptic Calcium Signals to Actin Remodeling in Dendritic Spines. *Neuron* **97:**

Mikhaylova M, Bera S, Kobler O, Frischknecht R & Kreutz MR (2016) A Dendritic Golgi Satellite between ERGIC and Retromer. *Cell Rep.* **14:** 189–199

Molnár E (2011) Long-term potentiation in cultured hippocampal neurons. *Semin. Cell Dev. Biol.* **22:** 506–513

Mundel P, Heid HW, Mundel TM, Krüger M, Reiser J & Kriz W (1997) Synaptopodin: An actin-associated protein in telencephalic dendrites and renal podocytes. *J. Cell Biol.* **139:** 193–204

Na Y, Park S, Lee C, Sockanathan S, Huganir RL, Worley PF, Na Y, Park S, Lee C, Kim D, Park JM & Sockanathan S (2016) Real-Time Imaging Reveals Properties of Glutamate-Induced Arc/Arg 3.1 Translation in Neuronal Dendrites. *Neuron* **91:** 1–13

Nakagawa T, Engler JA & Sheng M (2004) The dynamic turnover and functional roles of α-actinin in dendritic spines. *Neuropharmacology* **47:** 734–745

Nascimento AAC, Cheney RE, Tauhata SBF, Larson RE & Mooseker MS (1996) Enzymatic characterization and functional domain mapping of brain myosin-V. *J. Biol. Chem.* **271:** 17561–17569

Neumann S, Chassefeyre R, Campbell GE & Encalada SE (2017) KymoAnalyzer: a software tool for the quantitative analysis of intracellular transport in neurons. *Traffic* **18:** 71–88

Nguyen H & Higuchi H (2005) Motility of myosin V regulated by the dissociation of single calmodulin. *Nat. Struct. Mol. Biol.* **12:** 127–132

Oertner TG & Matus A (2005) Calcium regulation of actin dynamics in dendritic spines. *Cell Calcium* **37:** 477–482

Okamoto K-I, Nagai T, Miyawaki A & Hayashi Y (2004) Rapid and persistent modulation of actin dynamics regulates postsynaptic reorganization underlying bidirectional plasticity. *Nat. Neurosci.* **7:** 1104–12

Osterweil E, Wells DG & Mooseker MS (2005) A role for myosin VI in postsynaptic structure and glutamate receptor endocytosis. *J. Cell Biol.* **168:** 329–38

Padamsey Z, McGuinness L, Bardo SJ, Reinhart M, Tong R, Hedegaard A, Hart ML & Emptage NJ

(2017) Activity-Dependent Exocytosis of Lysosomes Regulates the Structural Plasticity of Dendritic Spines. *Neuron* **93:** 132–146

Poindron P, Piguet P & Förster E (2005) New Methods for Culturing Cells from Nervous Tissues. *BioValley Monogr.* **1:**

Preciado López M, Huber F, Grigoriev I, Steinmetz MO, Akhmanova A, Dogterom M & Koenderink GH (2014) In vitro reconstitution of dynamic microtubules interacting with actin filament networks. *Methods Enzymol.* **540:** 301–320

Pu J, Guardia CM, Keren-Kaplan T & Bonifacino JS (2016) Mechanisms and functions of lysosome positioning. *J. Cell Sci.* **129:** 4329–4339

Qu Y, Hahn I, Webb S & Prokop A (2016) Periodic actin structures in neuronal axons are required to maintain microtubules.

Redmond L & Ghosh A (2005) Regulation of dendritic development by calcium signaling. *Cell Calcium* **37:** 411–416

Redondo RL & Morris RGM (2011) Making memories last: The synaptic tagging and capture hypothesis. *Nat. Rev. Neurosci.* **12:** 17–30

Rizvi SA, Neidt EM, Cui J, Feiger Z, Skau CT, Gardel ML, Kozmin SA & Kovar DR (2009) Identification and Characterization of a Small Molecule Inhibitor of Formin-Mediated Actin Assembly. *Chem. Biol.* **16:** 1158–1168

Sánchez-Ponce D, Blázquez-Llorca L, Defelipe J, Garrido JJ & Muñoz A (2012) Colocalization of α-actinin and synaptopodin in the pyramidal cell axon initial segment. *Cereb. Cortex* **22:** 1648–1661

Sánchez-Ponce D, DeFelipe J, Garrido JJ & Muñoz A (2011) In vitro maturation of the cisternal organelle in the hippocampal neuron's axon initial segment. *Mol. Cell. Neurosci.* **48:** 104–116

Sbalzarini IF & Koumoutsakos P (2005) Feature point tracking and trajectory analysis for video imaging in cell biology. *J. Struct. Biol.* **151:** 182–195

Schätzle P, Esteves da Silva M, Tas RP, Katrukha EA, Hu HY, Wierenga CJ, Kapitein LC & Hoogenraad CC (2018) Activity-Dependent Actin Remodeling at the Base of Dendritic Spines Promotes Microtubule Entry. *Curr. Biol.***:** 1–13

Shah MM, Hammond RS & Hoffman D (2010) Dendritic Ion Channel Trafficking and Plasticity. **33:** 307–316

Shen M, Zhang N, Zheng S, Zhang W-B, Zhang H-M, Lu Z, Su QP, Sun Y, Ye K & Li X-D (2016) Calmodulin in complex with the first IQ motif of myosin-5a functions as an intact calcium sensor. *Proc. Natl. Acad. Sci. U. S. A.* **113:** E5812–E5820

Smith B a, Daugherty-Clarke K, Goode BL & Gelles J (2013) Pathway of actin filament branch formation by Arp2/3 complex revealed by single-molecule imaging. *Proc. Natl. Acad. Sci. U. S. A.* **110:** 1285–1290

Sood P, Murthy K, Kumar V, Nonet ML, Menon GI & Koushika SP (2018) Cargo crowding at actin-rich regions along axons causes local traffic jams. *Traffic* **19:** 166–181

Spence EF, Kanak DJ, Carlson BR & Soderling SH (2016) The Arp2/3 Complex Is Essential for Distinct Stages of Spine Synapse Maturation, Including Synapse Unsilencing. *J. Neurosci.* **36:** 9696–9709

Sung JY, Engmann O, Teylan MA, Nairn AC, Greengard P & Kim Y (2008) WAVE1 controls neuronal activity-induced mitochondrial distribution in dendritic spines. *Proc. Natl. Acad. Sci. U. S. A.* **105:** 3112–3116

Thirumurugan K, Sakamoto T, Hammer JA, Sellers JR & Knight PJ (2006) The cargo-binding domain regulates structure and activity of myosin 5. *Nature* **442:** 212–5

Tinevez JY, Perry N, Schindelin J, Hoopes GM, Reynolds GD, Laplantine E, Bednarek SY, Shorte SL & Eliceiri KW (2017) TrackMate: An open and extensible platform for single-particle tracking. *Methods* **115:** 80–90

Toresson H & Grant SGN (2005) Dynamic distribution of endoplasmic reticulum in hippocampal neuron dendritic spines. *Eur. J. Neurosci.* **22:** 1793–1798

Trybus KM, Gushchin MI, Lui H, Hazelwood L, Krementsova EB, Volkmann N & Hanein D (2007) Effect of calcium on calmodulin bound to the IQ motifs of myosin V. *J. Biol. Chem.* **282:** 23316–23325

Trybus KM, Krementsova E & Freyzon Y (1999) Kinetic characterization of a monomeric unconventional myosin V construct. *J. Biol. Chem.* **274:** 27448–27456

Verbich D, Becker D, Vlachos A, Mundel P, Deller T & McKinney RA (2016) Rewiring neuronal microcircuits of the brain via spine head protrusions--a role for synaptopodin and intracellular calcium stores. *Acta Neuropathol. Commun.* **4:** 38

Vlachos A, Ikenberg B, Lenz M, Becker D, Reifenberg K, Bas-Orth C & Deller T (2013) Synaptopodin regulates denervation-induced homeostatic synaptic plasticity. *Proc. Natl. Acad. Sci.* **110:** 8242–8247

Vlachos A, Korkotian E, Schonfeld E, Copanaki E, Deller T & Segal M (2009) Synaptopodin regulates plasticity of dendritic spines in hippocampal neurons. *J. Neurosci.* **29:** 1017–1033

Wagner W, Brenowitz SD & Hammer JAI (2011) Myosin-Va Transports the Endoplasmic Reticulum into the Dendritic Spines of Purkinje Neurons. *Nat. Cell Biol.* **1:** 40–48

Wang F, Chen L, Arcucci O, Harvey E V., Bowers B, Xu Y, Hammer JA & Sellers JR (2000) Effect of ADP and ionic strength on the kinetic and motile properties of recombinant mouse myosin V. *J. Biol. Chem.* **275:** 4329–4335

Wang F, Thirumurugan K, Stafford WF, Hammer JA, Knight PJ & Sellers JR (2004) Regulated Conformation of Myosin V. *J. Biol. Chem.* **279:** 2333–2336

Wang L, Dumoulin A, Renner M, Triller A & Specht CG (2016) The Role of Synaptopodin in Membrane Protein Diffusion in the Dendritic Spine Neck. *PLoS One* **11:** e0148310

Wang Z, Edwards JG, Riley N, Provance DW, Karcher R, Li X, Davison IG, Ikebe M, Mercer JA, Kauer JA & Ehlers MD (2008) Myosin Vb Mobilizes Recycling Endosomes and AMPA Receptors for Postsynaptic Plasticity. *Cell* **135:** 535–548

Willig KI, Steffens H, Gregor C, Herholt A, Rossner MJ & Hell SW (2014) Nanoscopy of filamentous actin in cortical dendrites of a living mouse. *Biophys. J.* **106:** L01–L03

Wu H, Nash JE, Zamorano P & Garner CC (2002) Interaction of SAP97 with minus-end-directed actin motor myosin VI: Implications for AMPA receptor trafficking. *J. Biol. Chem.* **277:** 30928–30934

Xu K, Zhong G & Zhuang X (2013) Actin, spectrin, and associated proteins form a periodic cytoskeletal structure in axons. *Science (80-.).* **339:** 452–456

Yamazaki M, Matsuo R, Fukazawa Y, Ozawa F & Inokuchi K (2001) Regulated expression of an actin-associated protein, synaptopodin, during long-term potentiation. *J. Neurochem.* **79:** 192–199

Yoon YJ, Wu B, Buxbaum AR, Das S, Tsai A, English BP, Grimm JB, Lavis LD & Singer RH (2016) Glutamate-induced RNA localization and translation in neurons. *Proc. Natl. Acad. Sci.***:** 201614267

Yoshimura A, Fujii R, Watanabe Y, Okabe S, Fukui K & Takumi T (2006) Myosin-Va Facilitates the Accumulation of mRNA/Protein Complex in Dendritic Spines. *Curr. Biol.* **16:** 2345–2351

Yu DX, Di Giorgio FP, Yao J, Marchetto MC, Brennand K, Wright R, Mei A, McHenry L, Lisuk D, Grasmick JM, Silberman P, Silberman G, Jappelli R & Gage FH (2014) Modeling hippocampal neurogenesis using human pluripotent stem cells. *Stem Cell Reports* **2:** 295–310

Yuan Y, Seong E, Singh D & Arikkath J (2015) Differential Regulation of Apical-basolateral Dendrite Outgrowth by Activity in Hippocampal Neurons. *Front. Cell. Neurosci.* **9:** 1–8

Zhang X, Pöschel B, Faul C, Upreti C, Stanton PK & Mundel P (2013) Essential role for synaptopodin in dendritic spine plasticity of the developing hippocampus. *J. Neurosci.* **33:** 12510–8

Appendix

GHS Hazard Pictograms

GHS02
Flammable

GHS03
Oxidizing

GHS05
Corrosive

GHS06
Toxic

GHS07
Irritant

GHS08
Systemic Health Hazard

GHS09
Environmental Hazard

GHS Hazard statements

H225 Highly flammable liquid and vapour

H226 Flammable liquid and vapour

H228 Flammable solid

H271 May cause fire or explosion; strong oxidizer

H272 May intensify fire; oxidizer

H300: Fatal if swallowed.

H301: Toxic if swallowed

H302: Harmful if swallowed

H310: Fatal in contact with skin

H311: Toxic in contact with skin

H312: Harmful in contact with skin

H314: Causes severe skin burns and eye damage

H315: Causes skin irritation

H317: May cause an allergic skin reaction

H318: Causes serious eye damage

H319: Causes serious eye irritation

H330: Fatal if inhaled

H331: Toxic if inhaled

H332: Harmful if inhaled

H334: May cause allergy or asthma symptoms or breathing difficulties if inhaled

H335: May cause respiratory irritation

H340: May cause genetic defects

H341: Suspected of causing genetic defects

H350: May cause cancer

H351: Suspected of causing cancer

H370: Causes damage to organs

H372: Causes damage to organs through prolonged or repeated exposure

H373: May cause damage to organs through prolonged or repeated exposure

H301+H331: Toxic if swallowed or if inhaled

H301+H311+H331: Toxic if swallowed, in contact with skin or if inhaled

H400: Very toxic to aquatic life

H410: Very toxic to aquatic life with long-lasting effects

GHS Precautionary statements

P201: Obtain special instructions before use.

P210: Keep away from heat, hot surfaces, sparks, open flames and other ignition sources. No smoking.

P220: Keep/Store away from clothing/…/combustible materials.

P221: Take any precaution to avoid mixing with combustibles.

P233: Keep container tightly closed.

P235: Keep cool.

P260: Do not breathe dust/fumes/gas/mist/vapours/spray.

P261: Avoid breathing dust/fumes/gas/mist/vapours/spray.

P262: Do not get in eyes, on skin, or on clothing.

P264: Wash … thoroughly after handling. [… (to be specified)].

P270: Do not eat, drink or smoke when using this product.

P271: Use only outdoors or in a well-ventilated area.

P273: Avoid release to the environment.

P280: Wear protective gloves/protective clothing/eye protection/face protection.

P282: Wear cold insulating gloves/face shield/eye protection.

P283: Wear fire/flame resistant/retardant clothing.

P284: [In case of inadequate ventilation] wear respiratory protection.

P301: IF SWALLOWED:

P302: IF ON SKIN:

P303: IF ON SKIN (or hair):

P304: IF INHALED:

P305: IF IN EYES:

P306: IF ON CLOTHING:

P308: IF exposed or concerned:

P310: Immediately call a POISON CENTER or doctor/physician.

P311: Call a POISON CENTER or doctor/physician.

P312: Call a POISON CENTER or doctor/physician if you feel unwell.

P313: Get medical advice/attention.

P321: Specific treatment (see ... on this label).

P322: Specific measures (see ... on this label).

P330: Rinse mouth.

P331: Do NOT induce vomiting.

P337: If eye irritation persists:

P338: Remove contact lenses, if present and easy to do. Continue rinsing.

P340: Remove victim to fresh air and keep at rest in a position comfortable for breathing.

P341: If breathing is difficult, remove victim to fresh air and keep at rest in a position comfortable for breathing.

P342: If experiencing respiratory symptoms:

P350: Gently wash with plenty of soap and water.

P351: Rinse cautiously with water for several minutes.

P352: Wash with plenty of soap and water.

P353: Rinse skin with water/shower.

P360: Rinse immediately contaminated clothing and skin with plenty of water before removing clothes.

P361: Remove/Take off immediately all contaminated clothing.

P362: Take off contaminated clothing and wash before reuse.

P363: Wash contaminated clothing before reuse.

P370: In case of fire:

P371: In case of major fire and large quantities:

P375: Fight fire remotely due to the risk of explosion.

P378: Use ... for extinction.

P380: Evacuate area.

P391: Collect spillage.

P403: Store in a well-ventilated place.

P405: Store locked up.

P501: Dispose of contents/container to...

Affidavit / Eidesstattliche Versicherung:

„Hiermit versichere ich an Eides statt, die vorliegende Dissertation selbst verfasst und keine anderen als die angegebenen Hilfsmittel benutzt zu haben. Die eingereichte schriftliche Fassung entspricht der auf dem elektronischen Speichermedium. Ich versichere, dass diese Dissertation nicht in einem früheren Promotionsverfahren eingereicht wurde."

_____

Datum, Unterschrift